PERSPIRABLE SKIN: THERMAL BUCKLING ACHIEVED BY COMPLEX FUNCTIONALLY GRADED MATERIALS

By

Mingang Wang

A DISSERTATION

Submitted to
Michigan State University
in partial fulfillment of the requirements
for the degree of

Mechanical Engineering-Doctor of Philosophy

2013

ABSTRACT

PERSPIRABLE SKIN: THERMAL BUCKLING ACHIEVED BY COMPLEX FUNCTIONALLY GRADED MATERIALS

By

Mingang Wang

A perspirable skin is a new design concept of thermal protection system to autonomously reduce the surface temperature in many applications such as reentry for space shuttle and hypersonic vehicles. A unique design features an assembly of tiles and core parts, which buckles upon heating. Potentially, a large gap can be generated through this buckling action to increase the cooling efficiency. The compressed coolant gas onboard is passed through this gap onto the surface. The coolant gas is expected to mix with the surface air eliminating the frictional heating and reducing the surface temperature. These tiles will be assembled and shrink-fitted within an opening on the existing skin (RCC).

To induce the buckling action, each tile needs to have a unique CTE gradiency, which causes expansion radially and shrinkage tangentially upon heating. For our preliminary design, the core and the tiles are made of pure ZrW_2O_8 (zirconium tungstate) and ZrW_2O_8-ZrO_2 (zirconia) Functionally Graded Material (FGM), respectively. ZrW_2O_8 has a large negative CTE value over a wide temperature range. The assembly design is modeled and verified buckling action through FEA with the best-estimated thermal

loading conditions. Most importantly, the fabrication process of these tiles made of complex Functionally Graded materials (FGMs) is described in this thesis.

During the manufacturing process, influences of both nanopowders and oxides sintering additives on the final mechanical properties of ceramic samples are discussed. The final sintered density can be improved by introducing the nanopowders due to its large surface area, while the oxides sintering additives can also help the densification by forming liquid phase. A micromechanics model is used to predict the Young's modulus values and compare with the experimental data. It is showed that two groups of values have a very good agreement based on the relative density data. In order to make the assembly to shrink-fit into the RCC skin, samples are pre-sintered and machined into specified geometry. Finally, the homogenous assembly is made in order to run the test with the furnace.

ACKNOWLEDGMENTS

I wish to express my sincere appreciation to Dr. Patrick Kwon, my advisor, for his invaluable supervision and support throughout my doctoral studies and reviews of my dissertation. I would also like to thank Dr. Dahsin Liu, Dr. Jeff Sakamoto and Dr. Seungik Baek for being on my thesis committee. I appreciate all the committee members, for their precious time on reviewing my dissertation, attending the comprehensive and final defense.

I am delighted to have a group of very knowledgeable colleagues on this project. I would like to give many thanks to Li Sun who has been a pioneer exploring and laying a good foundation for the research work. I would also like to thank John Tam, Mayeul de La Tour du Pin and Matt Lempke for their assistance in conducting lab experiments and contributions to the research work. Finally, I would like to thank my wife and my family, as I could not finish the PhD study without their help.

TABLE OF CONTENTS

LIST OF TABLES

LIST OF FIGURES

CHAPTER 1 INTRODUCTION

1.1. CURRENT THERMAL PROTECTION SYSTEM (TPS)

Thermal Protection System (TPS) is an essential component of space shuttle, which protects the vehicle from the aerodynamic heating generated at the surface. This is caused by the combination of compression and surface friction by the atmospheric gases. During the reentry into the Earth's atmosphere, the orbiter travels at speeds exceeding 27,000 km/h, and the surface temperatures can reach as high as 1440°C [1].

The space shuttle orbiter is composed of numerous advanced materials, but the main structure is mostly made of 2024-T6 aluminum and graphite- epoxy [3]. Both of them can only withstand temperatures up to 175°C; therefore, a TPS is used to prevent heat from transferring into the vehicle so that the structural frame can be maintained in the safe temperature [2, 3]. Without a TPS, the whole structure will degrade as the high surface temperature will reach into the interior. Thus, it is a very crucial element for the protection of space shuttle.

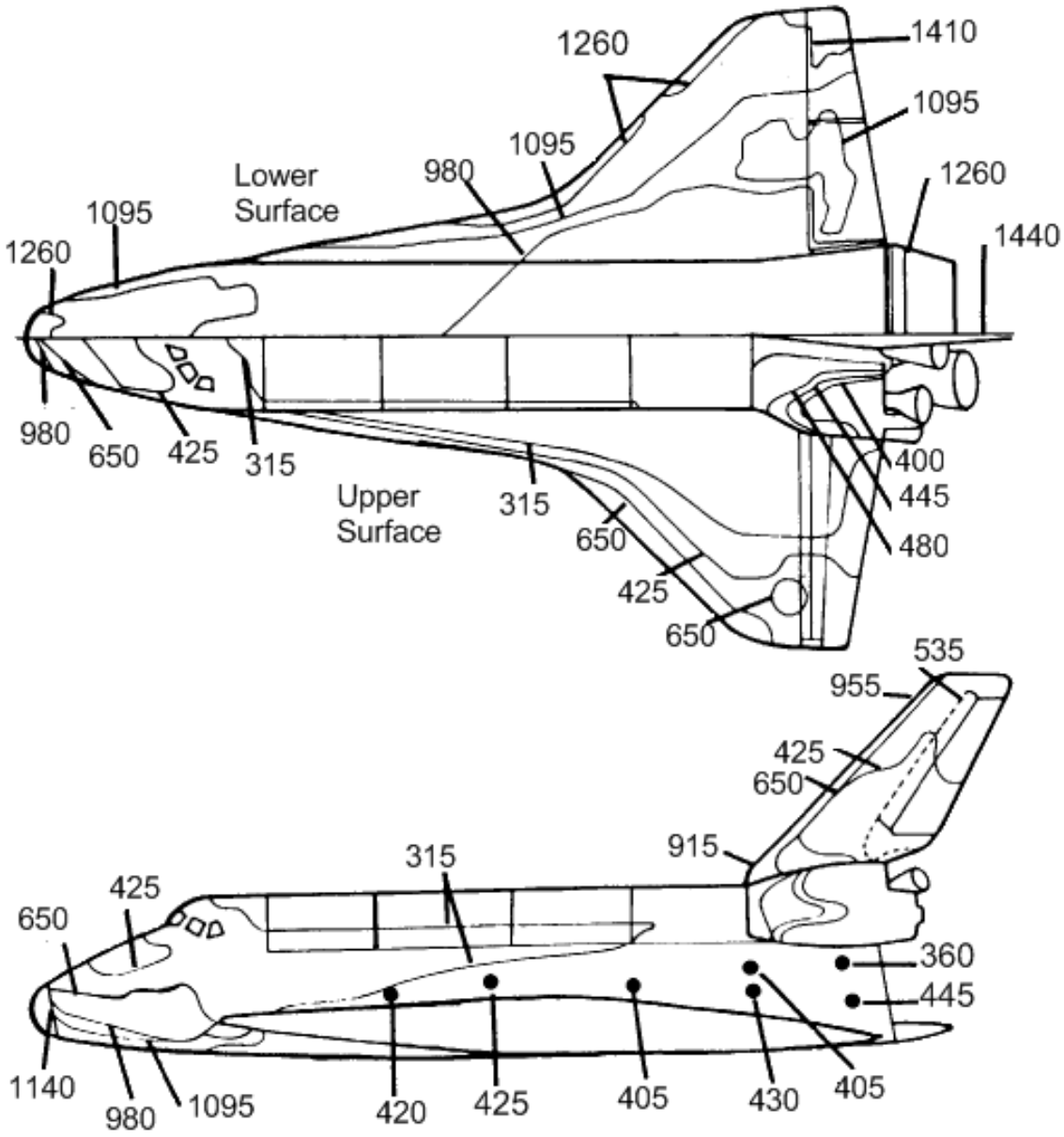

Figure 1.1. Surface temperature distribution of space shuttle; All temperatures shown are in degrees Celsius [4].

The TPS selected for a space shuttle is composed of several different materials due to the wide variation of temperatures that the vehicle experiences. Each material's thermal properties, durability, and weight determine the extent of its application on the vehicle. In

an earlier NASA report, which dated back to 1989, it was revealed that the surface temperatures distribution of a space shuttle as shown in Figure 1.1[4].

The original TPS is composed of four main materials. These materials include Reinforced Carbon-Carbon (RCC), low-temperature reusable surface insulation tiles (LRSI or white tiles), high-temperature reusable surface insulation tiles (HRSI), and felt reusable surface insulation (FRSI or black tiles) blankets [2]. Each of these tiles or blankets has different thermal properties and can withstand different temperatures as listed in Table 1.1 below.

Table 1.1. Usage of different tiles and blankets [2]

Category	Description
High-Temperature Reusable Surface Insulation (HRSI) Tiles	They have high emissivity in order to eliminate the heat during the re-entry. They can protect the covered areas up to 1,260 °C.
Low-Temperature Reusable Surface Insulation (LRSI) Tiles	They are the white tiles covering the upper surfaces of the orbiter and they can withstand temperatures up to 650 °C.
Felt Reusable Surface Insulation (FRSI) Blankets	They cover the upper section of the payload doors and the inboard sections of the upper wing surfaces. They also cover about 25% of the whole vehicle up to 370°C.
Reinforced Carbon-Carbon (RCC)	They cover the areas on the nose, chin, and leading edge of the wings where temperatures can be as high as 1,260 °C.

There are other types of tiles and blankets that also can be used on the space shuttle. Fibrous Refractory Composite Insulation (FRCI) tiles provide improved strength, durability, resistance to coating cracking and weight reduction, which can be used to

replace HRSI tiles in some areas. Another type of blanket, Advanced Flexible Reusable Surface Insulation (AFRSI), can replace most of the LRSI tiles in order to achieve the flight requirements more effectively [2].

Figure 1.2. Cross-section of Reinforced Carbon-Carbon material (RCC) [2]. For interpretation of the references to color in this and all other figures, the reader is referred to the electronic version of this dissertation.

The Reinforced Carbon-Carbon material, a most important component for the thermal protection system, has its own disadvantage. Because it covers the hottest area on the space shuttle, it also requires tedious inspection after each deployment as the high temperature will occasionally cause crack inside the structure. If damaged, the structure can lead to a serious accident as evident by the Columbia disaster. Therefore, the inspection process must be thorough, costing enormous time and labor. The motivation of this thesis is to propose a multifunctional graded material system, which composes

part of the TPS to protect certain high temperature area during re-entry into the Earth's atmosphere. The proposed design, called "Perspirable Skin", is an autonomous and reusable system, which is expected to significantly reduce the surface temperature due to the frictional heating.

1.2. CONCEPT OF PERSPIRABLE SKIN DESIGN

In humans, perspiration is essential to maintain the body temperature. When the temperature of the skin gets higher than normal temperature, the sweat glands will expand and produce sweat. When evaporated from the skin, it will have a cooling effect on the body. Perspiration maintains the body temperature when people feel hot. Perspirable Skin design proposed in this thesis behaves very similar to the perspiration of the human body.

The design requires a multifunctional material system, which is arranged in a 'Peg and Hole' fashion. The design includes a core material shrink-fitted into a skin panel such as Reinforced Carbon-Carbon Composite (RCC). The main design idea hinges on the core made of either pure ZrW_2O_8 or Functionally Graded Materials (FGMs) made of ZrW_2O_8 and ZrO_2. The choice of ZrW_2O_8 was due to its highly negative Coefficient of Thermal Expansion (CTE) in a wide range of temperatures [5] (0~1050K). When the surface temperature of Perspirable Skin increases during reentry, a gap is formed automatically between the core and the RCC skin, mainly due to the the difference in CTE values. The RCC skin will remain the same dimension because of the near zero CTE value. Once the

temperature reaches the working temperature, the generated gap can be introduced the onboard coolant gas onto the surface. The flow of coolant gas will cool down the high surface temperature. When the temperature is lower than the working temperature, the core part will expand so that the gap will automatically close to maintain the original shape of the assembly.

Furthermore, in order to increase the cooling efficiency, “thermal buckling” structure is introduced in this thesis, and by utilizing FGMs; the buckling structure can be triggered when the temperature exceeds the working temperature. It can open a much larger gap compared to the original “Peg and Hole” design [57]. Both the initial and optimized design for mimicking the perspirable skin will be discussed in details in chapter 2.

1.3. POWDER METALLURGY

Powder metallurgy is the process of blending fine powdered materials, pressing them into a desired shape or form (compacting), and then heating the compacted material in a controlled atmosphere to consolidate the material (sintering). The powder metallurgy process generally consists of four basic steps: (1) powder manufacture, (2) powder blending, (3) compacting, (4) sintering [6].

For the compressed powder, particles may vary in size and shape; thus, this is an important step to ensure that the properties will be uniform throughout the finished part [6, 7]. During the powder mixing step, some additives such as lubricants or binders may be

needed to the powder mixture. Lubricants can help to improve the flow characteristics. While binders help increase the strength of green sample. [7]

There are numerous shaping operations such as injection molding, extrusion, slurry techniques, freezing techniques, and compaction [8]. Among these, compaction is the most conventional and common way for the experiment, which is also used in this thesis. Powder compaction is the process of compacting ceramic powders in a die through the application of high pressures. Typically the powder is held between two punches in the vertical orientation forming the bottom of the cavity. The powder is then compacted into a shape and then the compacted powder is ejected from the die cavity [9].

The pressing techniques mainly include two kinds, hot pressing and cold pressing. Cold pressing is the most important compaction method in powder metallurgy. It starts from bulk powders containing very small or no lubricant or binder additions. The classical uniaxial compaction process is shown in a step-by-step fashion in Figure 1.3. The mixed powder is transferred to the die with the bottom punch inserted in it. The top surface is flattened before the insertion of the top punch. This is to ensure that the top punch would have maximum surface contact with the powder and evenly distribute the pressure during the compaction. After compacting at a certain pressure, the sample, which is called “green compact”, is ejected from the die for sintering. The final density of a green sample depends on the compaction pressure and the powder characteristics [7, 8].

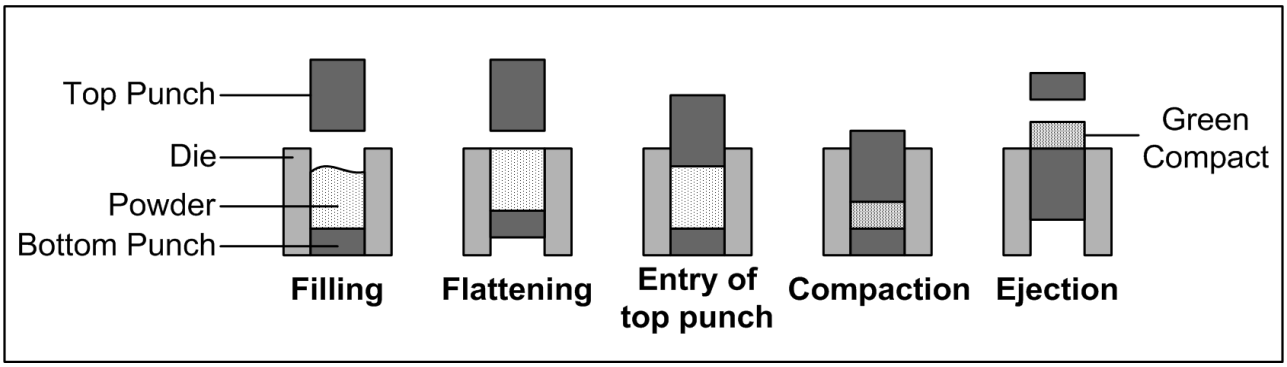

Figure 1.3. Cold uniaxial powder compaction process

After compaction, the green samples are not fully dense. Therefore, sintering will be employed to obtain a full density. Sintering is a thermal process that involves bonding of particles together at high temperatures by solid-state atomic transport phenomenon. The green compact is heated in a controlled-atmosphere furnace to the temperatures well below its melting point; however, under some certain requirements, the formation of a liquid phase might be involved. After sintering, the strength and final density can be improved significantly [7, 8] Sintering can be considered to proceed in three stages.

Coble [10] proposed three stages in sintering. During each stage, different sintering kinetics takes place.

1. The initial stage: The inter-particle contact area increases by neck growth. The relative density increases to about 65%.
2. The intermediate stage: Continuous pore channels are seen at the triple points (three-grain junctions) and relative density increases from 65 to 90%.
3. The final stage: Pore phase is eventually pinched off. Continuous pore channels disappear. Individual pores are either lenticular on grain boundaries, or rounded within a grain. Pore and grain boundary mobility increases dramatically at this stage.

Sintering kinetics is dependent on many variables [11], such as (1) temperature, (2) green density, (3) Atmosphere, (4) Particle size, (5) Phase transition.

For the green density, the higher the green density, the slower the densification rate. For the atmosphere factor, some sintering may require the vacuum atmosphere to prevent the oxidization, and the atmosphere can enhance the diffusivity sometimes [12]. Influence of particle size is that finer particles have more surface area than coarser particles, and thus the smaller particles will help sintering, like nanopowders. In practice, however, very fine particles may lead to agglomeration and it is very difficult to compact small particles due to the enhanced interparticle friction, which may lead a low green compact density. Normally densification rate will change as phase changes, like the densification rate will increase once we have liquid phase during sintering process [13].

During sintering procedure, some additives may enhance the sinterability and control the microstructure. Typical examples are the addition of Ni to W for improving sinterability, and the addition of MgO to Al_2O_3 for prohibiting abnormal grain growth and improving densification effects [14]. Some papers also mentioned that the densification could be improved by employing nanopowders additive due to the large surface energy offered by nanopowders. For example, the mechanical properties and microstructure of SiC ceramics can be successfully improved by including nano SiC powder and some oxides. The oxide additives system slightly enhanced the mechanical properties of the ceramics. The addition of nano-SiC lead to finer microstructure [15]. Another submicron silicon

carbide (SiC) was sintered to about 98% of its theoretical density with alumina and yttria as sintering additives. This densification was possible because of the liquid-phase sintering of a eutectic liquid formed between Al_2O_3 and Y_2O_3 at sintering temperatures [16]. Many oxides such as Al_2O_3, MgO, Lu_2O_3, Y_2O_3, Al_4SiC_4, and Al_2O_3–Y_2O_3 have been reported to form liquid phase assisted sintering [17].

According to the literature review, some sintering plans including adding the nanopowders and oxides were carried out to improve the mechanical properties and microstructures of sintered sample. It is verified that with the same improving mechanism, the final sintered density of zirconium tungstate can be enhanced by 10%.

In addition to the three main steps described above, other additional operations might be necessary for the process in order to have some specific shape or required dimensions to compose the assembly. These operations may include prototype manufacturing or surface finishing. In this thesis, the partially sintering and CNC machining techniques are utilized to obtain the sample we design, relevant details will be introduced in chapter 5.

According to our design, powder metallurgy is the most suitable method for manufacturing the core of the Perspirable Skin. The fabrication process is discussed in detail in Chapter 2 and 3. Additionally, the effects of powder mixing in the compaction capabilities of ceramic powders, as well as the additive on the final sintered density are investigated in Chapter 4.

1.4 SHRINK-FITTING TECHNIQUES

Shrink-fitting is a technique in which pieces of a structure are heated or cooled, employing the phenomenon of thermal expansion, to tightly join two pieces that are geometrically compatible [18]. It can also be explained as an important connection for many mechanical parts by utilizing a residual stress state or simply to connect different parts in a reliable and non expensive manner [19]. Many different methods and techniques can be employed to accomplish a shrink fit [20]. In a traditional shrink-fit technique, the outside container is heated to a high enough temperature to expand to accommodate the insert. In this thesis the shrink-fitting technique was used to obtain the FGM samples. The details will be interpreted in Chapter 3 when talking about the manufacturing process of functional graded materials.

1.5. RULE AND INVERSE RULE OF MIXTURES

Rule of Mixtures is a method of approaching to approximate estimation of composite material properties, based on an assumption that a composite property is the volume weighed average of the phases (matrix and dispersed phase) properties. These rules are extremely useful in assessment of the combinations of basic mechanical/physical properties that can be engineered via composite reinforcement [21].

According to Rule of Mixtures properties of composite materials are estimated as follows: Density, Coefficient of Thermal Expansion, Modulus of Elasticity, Shear modulus, Poisson's ratio, Tensile strength.

Density

$$d_c = d_m \times V_m + d_f \times V_f \quad (1.1)$$

where

d_i= *density of ,* composite, matrix and dispersed phases depending on i=c, m and f respectively;

Coefficient of Thermal Expansion (CTE) in longitudinal direction (along the fibers)

$$\alpha_{cl} = \frac{\alpha_m \times V_m \times E_m + \alpha_f \times V_f \times E_f}{V_m \times E_m + V_f \times E_f} \quad (1.2)$$

Where

α_{cl}, α_m, α_f – CTE of composite in longitudinal direction, matrix and dispersed phase (fiber) respectively;

E_m,E_f – modulus of elasticity of matrix and dispersed phase (fiber) respectively.

Coefficient of Thermal Expansion (CTE) in transverse direction (perpendicular to the fibers)

$$\alpha_{cl} = (1 + \mu_m) \times \alpha_m \times V_m + \alpha_f \times V_f \quad (1.3)$$

Where

μ_m – Poisson's ratio of matrix.

Poisson's ratio is the ratio of transverse contraction strain to longitudinal extension strain in the direction of applied force.

The inverse rule of mixtures states that in the direction perpendicular to the fibers, the elastic modulus of a composite can be as low as equation (1.4) [22]. It is not as accurate as the Rule of Mixtures because the equal stress assumption is not entirely valid – parts of the matrix will be shielded from stress by the fibers.

$$E_c = \left(\frac{f}{E_f} + \frac{1-f}{E_m}\right)^{-1} \quad (1.4)$$

The formulas are used to estimate the properties of the material simulated or made in our thesis, the calculation results will be discussed in details in chapter 2 and 5.

1.6 MORI-TANAKA SCHEME

Many micromechanics models have been presented to predict the effective or bulk physical properties of composite materials [23-29]. The work of Mori and Tanaka (1973), [23] originally focused on the calculation of average internal stress in the matrix materials, which contains precipitates with eigenstrains, now has been used to estimate the properties of composite materials. The Figure 1.4 shows the different simulating mechanism of the two prediction methods- rule of mixture and Mori-Tanaka Scheme.

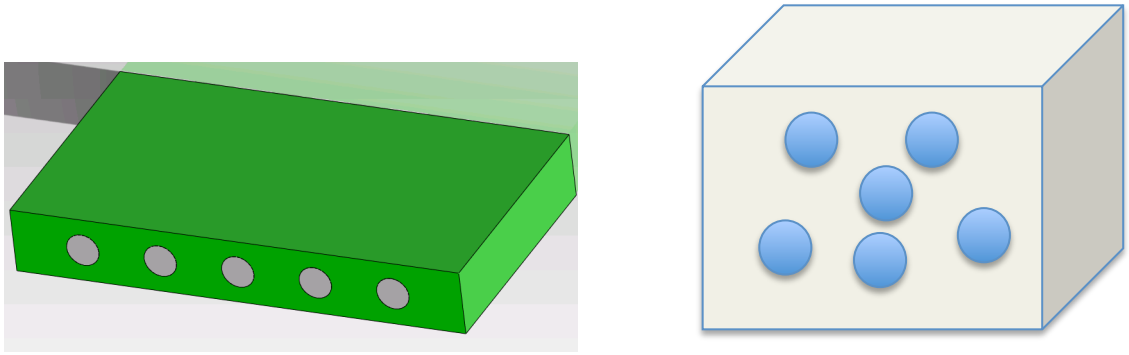

(a) (b)

Figure 1.4. Schematic illustration (a) Rule or Inverse Rule of mixtures; (b) Mori–Tanaka approaches.

The Mori–Tanaka method, which is suitable for particulate composite materials, with the slight modification applicable for high volume fractions, was applied to estimate the Young's modulus values of sintered porous sample. Based on Eshelby's [30] elastic solution for inhomogeneity in infinite medium, the fourth-order tensor relates average inclusion strain to average matrix strain and approximately accounts for fiber interaction effects.

The Mori-Tanaka Method was introduced with following equations to calculate the Young's modulus of the porous ZrW_2O_8, and make a comparison with experiment values. The effective stiffness tensor, $\boldsymbol{C_{ef}}$, is used to calculate the Young's modulus, *E*, for the stiffness matrix.

$$C_{ef} = C_m + v(C_i - C_m)A_i \quad (1.5)$$

Where $\boldsymbol{C_m}$ and $\boldsymbol{C_i}$ are the stiffness tensors of the matrix and inclusion materials as pores, respectively, v is the volume fraction of the inclusion phase. $\boldsymbol{A_i}$ is the inclusion strain concentrator tensor defined as

$$A_i = T[(1-v)I + vT]^{-1} \tag{1.6}$$

Where $\boldsymbol{I}$ is the forth rank identity tensor and $\boldsymbol{T}$ is Wu's tensor [33] defined as

$$T = [I + ES_m(C_i - C_m)]^{-1} \tag{1.7}$$

Where $\boldsymbol{E}$ is Eshelby's tensor decided by the shape of the inclusion, and $\boldsymbol{S_m}$ is the compliance tensor of the matrix material.

When applying the Mori-Tanaka scheme to a two-phase composite, one phase is the matrix and the other is the second phase. In metal matrix composites, the metal phase typically constitutes the matrix and the hard ceramics phase becomes the second phase. In case of ceramic-ceramic composites, the distinction between reinforcement and matrix phases may not be very obvious in the mid range (the volume fraction between 0.3 and 0.8). The second phase can become more and more continuous and finally becomes more like the matrix material as the volume ratio increases. When the volume ratio reaches a certain threshold, the role of each phase completely reverses. This threshold value depends on the volume ratio, the shape and morphology of each phase and the consolidation characteristic of each phase [31]. In real systems of materials, both phases can be continuous and thus one needs to define the degree of contiguity. By

incorporating the continuity η as a weighting function, Kwon et al. [29] revised the Mori-Tanaka method, producing the following model

$$C_c = C^+ + \eta(C^- - C^+) \tag{1.8}$$

where C^+ is the stiffness tensor calculated from Equation (1.8) by assuming one phase to be the matrix phase and C^- is the one by assuming that the same phase to be the second phase. The continuity η, which is ranging from 0 to 1, has been defined by Nishimatsu and Gurland [32].

1.7. FUNCTIONALLY GRADED MATERIAL (FGM)

A functionally graded material is defined as a composite material that has the distribution of the spatially varying second phase to attain macroscopically inhomogeneous properties [34, 35, and 36]. One of the main purposes of FGMs is to design the inhomogeneous properties of a material to tailor-fit for a particular loading condition [37]. In many high temperature applications, it is becoming more and more difficult to meet the highly stringent design requirements by using materials that are "homogeneous" in their bulk properties [38]. FGMs were conceived in late 1980s to be an ideal thermal barrier for space structure, fusion reactor or future space plane system in order to withstand severe temperature gradients while still retaining necessary mechanical integrity [39].

The processing of FGMs on a laboratory scale has reached a considerable level of maturity. Among many processing methods available today, the choice of processing

method depends on various factors such as the materials involved, the type and extent of gradiency and the dimensions of a component [40]. Miyamoto [41] categorized the fabrication methods of FGMs into bulk, layer, perform, and melt processing. Bulk processing [42-45] creates a bulk material with graded porosity, composition, or phase configuration, performed by forming stacks of powder, fibers, or even sheets by means of normal gravity, centrifugal forces, or pressure induced flow. Layer processing can be achieved by mechanical deposition through lamination and thermal spraying [46, 47] by the deposition of molecules or atoms with physical and chemical vapor deposition or with mechanisms based on electro-transport or chemical reaction. Preform processing is applied to initiate or to modify existing gradients in a preform. The conventional processing methods can be done in solid state, liquid phase, or vapor phase diffusion. Melt processing comprises elements of both constructive processing and processing associated with mass transfer. Gradual phase separation under normal or enhanced gravity can be treated similarly to sedimentation in particulate processing [48-49].

The powder stacking method is one of the bulk processing methods, which is used in this study. Powder metallurgy (P/M) is the most common processing technique used to fabricate stepwise ceramic FGMs [6]. The typical P/M processing steps to fabricate multi-layer materials are as follows: 1) stacking the powders layer-by-layer, 2) forming operations (usually a die compaction step) and 3) sintering.

Another method employed in making the FGMs is shrink-fitting techniques, which is already explained above. The specific characteristic of making FGMs in this thesis is we

utilize some components to react to generate the intermediate compound forming the solid boundary for the FGMs. The FEA modeling and the fabrication of the FGM core are discussed separately in Chapter 3.

1.8 EXPERIMENTAL FACILITIES

As we discussed in Section 1.3, typical techniques of P/M method include powder mixing, powder characteristics testing, compaction, sintering, mass and volume measurement, and microstructure observation. To perform these steps, various facilities were used.

1. Powder mixing was processed in a jar mill (U.S. Stoneware 764AVM, U.S.A.) using 12mm diameter zirconia mixing media for 48 hours at a 45rev/min speed, or by a Speed Mixer DAC 150.1 FVZ (FlackTek, Inc., USA) for 3 minutes (1 minute for each cycle and totally 3 cycles) at the angular velocity of 1700 rad/s. The minimum mixing amount needs to be no less than 10g. Different size of zirconia beads can be used during the mixing to break down the particle size.
2. Mass was measured by an electronic balance (Adventures AR2140, OHAUS Corp. USA). The resolution is 0.1mg.
3. Powder compaction was performed in a single-action die made by 1144 Stress Proof steel. There are three different dimensions for the die, which are 22mm, 19.10mm, and 7.94mm diameter. The smaller die was used to prepare the sample for further testing, like CTE character. The load to compact powder stacks was in the range of 60 to 210MPa, normally 70MPa, which was applied by MTS

Insight 300 (Maximum load 300KN, MTS Systems Corp. USA). The compaction speed of MTS Insight 300 was 5mm/min and the stress resolution is 0.013MPa. A small amount of pressure 0.5MPa will be applied sometimes to obtain a stable state when measuring the relative density for green samples.

4. Green compacts were sintered in air furnace (Carbolite-HTF1700, UK) or vacuum furnace (Top loading vacuum furnace/3000^{o}C). The temperature control resolution for the open-air furnace is 1^{o}C, and the ramp rate can set up to as high as 15^{o}C/min. For the vacuum furnace from Materials Research, the chamber needs to be filled with argon gas during sintering to protect the graphite boundary. The temperature control resolution is 0.1^{o}C, and the ramp rate can set up to 30^{o}C/min among the high temperature range.
5. The thickness and diameter of samples were measured by a MARATHON electronic digital caliper. The resolution is 0.01mm.
6. The volumes of the fully-sintered samples were measured in water using Archimedes' principle. The resolution is 0.10cm^{3}.
7. To attain clear micrographs, the fully-sintered samples were thermal-etched in a box furnace (Carbolite-HTF1700, UK). Different materials require different thermal-etched temperature, and usually the temperature range is 300-600^{o}C.
8. The microstructure of a sintered sample was observed by Scanning Electron Microscopy (JEOL 6400V, Japan).
9. Real time sintering testing was performed using a Thermo-mechanical Analysor (TMA) SETARAM SETSYS Evoluation 95 to examine the densification rate and

the coefficient of thermal expansion for sintered sample can also be tested by TMA, with argon gas providing a protective environment.

10. The pre-sintered sample was prepared and cut with CNC machine (Emco group PC Mill 50) into a designed shape to make the assembly. Different cutting speeds and feed rates were used based on different materials. Details will be interpreted in Chapter 5.

CHAPTER 2 PERSPIRABLE SKIN DESIGN

2.1. MATERIAL SELECTION FOR THE CORE

As we discussed above, the core part of the prespirable skin should be a negative CTE material in order to have thermal dimension difference with the outside RCC part. There are several materials that exhibit negative CTE properties. Table 2.1 below shows some of the NTE materials.

Table 2.1. Isotopic negative thermal expansion materials [50-56]

Material	CTE range (10^{-6} K^{-1})	Temperature range (K)
ThP_2O_7	-9.3 to 4.3	573-480
UP_2O_7	-7.1 to 3.1	773-1773
ZrV_2O_7	-11.1 to 15.4	380-875
$Cd(CN)_2$	−33.5	170-375
$(HfMg)(WO_4)_3$	-2	290-1070
ZrW_2O_8	-13.2 to -6.5	3-1050
HfW_2O_8	-12.9 to -6.4	3-1050

Among these materials, ThP_2O_7, UP_2O_7, and ZrV_2O_7 are not suitable for being chosen as the cores due to their low CTE ranges; and we could notice that at higher temperatures they will change to positive CTE materials automatically. In addition, the

range of their working temperature is too narrow to meet the requirements of the reentry for space shuttle. $Cd(CN)_2$ exhibits a large NTE values while at the same time its working temperature is too low. Despite of its wide working temperature range, $(HfMg)(WO_4)_3$ is not fit for our problem due to its low negative CTE values. Both Hafnium (Hf) and Zirconium (Zr) meet the required working temperature range and exhibit a good negative CTE range. Because Hf is more rare, ZrW_2O_8 would be chosen as the best fabricating material for the perspirable core.

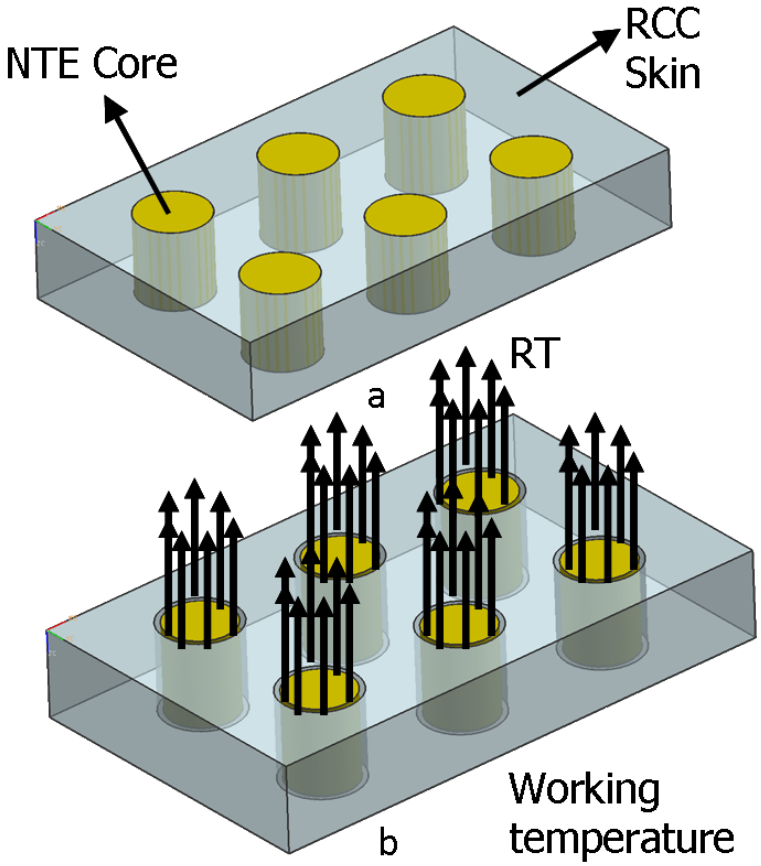

Figure 2.1. Schematic drawing of the fundamental design concept. (a) When the skin is closed at room temperature; (b) opened at working temperature [57]

2.2. RESULTS FROM PREVIOUS STAGE

Due to the limitation of current TPS, a better system design is proposed to enhance the durability and reliability of the space shuttle. Similar to the sweat to maintain the temperature of human body, the new TPS can have a self-cooling function. In the early stage of this project “Perspirable Skin”, Sun and Oguz [57, 58] proposed the design of the perspirable skin to be a multifunctional material system, which is arranged in a “peg and hole” fashion. Based on this design, a gap is generated successfully when FGM sample is employed to make the core part. The designed details about FGM sample are shown in Figure 2.2.

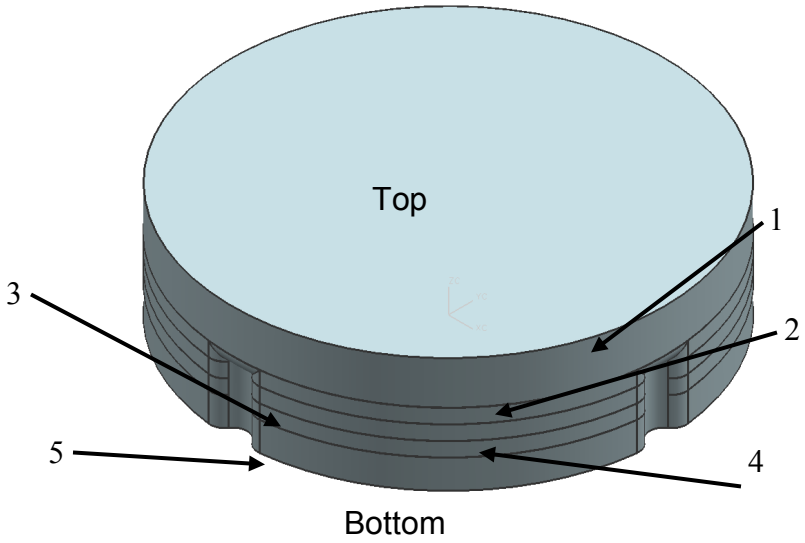

Figure 2.2. Final design of the FGM core with channels for coolant gas to flow through [57] (number listed refer to table 2.3)

In order to maintain the core part its position in the perspirable skin design, the core need to be made with slightly positive CTE values on the bottom, which means the shrinkage occurred is relatively minute compared to the top. During the working procedure, the core will remain in contact with the surrounding RCC skin from the bottom part while a gap is already generated near the exterior surface which has shrank. To let the coolant gas coming out from the gap, four semi-annular channels are incorporated into the core to help the cooling effect.

2.2.1 Material Properties for RCC

In order to run the simulation of our model correctly, the material properties such as CTE values, young's modulus, Poisson ratio, of each part are investigated.

The fiber arrangements of optimized RCC included 3-D orthogonal, 2-D fabric laminated, and isotropic.

Table 2.2. Various parameters of RCC used in FEA [59]

Designation	Young's Modulus (GPa)		Shear Modulus (GPa)	CTE ($10^{-6}K^{-1}$)	
	Longitudinal	Transverse		Longitudinal	Transverse
2D Fabric Laminate	118	4.1	6	1.3	6.1
3D Woven Orthogonal	55	96	17.5	1.3	1.3
3D Isotropic	14	-	-	2E-7*	2E-7*

* Testing results by the TMA

Most properties of the RCC used in FEA were taken from the report of Sheehan et al. [59], such as the elastic modulus, shear modulus and CTE, which are listed in the Table 2.2.

2.2.2 Material properties for ZrW_2O_8

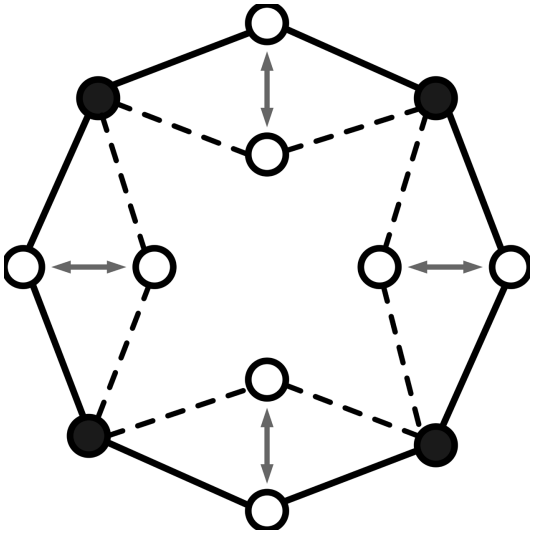

Figure 2.3 Schematic of thermal contraction caused by thermal motion (filled circles are cations, and open circles are oxygen atoms. The solid line shows low temperature bonds position, dash line shows bonds at high temperature and arrows show the vibration direction of oxygen atoms) [60].

The shrinking mechanism for NTE materials is interpreted as follow. The M-O-M linkage is the basis for the isotropic negative thermal expansion of the ceramics in Table 2.1. For ZrW_2O_8, the M-O-M linkage is Zr-O-Zr or W-O-W. The materials listed in table 2.1 have several structural characteristics in common: 1) the crystal structure is an open,

low-density framework structure; 2) the coordination of oxygen is only two-fold; and 3) the M-O bond is very strong. These characteristics will lead to two intimately related consequences: 1) The thermal expansion of the M-O bond will be very low, and the thermal vibration of oxygen will be very low in the directions of the M atoms; and 2) thermal vibration of oxygen perpendicular to the M-O-M linkage must be very high. With these unique thermal motions, the material will exhibit negative thermal expansion as the temperature increases [50, 51, 60].

Most thermo-mechanical properties of ZrW_2O_8 were experimentally determined. The CTE and Young's modulus of the ZrW_2O_8 were measured using a Thermal Mechanical Analyzer (TMA: Setaram 95, France) with the heating and cooling rates of 1°C/min in the argon gas environment.

The Young's Modulus of ZrW_2O_8 was found to be approximate 4.31GPa at room temperature [58]. The CTE-temperature relationship of ZrW_2O_8 is shown in Figure 2.4. It is indicated that ZrW_2O_8 is a negative material and have a wide range of working temperatures except the sharp change around 160°C due to the **α**- to **β**- ZrW_2O_8 phase transition [61]. The CTE of the ZrW_2O_8 at room temperature is $-8.09 \pm 0.65K^{-1}$.

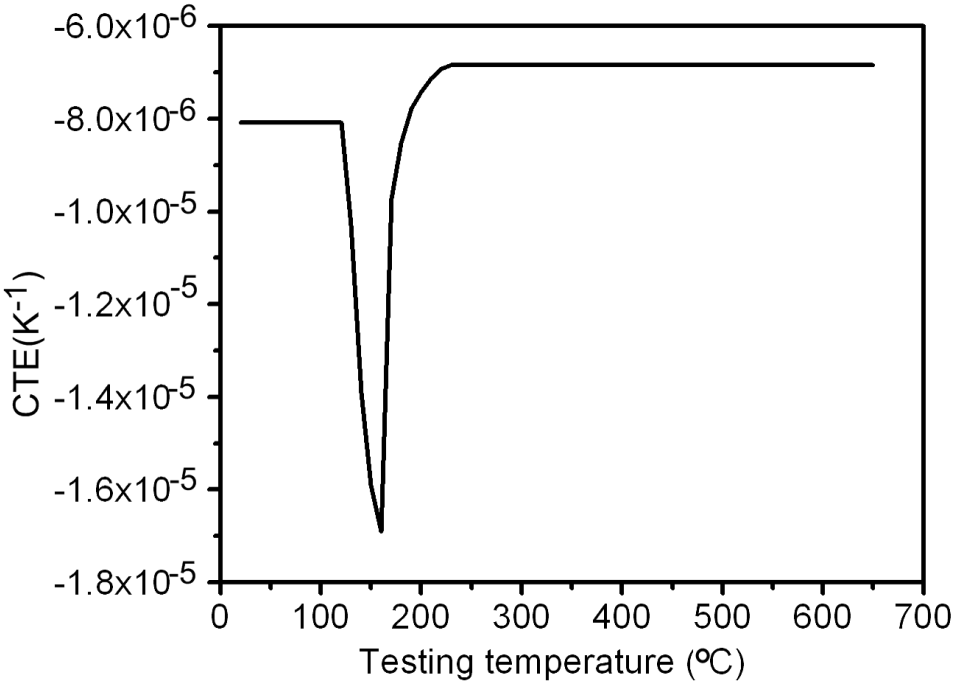

Figure 2.4. The temperature dependence of the CTE of ZrW_2O_8.

The high temperature thermal conductivity of ZrW_2O_8 was measured using the laser flash method (FlashLine 5000, USA) from room temperature to 710°C. The results are shown in Figure 2.5 (*Test was performed by Dr. Xun Shi at Prof. Uher group at University of Michigan, USA*).

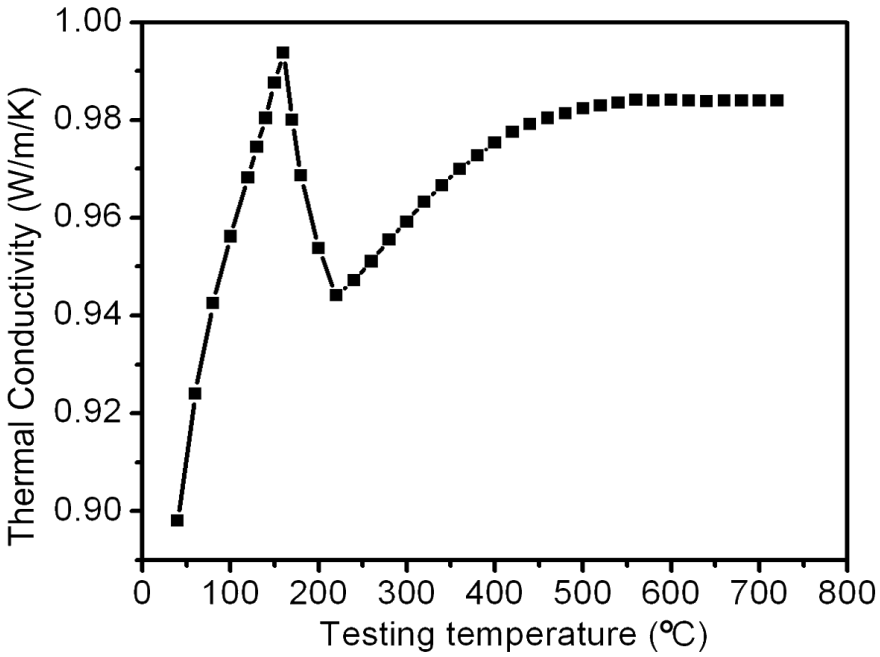

Figure 2.5. The temperature dependence of thermal conductivity of ZrW_2O_8

The Poisson's ratio was taken as 0.3 from the report of Drymiotis et al [62]. Then its shear modulus (G) was calculated using the Young's Modulus and Poisson's ratio.

2.2.3 Simulation of the original design

The FEA simulation based on the design is also done to verify the shrinkage and the gap generated. The highest working temperature for the perspirable skin is estimated to be around 750 °C to 780 °C because the compound ZrW_2O_8 would dissociate at around 777 °C [57].

In this thesis, to produce pure ZrW_2O_8, the ZrO_2 and WO_3 powders are mixed in the stoichiometric ratio of 1:2 as the layer 1 (mass ratio is mWO_3: $mZrO_2$ =1:0.266) [63]. The other ZrW_2O_8/ZrO_2 mixtures with other volume ratios are also shown in Table 2.3 below. They are the compositions to make the each layer for the FGM we design.

Table 2.3. Design parameters for FGM core

Layer number	ZrW_2O_8/ZrO_2 Volume Ratio	Thermal Conductivity (W/m/K)	Young's Modulus (GPa)	Thickness (mm)
1	100:00	0.9672	4.12 ± 0.13	3
2	88:12	1.0696	3.65 ± 0.13	1
3	76:24	1.1346	3.18 ± 0.10	1
4	64:36	1.2099	2.71 ± 0.08	1
5	52:48	1.4531	2.24 ± 0.08	2

(layer 1: top layer; layer 5: bottom layer)

For the loading condition in the simulation, the top layer of the core was exposed to a temperature of 760 °C and the bottom layer was set to a constant temperature of 100 °C.

The ABAQUS simulation shown in Figure 2.6 represented one quarter of the design because the setup was axis-symmetric. The result showed that a gap was generated through the thermal loading condition while the bottom still remained contact with the skin. The maximum gap we can get from the simulation is approximately 100 μm (100×10^{-6} m); in addition, the maximum stress is 9.75MPa.

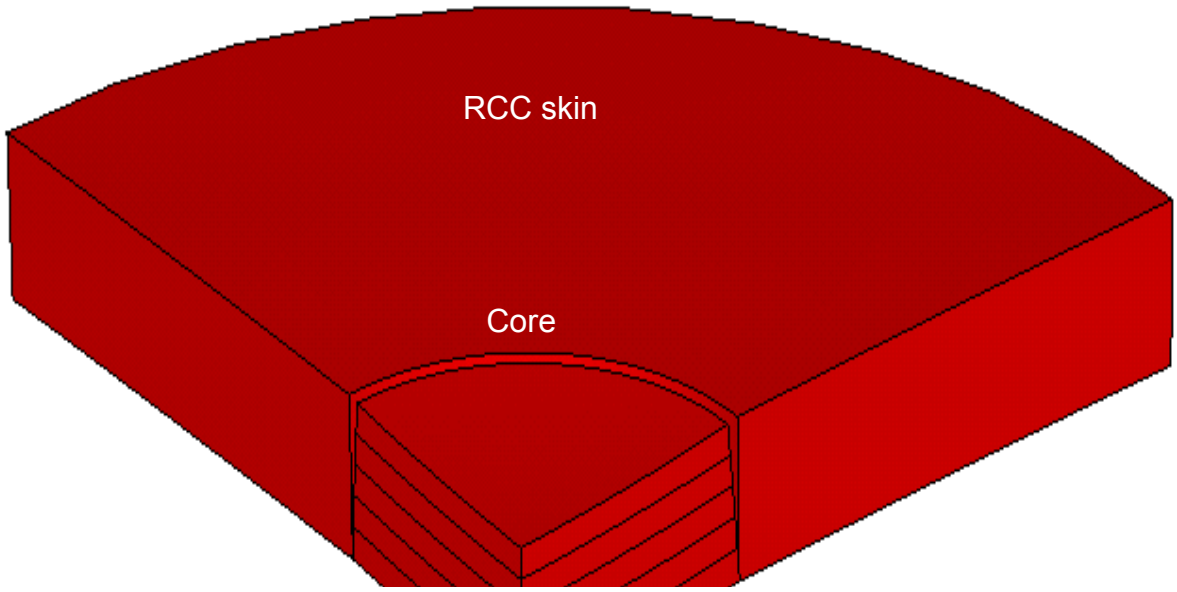

Figure 2.6. ABAQUS simulation of the perspirable skin [57]

2.3. NEW PRESPIRABLE SKIN DESIGN WITH BUCKLING IDEA

The previous design had the core made of ZrW_2O_8 shrink-fitted into the RCC. When the temperature increases, a gap is formed between the core and the RCC skin due to the distinct CTE difference. An onboard coolant gas can then be passed through this gap onto the surface of the vehicle, which will envelop the surface to prevent additional frictional heating. Because most of the high temperature materials available have limited CTE ranges (typically in 10^{-6}/°C), the gap generated by this simple in-plane thermal deformation could not achieve a high capacity for cooling. Therefore, a new design concept is proposed to drastically improve the cooling capacity by utilizing a buckling action. The core will be replaced with an assembly of tiles, which will buckle

under a given thermal loading. These tiles will be made of ZrW_2O_8 and/or complex/multidimensional FGMs, which are critical in our design.

The property gradient in FGMs typically changes in one direction. In this thesis, a novel processing technique is developed to achieve complex FGMs for the tiles used for our Perspirable Skin using the reaction between ZrW_2O_8 and ZrO_2. The partially sintered sample allows us to machine the part into their desired shapes. These shapes are designed to shrink-fit one with the other to form the complex gradiency of FGMs. The requirements of our tiles are unique such that they have to exhibit high positive thermal expansion radially and modest negative thermal expansion circumferentially. The reason for a negative circumferential CTE is to avoid the tiles getting stuck with the core during the buckling. In addition, the tiles is designed to have a through-the-thickness gradiency - higher thermal expansion on the exterior surface and negative thermal expansion on the interior surface - to trigger the required buckling action. The next chapter will describe the detailed processing steps of the FGM tiles and the steps we have taken to reduce the distortion to improve the shape of the model.

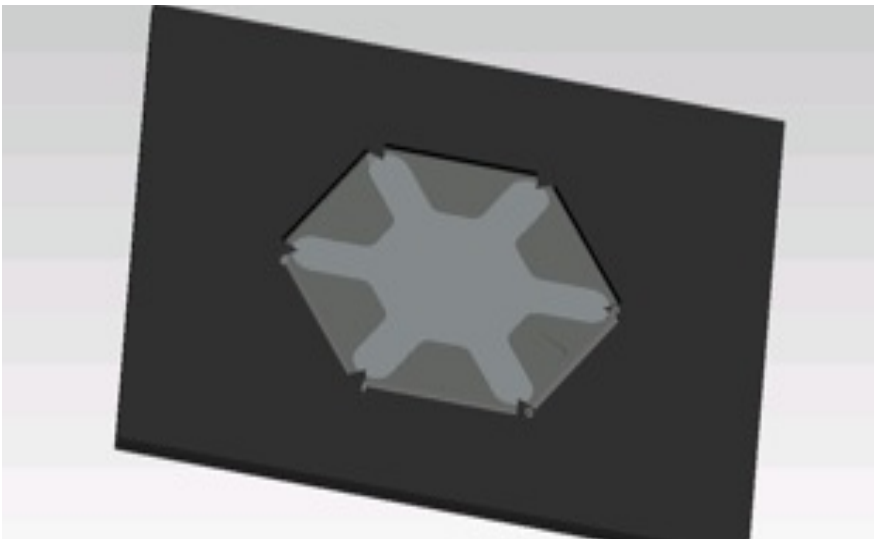

(a)

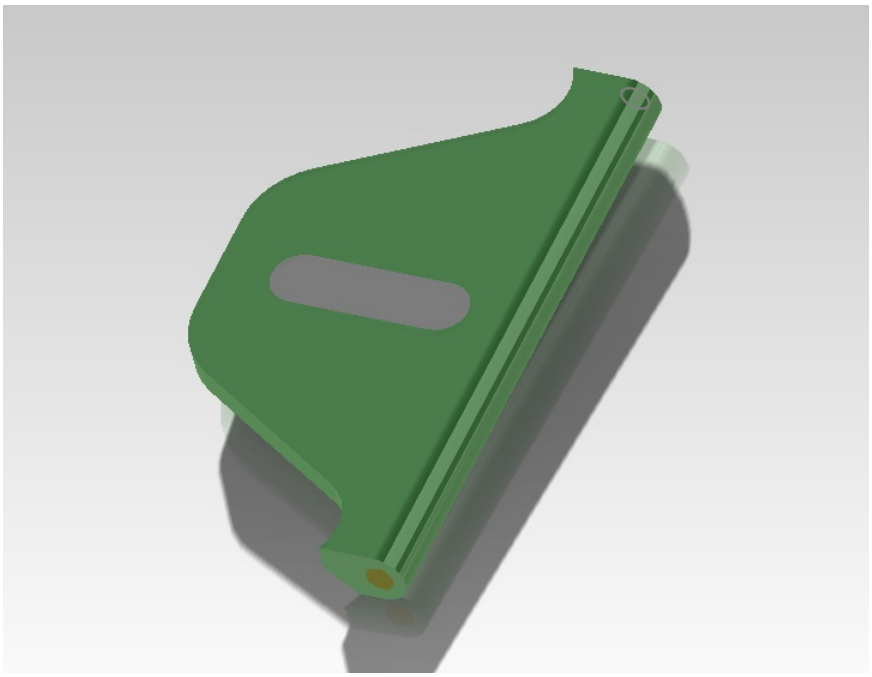

(b)

Figure 2.7. Buckling simulation: (a) original geometry representing the perspirable skin before buckling (b) designed tile part with ZrO_2 core (c) the geometry after buckling.

Figure 2.7 (cont'd)

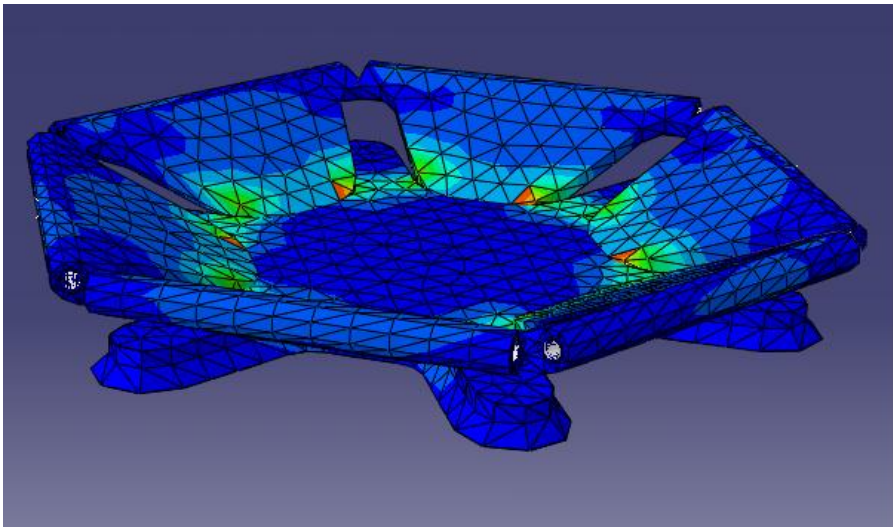

(c)

A buckling action can be achieved by a designed set of tiles as shown in Figure 2.7(a) with the RCC surface surrounding the tile assembly. When heated externally, the RCC, whose CTE is near zero, does not change its shape. The tile assembly, whose tiles have high positive CTE in the radial direction and modest negative CTE in the circumferential direction, will also be heated and put a compressive load radially. Consequently, the tiles will exert high enough radial force to buckle in order to generate large openings.

To enhance the buckling, the tiles with designed gradient materials consist of positive (e.g.: ZrO_2) and negative CTEs (e.g.: ZrW_2O_8) materials. For the preliminary analysis, the material properties used in our simulation were calculated and presented in Table 2.4 using the rule and inverse rules of mixture (ROM and IROM), which provide the two

extreme arrangements of two materials [10]. The volume ratio between ZrW_2O_8 and ZrO_2 was assumed 7:3, and with the formula introduced above, we obtained the material properties for each part.

Table 2.4. Material properties for the simulation

	Radial (ROM)	Circumferential (IROM)
CTE(/°C)	5.4e-6	-6e-6
Thermal conductivity (W/m/K)	5.6	2.7
Elastic modulus (MPa)	15.92	5.63
Poisson ratio	0.3	

The model was constructed with the properties from the rule of mixture in the radial direction and the properties from the inverse rule of mixture in the circumferential direction and the core tile is constructed with ZrO_2 only. The buckling simulation was performed with ABAQUS and the results are shown in Figure 2.6(c). In the FEM simulation, for the loading condition, 800°C was applied to the exterior surface and 50°C on the interior surface. Each tile was assigned an axis fixed to the surrounding RCC. With these loading and boundary conditions, the simulation results confirm the buckling action, and validate the design intent.

CHAPTER 3 POWDER METALLURGY OF FUNCTIONALLY GRADED MATERIALS AND ASSEMBLY

3.1. INTRODUCTION

Based on the simulation results, the tiles with the CTEs different in two directions are needed for the design. Two processing methods were considered for the tiles as represented in Figure 3.1. The first procedure starts by combining ceramic powders with ceramic fibers. With the fibers arranged radially, a positive CTE can be obtained along the fiber direction. This method was deemed unsuccessful due to the chemical reactions and residual thermal stresses between the fibers and matrix demolishing the samples during sintering. The other method requires sintering and shrink-fitting multiple tile components made of ZrO_2 and ZrW_2O_8 together to obtain distinct CTEs in different directions within the tile media. Based on this method, design optimization is also planned in order to enhance the buckling action. In addition, the powders distinctly different in average particle size were mixed with the two primary powders to alter the sintering behavior while minimizing the distortion that the samples experience during this phase. Table 3.1 lists several ceramic powders and fibers used in this study.

3.2. MATERIALS AND EXPERIMENTAL PROCEDURE

Table 3.1. Characteristics of Raw Powders

Name	Material	Mean particle size (μm)	Manufacturer
W-Fluka	WO_3	8.22	Sigma-Aldrich, U.S.A.
TZ3YS*	ZrO_2	0.56	Tosoh Co., Japan
CERAC-2003*	ZrO_2	1.23	CERAC Inc., U.S.A.
Nextel 610	Al_2O_3	½" chopped fiber	3M company
SCS-6	SiC	142	Specialty Materials, INC.

*Stabilized by 3w% Y_2O_3.

The 2:1 stoichiometric ratio of WO_3 and ZrO_2 is needed to produce pure ZrW_2O_8. The powders were mixed with 12mm-diameter zirconia media in a jar mill (U.S. Stoneware 764AVM, U.S.A.) for 48 hours. Before combining the powders with fibers, the fibers were heated to 600°C for two hours to remove any organic sizing [64].

The mixture was then stacked in a single-action die and chopped fibers were placed along one direction. The powders were compacted under 70MPa pressure. Green compacts were then sintered at 1150°C for 6 hours in a covered platinum crucible under atmospheric pressure in a furnace (Carbolite-HTF1700, UK). The covered crucible provided the nearly sealed environment required to reduce the sublimation of WO_3 at temperatures higher than 800°C [65]. Since the decomposition of ZrW_2O_8 takes place when the temperature is lower than 1100°C, a quenching process, performed by

removing the crucible out from the furnace after sintering, was necessary to prevent decomposition at lower temperatures and produce pure ZrW_2O_8.

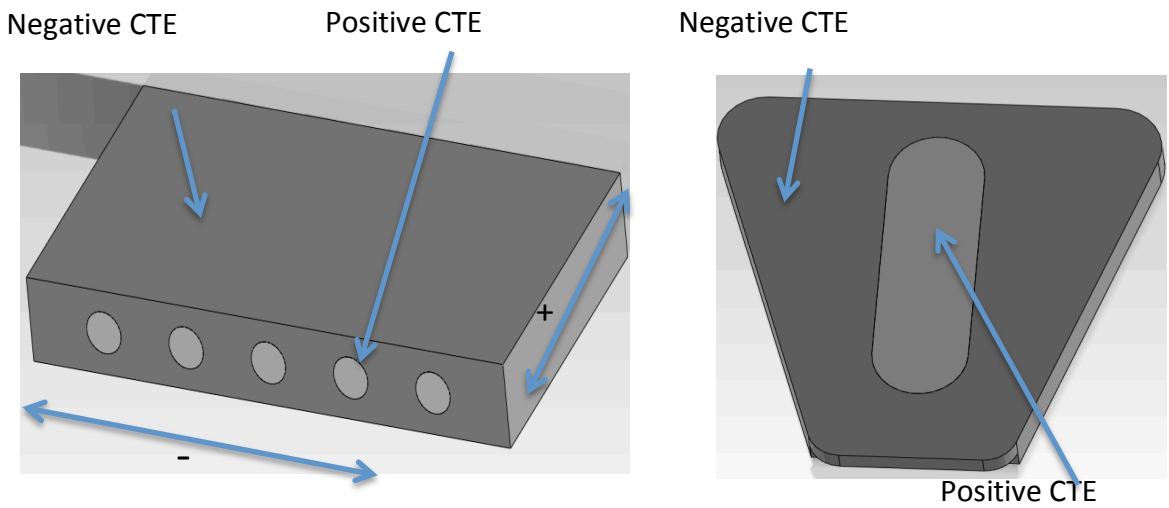

(a) (b)

Figure 3.1. Processing (a) ceramic powders with fibers; (b) shrink-fitting technique exhibiting negative CTE in the vertical direction and positive CTE in the horizontal direction

Another way to achieve inhomogeneous media uses shrink-fitting technique. From our previous work [66], we were able to make continuous FGMs between ZrO_2 and ZrW_2O_8. Because of the reaction between ZrO_2 and ZrW_2O_8, they can be intimately joined, which enables us to fabricate more complex FGM media for the tile design using this shrink-fitting technique. Two processing techniques were explored.

First, the WO_3+ZrO_2 powder mixture was first compacted under 70MPa, partially sintered at 950°C for four hours, and subsequently CNC-milled to have a certain shape

which will later accommodate the ZrO_2 sample. The partially sintered sample has turned into partially sintered ZrW_2O_8. The ZrO_2 sample was prepared also by partially sintering at 900°C for three hours and was then machined to fit the partially sintered ZrW_2O_8. After machining, the ZrO_2 sample was fully sintered under 1350°C for four hours and then inserted into the ZrW_2O_8 sample. These two materials were then co-sintered under 1150°C for 3 hours. By controlling the dimensions of each part during partial-sintering and subsequent full- sintering, the tiles are produced by precisely controlling the ZrW_2O_8 shrinkage and ZrO_2 expansion during the sintering process. A reaction layer was formed at the boundary between the ZrW_2O_8 and ZrO_2, which aids these two materials in joining together.

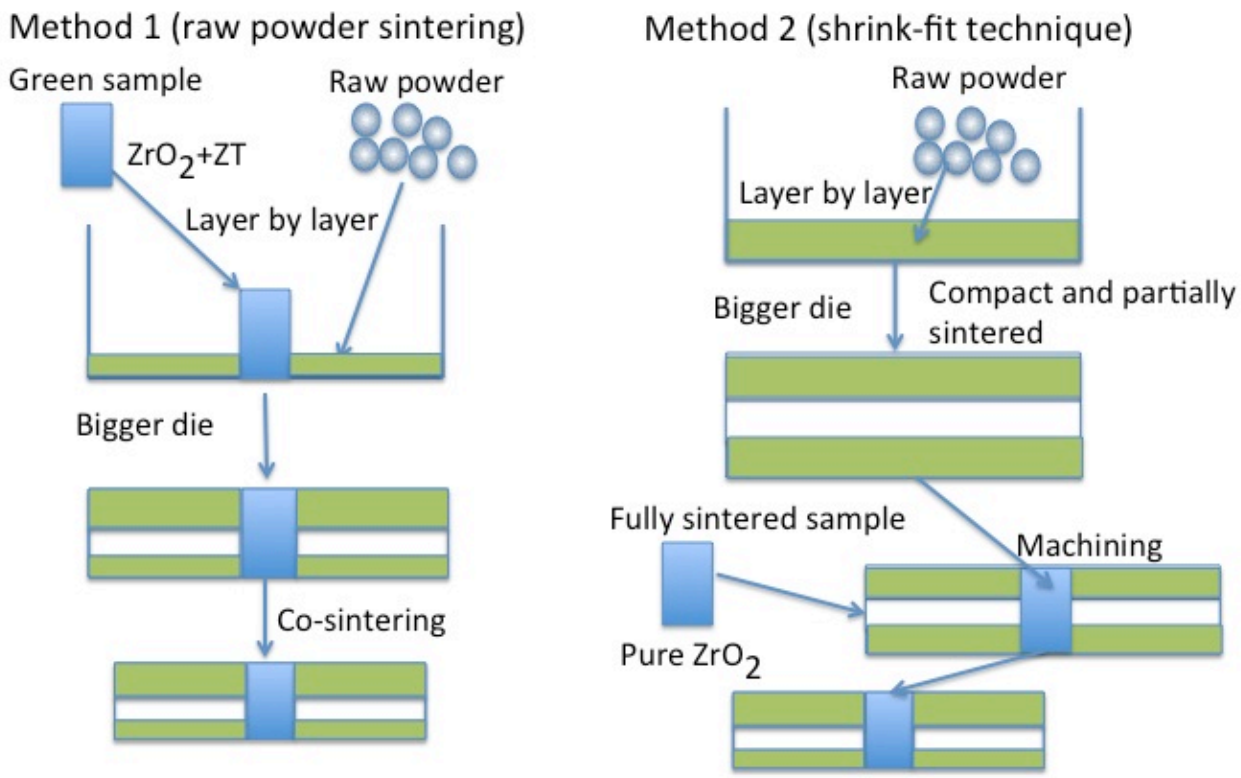

Figure 3.2. Multi-dimensional gradiency fabricating alternatives

The other processing technique involves (1) compacting the mixture (50%ZrO_2+50% ZrW_2O_8) in a small die (d=7.94mm) under 70MPa loading pressure to make core, (2) placing the core in the middle of a large die (d=19.10mm), and (3) filling a larger die with three powder layers, pure ZrW_2O_8, 80%ZrO_2+20% ZrW_2O_8 and another pure ZrW_2O_8, (4) compacting and sintering them at 1150°C for 2 hours.

3.3. RESULTS AND DISCUSSION

3.3.1 Sintered FGM sample with shrink-fitting technique

From the WO_3 and Al_2O_3 bi-phase diagram [67], $Al_2(WO_4)_3$ can only exist at a temperature higher than 720°C, and these alumina fibers will react with the WO_3+ZrO_2 mixture to become a liquid compound around 1150°C. The reaction will destroy the shape of the sample as shown in Figure 3.3(b). For the SiC fibers, with small amount, the sample maintains its shape as shown in Figure 3.3(a). With more SiC fibers, the residual thermal stress is greater during sintering. Because the high positive CTE value through radial direction requires a lot of fibers in the tile, SiC fibers cannot be used to fabricate the tiles for this application.

Figure 3.3 presents the samples constructed using a shrink-fitting technique; Figure 3.3(c) is a simple sample. ZrW_2O_8 was partially sintered, through which a hole was drilled. After 3 hours of co-sintering, the sample was shrink-fitted by placing the fully sintered ZrO_2 in the machined hole of the partially sintered ZrW_2O_8 tiles. Two main phenomena were observed in our samples. From our previous work [66], the ZrO_2 powder reacts with diffused tungsten during the sintering process. Instead of the pure white color indicating ZrO_2 powder, the core component has a yellow ring surrounding it, which signifies a reaction of ZrO_2 and ZrW_2O_8. Therefore, a desired FGM was generated from a composition of pure ZrW_2O_8 to pure ZrO_2 with a mixture of ZrO_2 and ZrW_2O_8. This FGM helps to join the two parts together, and the extent of reaction can

be controlled by adjusting the sintering temperature and soaking time.

White surface spots present on the surface of ZrW_2O_8 are another notable observation. This is due to the sublimation of WO_3 during the partial sintering and full sintering processes, since it is known that tungsten will dissociate and diffuse above 800°C. Therefore, the white spots present on the surface are ZrO_2 after loosing tungsten in ZrW_2O_8. The sample shown in Figure 3.3(d) is the tile designed in our simulation, shown in Figure 2.7. The key part of this process is that we need to compensate for the size change during the partial and full sintering processes. After many attempts, the ZrO_2 sample fit perfectly into the shape after it is fully sintered.

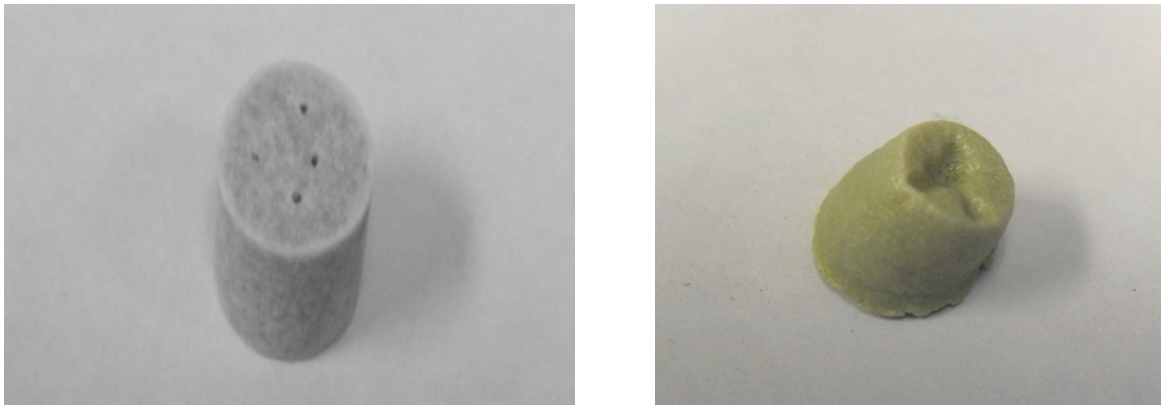

(a) (b)

Figure 3.3. (a) Results for ZrW_2O_8 with SiC fibers, (b) Results for ZrW_2O_8 with alumina fibers, (c) shrink-fitting samples: simple one with a ring shape, (d) a designed shape model to mimicking the tile part in the simulation

Figure 3.3 (cont'd)

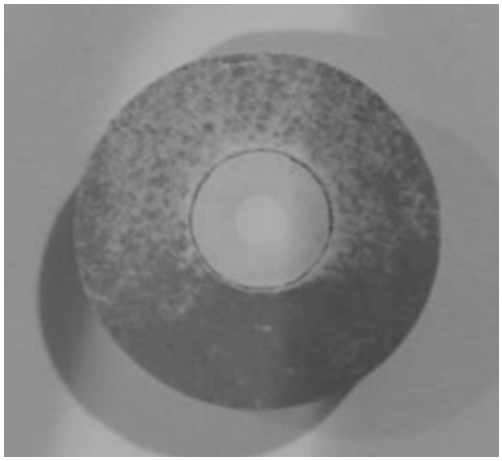

(c)

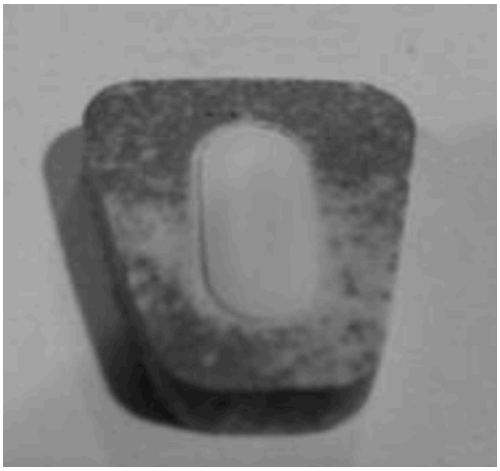

(d)

The reaction between ZrO_2 and ZrW_2O_8 may change the macroscopic CTE values critical to cause buckling. Thus, the geometric shape of the sample shown in Figure 3.3 (c) was imported and simulated using COMSOL to confirm the theoretical thermal expansion coefficient of the sample. The COMSOL result shows that the CTE value through the radial direction was $-3.95*10^{-6}$. To verify the simulation result, CTE values were also measured using the thermomechanical analyzer machine. Through the radial direction, the measured value was $-3.5*10^{-6}$. Compared with the simulation results, the slightly higher CTE in the radial direction is mainly due to the sublimation of WO_3 during the partial and full sintering process. In the thickness direction, the CTE value was measured on the ZrO_2 part to be $5*10^{-6}$, which is lower than the CTE value of ZrO_2 (around $7*10^{-6}$). The reason for the lower CTE value is due to the ZrW_2O_8 components surrounding the ZrO_2 component, which constrains the expansion when temperature

increases.

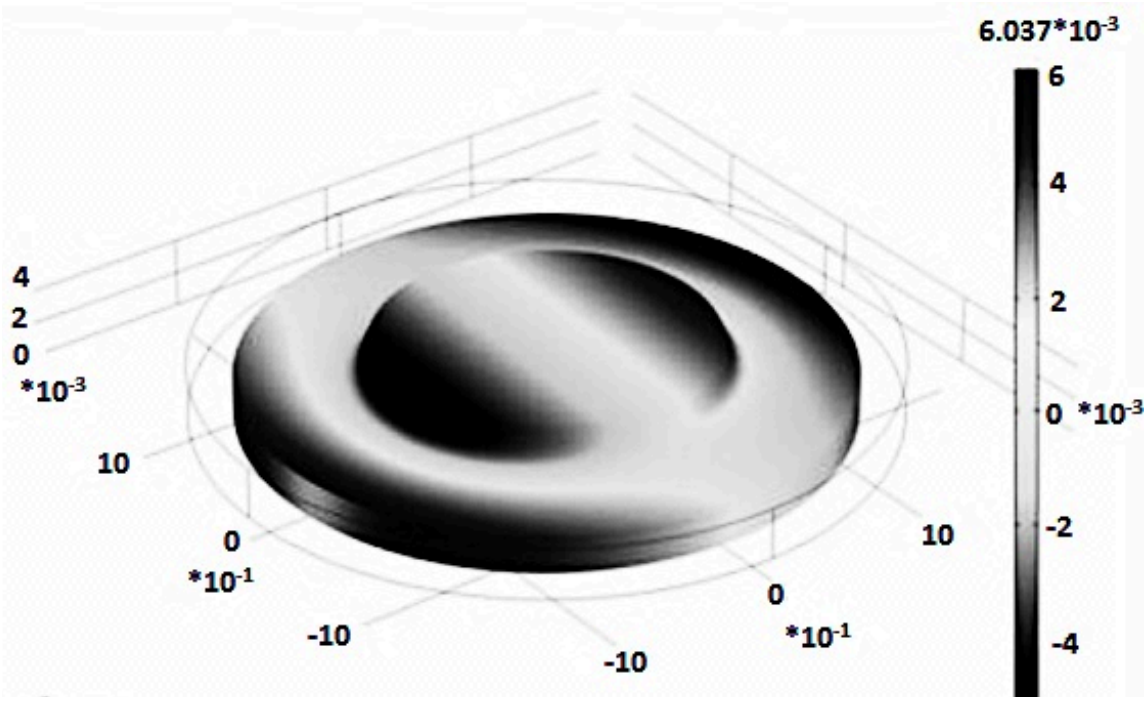

Figure 3.4. COMSOL simulation for radial CTE

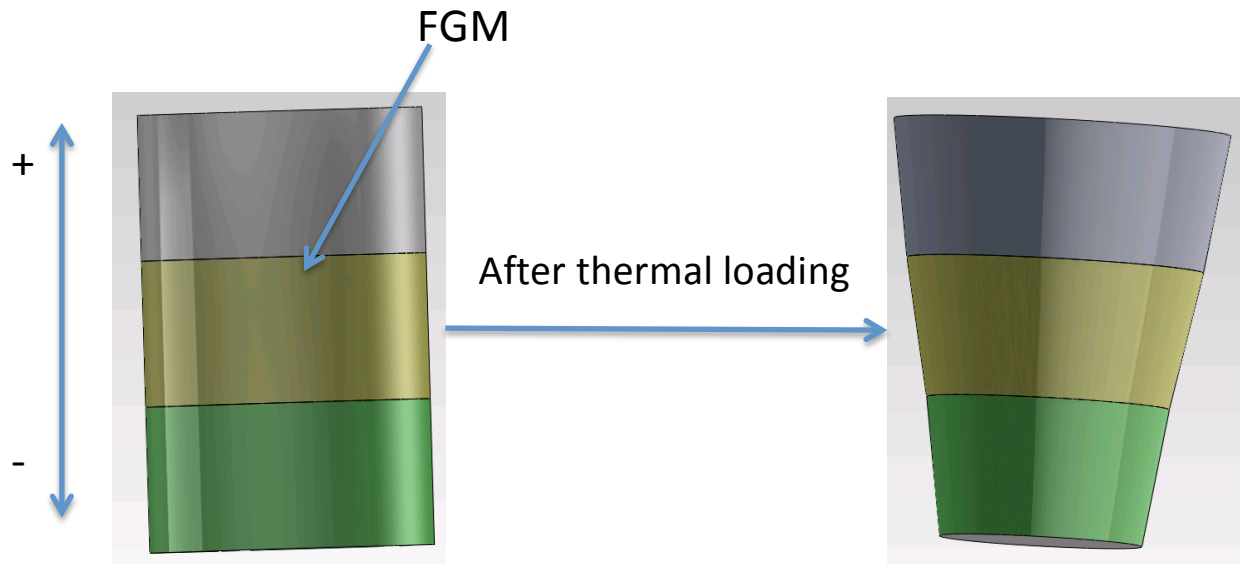

Figure 3.5. Buckling action enhanced by utilizing FGM through thickness direction

To obtain a large negative CTE value, one can sinter the sample in a furnace full of

tungsten-rich gas, which will reduce the sublimation of WO_3 powder. Another method is to decrease the proportion of ZrO_2 powder in the reacted mixture so that, the compound will have the exact moles of each component to obtain pure ZrW_2O_8 even after losing a certain amount of WO_3 powder by sublimation. However, this method is relatively difficult to control.

3.3.2 Sintered FGM sample using conventional method (layer by layer)

As shown in Figure 3.5, the buckling action can be enhanced if we can employ the FGM through thickness direction. The top layer with positive CTE will expand with a thermal loading, while the bottom negative CTE layer will shrink. This behavior will easily lead to the contact condition between core and tile parts from surface contact to almost line contact, which will definitely help trigger the buckling action.

The complex FGMs can change their properties in two directions, thickness and radial directions. Using the second method described above, complex FGM samples were successfully fabricated. Figures 3.6 and 3.7 showed the side and top view of the complex FGM sample we have produced. We can extend this method to continue adding more transition layers to make smoothly varying FGMs.

The tile components of the assembly must be in tight contact to avoid gas leaks. Thus it

is conceivable to use a form of gasket. This contact must be disengaged to promote a buckling action upon heating. The gradiency through the thickness direction with a strong positive CTE at the exterior surface and a slightly negative CTE at the interior surface is also needed. This can be achieved by simply increasing the proportion of ZrO_2 powder at the top.

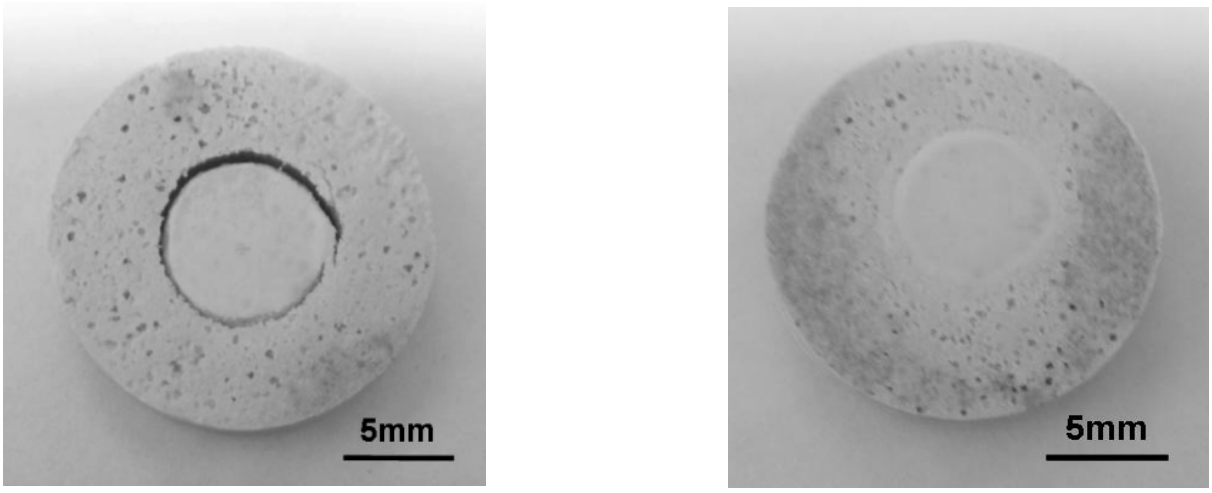

(a) (b)

Figure 3.6. Top view of the complex FGM sample: (a) core component (20% of $ZrW_2O_8$and 80% of ZrO_2 (20% of CERAC, 80% of TY3ZS)); (b) core component (50% of ZrW_2O_8 and 50% of ZrO_2 (10% of CERAC, 90% of TY3ZS))

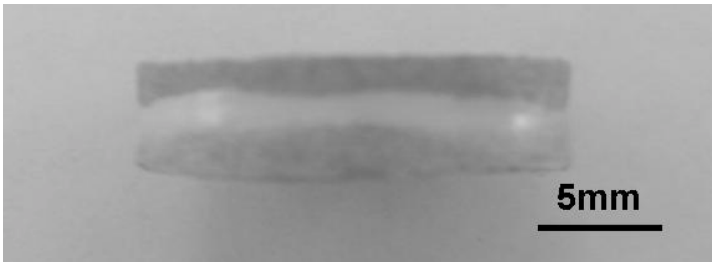

Figure 3.7. Side view of the complex FGM sample (refer to Figure 3.6 (b)).

We can examine the differences between the Samples 1 and 3 in Figure 3.15. The components of the middle layer for Sample 1 and 3 were 50% ZrW_2O_8/50% ZrO_2 and 20% ZrW_2O_8/80% ZrO_2, respectively. The middle layer of Sample 3 seems to have a full reaction, with the diffused tungsten changing its color from white to yellow, while sample 1 did not. The reason for this phenomenon is the difference in the proportion of ZrO_2 powder.

Table 3.2. Numbers of FGM samples with different soaking time

Sample number	1	2	3	4	5
Soaking time (hr)	0	1	2	3	4

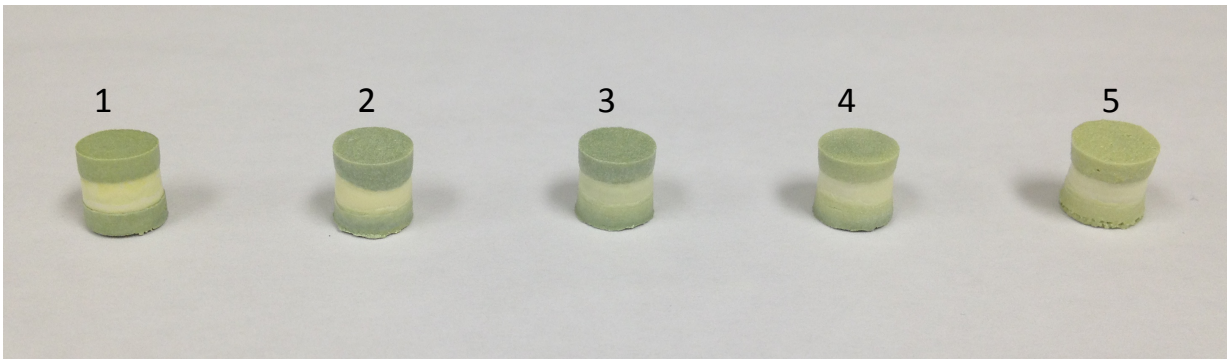

Figure 3.8. FGM samples sintered at 1160 degree with different soaking time.

In order to investigate the reaction mechanism within our FGM samples, various samples with different soaking time are shown in Figure 3.8. With soaking time

increasing, the sample color will change from dark green to light yellow gradually, which means the tungsten element will diffuse more with time since the green color comes the tungsten element.

Element mapping with SEM was carried out to examine the element diffusion inside the sample between each layer and the diffusion rate as a function of sintering temperature and soaking times was also calculated to comprehend the reaction process. Before doing the SEM, the sample was cut into half piece through thickness direction using diamond saw at a very low speed. The half side sample was used in the experiment to check the cross section. As shown in Figure 3.9, since the FGM sample was made symmetry from the mid-plane, the elemental mapping was done through the middle point. The percentage of W element was shown in Figure 3.9(a), which indicates W composition will first decrease at the boundary between two layers and then increase at the top layer. The same results can also be seen in SEM micrographs from different location.

The elemental mapping results for the samples with different soaking time (refer to table 3.2) were shown in Figure 3.10. The percentage of W element will decrease as the soaking time increase because of its own sublimation during sintering while Zr element will increase the proportion in the mixture due to the reduction of W element.

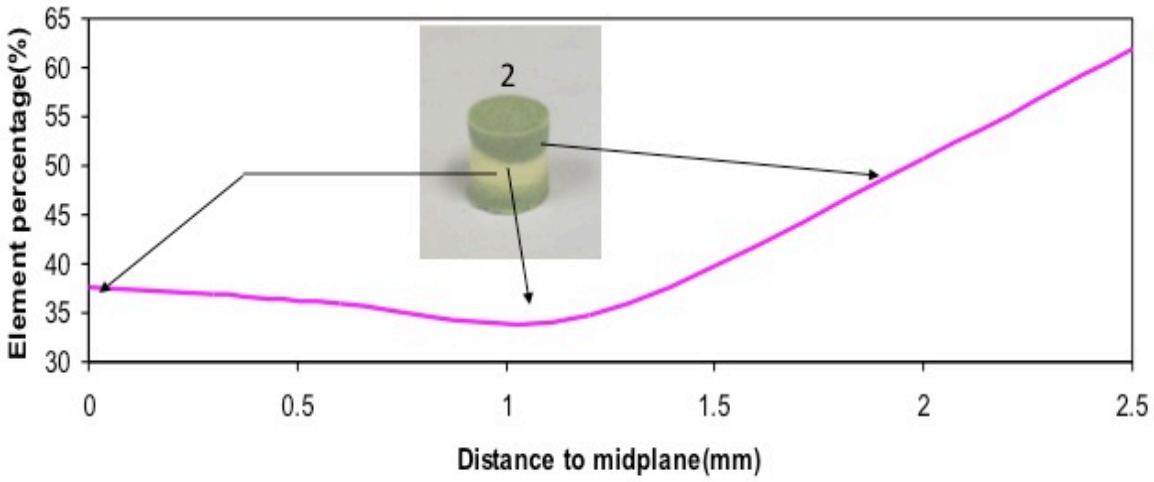

(a)

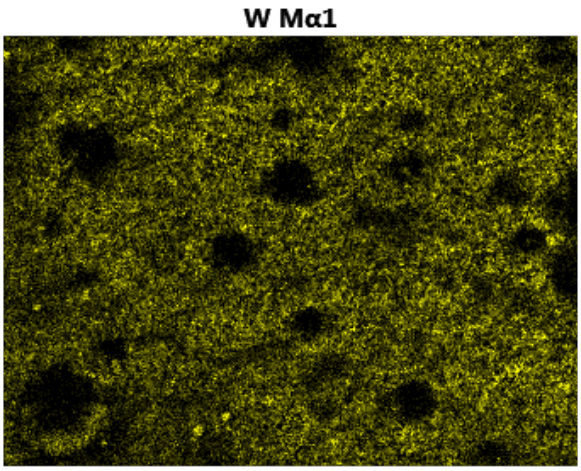

(b)

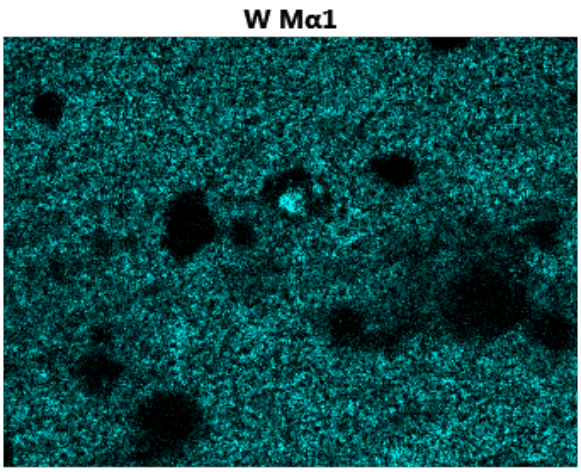

(c)

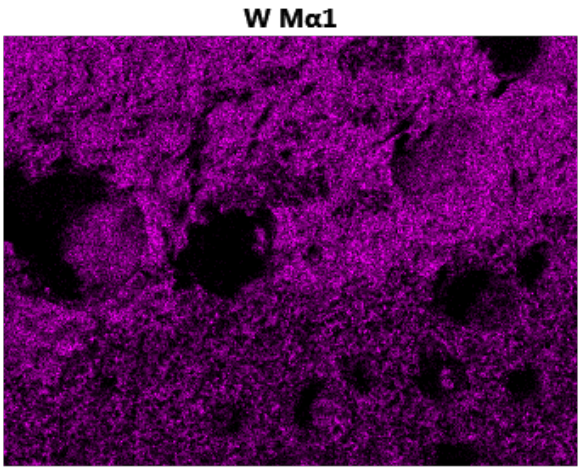

(d)

Figure 3.9 Elemental mapping of FGM sample: (a) W proportion in the FGM from

different location; (b) W element in position 1; (c) W element in position 2; (d) W element in position 3.

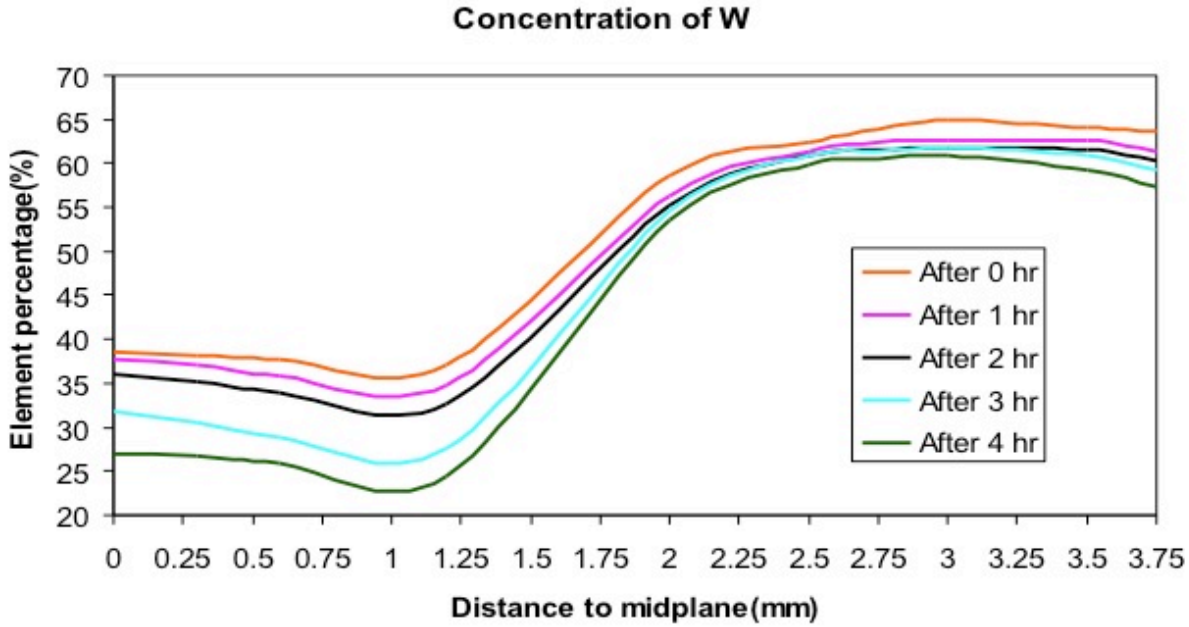

(a)

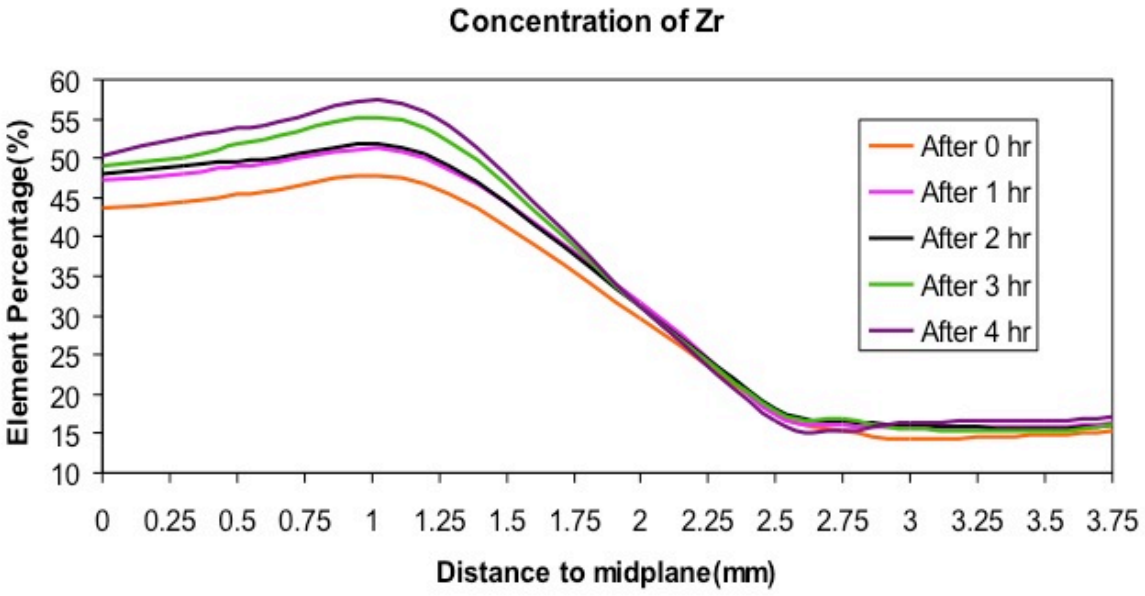

(b)

Figure 3.10. Elemental mapping results with different soaking time: (a) W, (b) Zr.

In addition to the three layers symmetry sample, asymmetry samples were also made for another applications. Figure 3.11 (a) showed the two layers sample, which was made of pure ZT on the top, 50% ZT+50% ZrO_2 for the bottom. The sample showed a very good appearance. After successfully making the FGM with the mixtures of ZT and ZrO_2, can the FGM with pure ZT to ZrO_2 was also fabricated by employing the MgO sintering additives as shown in Figure 3.11 (b). The symmetry sample was made with three layers, and the middle layer is pure ZT while the top and bottom layers were made of pure ZrO_2. The MgO additive will help consolidate the boundary between each layer after changing to liquid phase during the sintering. It will be much more effective to estimate the diffusion properties if we can have the FGM purely made from 100%ZT to 100% ZrO_2.

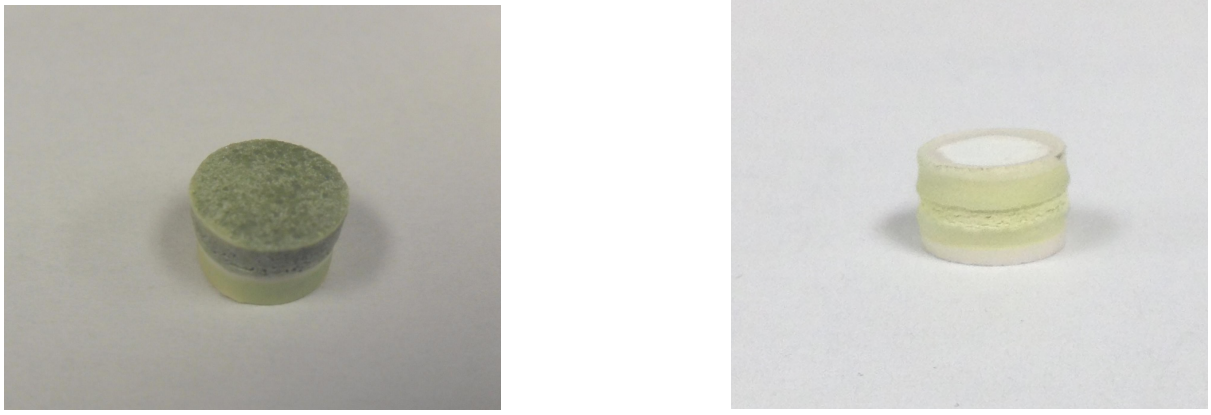

(a) (b)

Figure 3.11. FGM samples: (a) two layers sample (100%ZT and 50%ZT+50%ZrO_2), (b) three layers sample with pure ZrO_2 to ZT (100%ZO, 100%ZT and 100%ZrO_2), (c) cross section micrograph for sample b (edge), (d) cross section micrograph for sample b (center).

Figure 3.11 (cont'd)

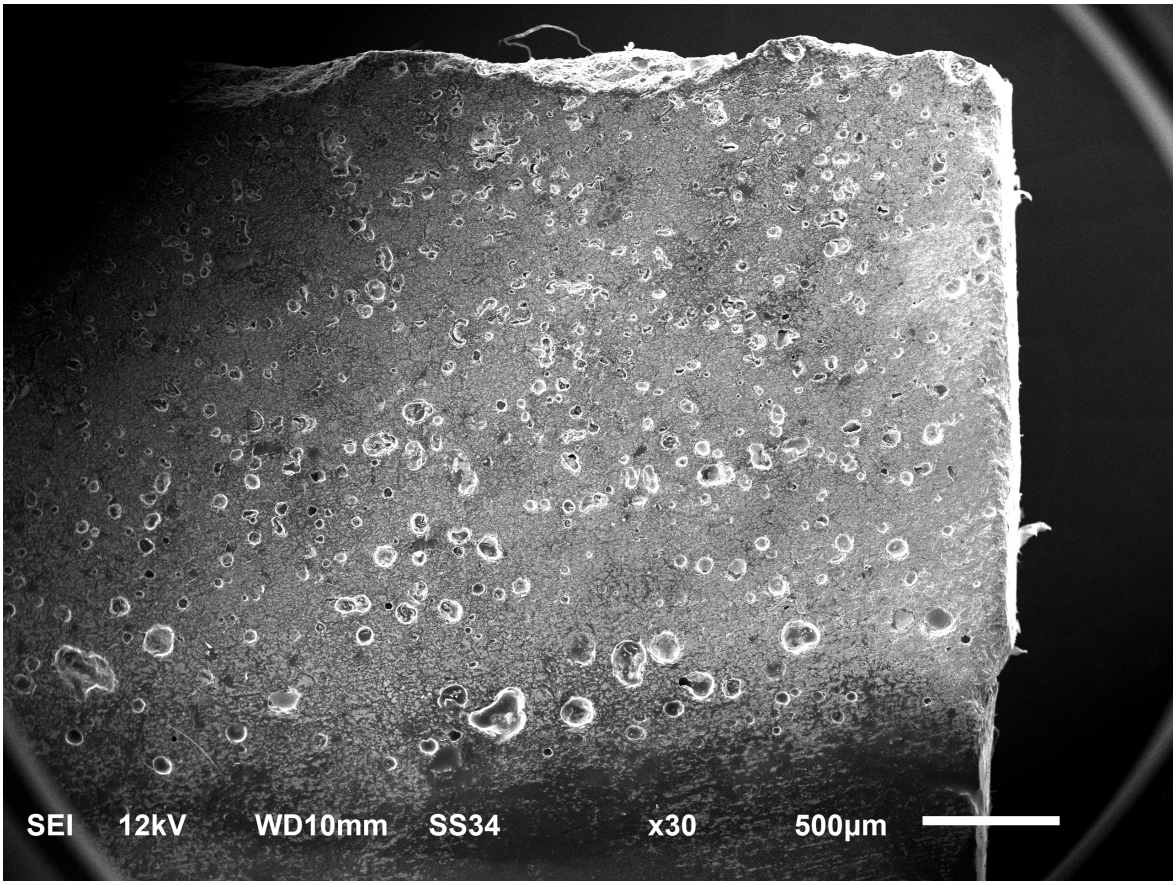

(c)

Figure 3.11(cont'd)

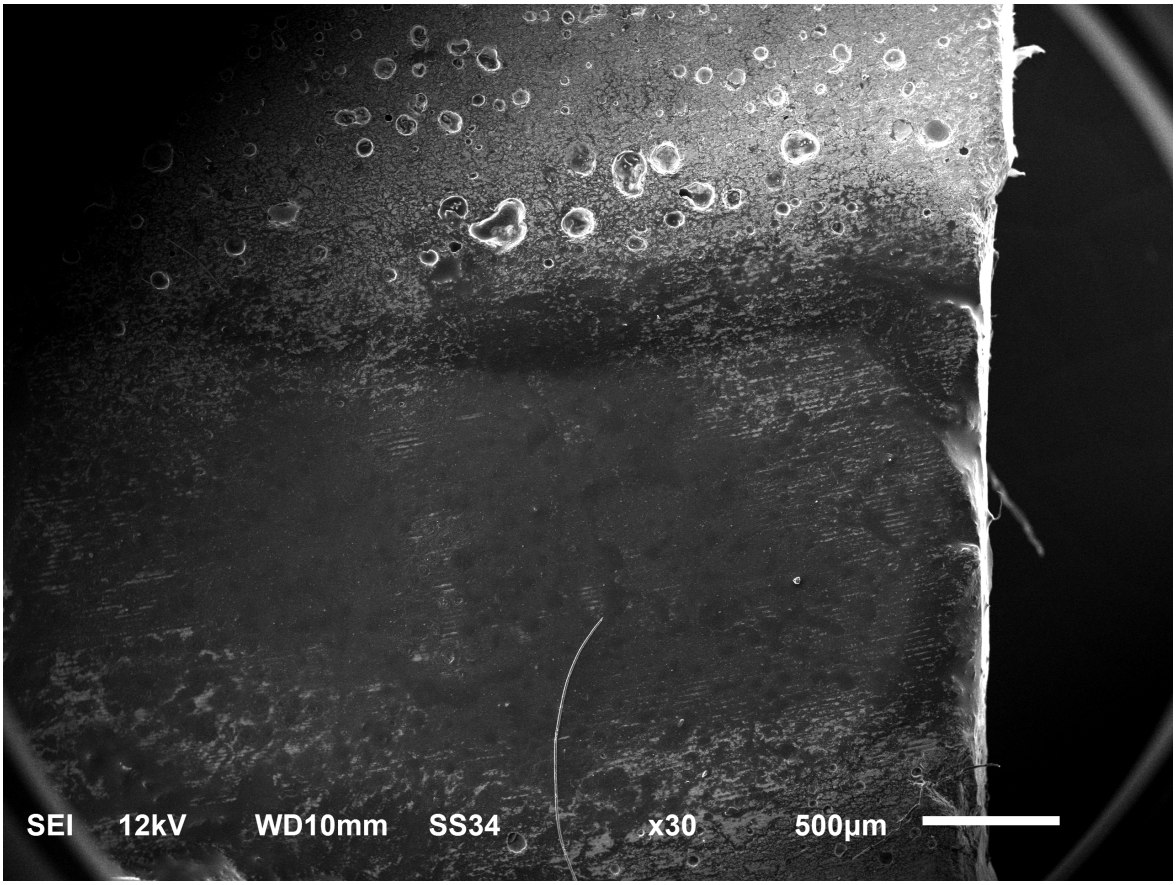

(d)

Thus, the micrographs and elemental mapping results were shown in Figure 3.11 and 3.12. As the sample was made symmetry, the measurement location starts from the middle plane. The elemental mapping results showed a very good continuous diffusion characters for both Zr and W. The theoretical percentage for each element in the compound was also calculated, for example, Zr 74.04% for ZrO_2 and Zr 15.54%, W 62.64% for ZrW_2O_8. The elemental mapping results showed a very good agreement with those theoretical values.

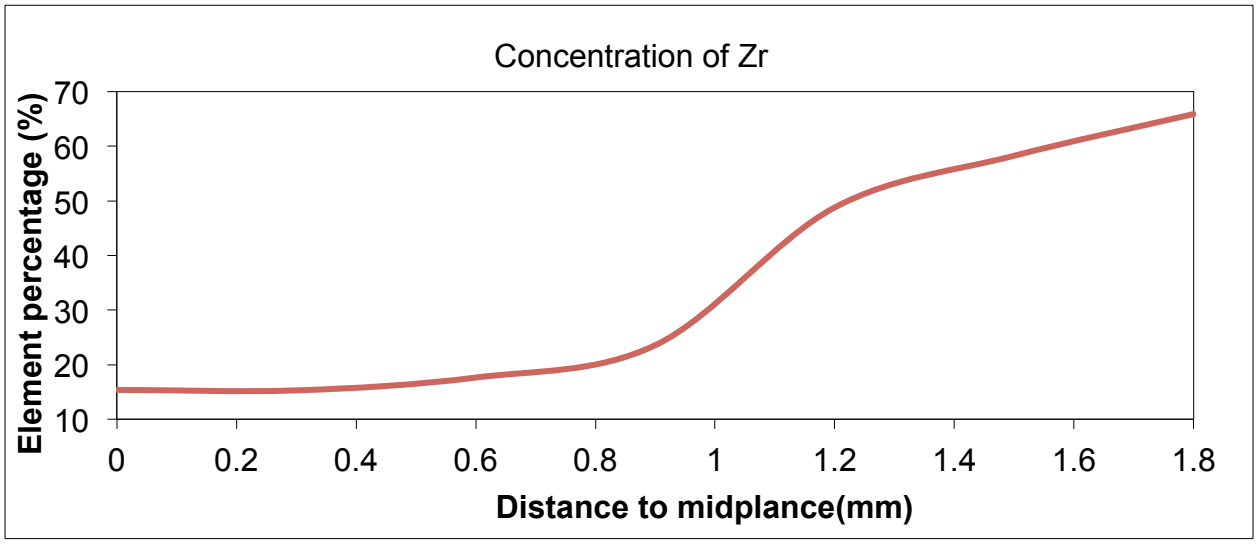

(a)

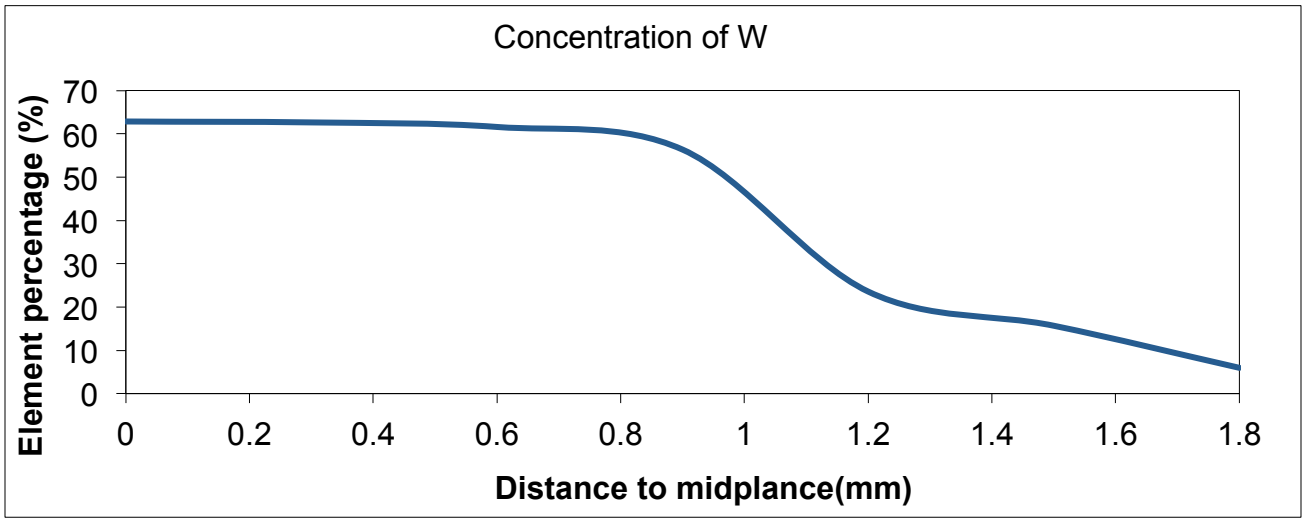

(b)

Figure 3.12. Elemental mapping results of FGM samples (refer to Figure 3.11 (b)), (a) concentration of Zr, (b) concentration of W, (c) micrographs of Zr element percentage on different locations.

Figure 3.12 (cont'd)

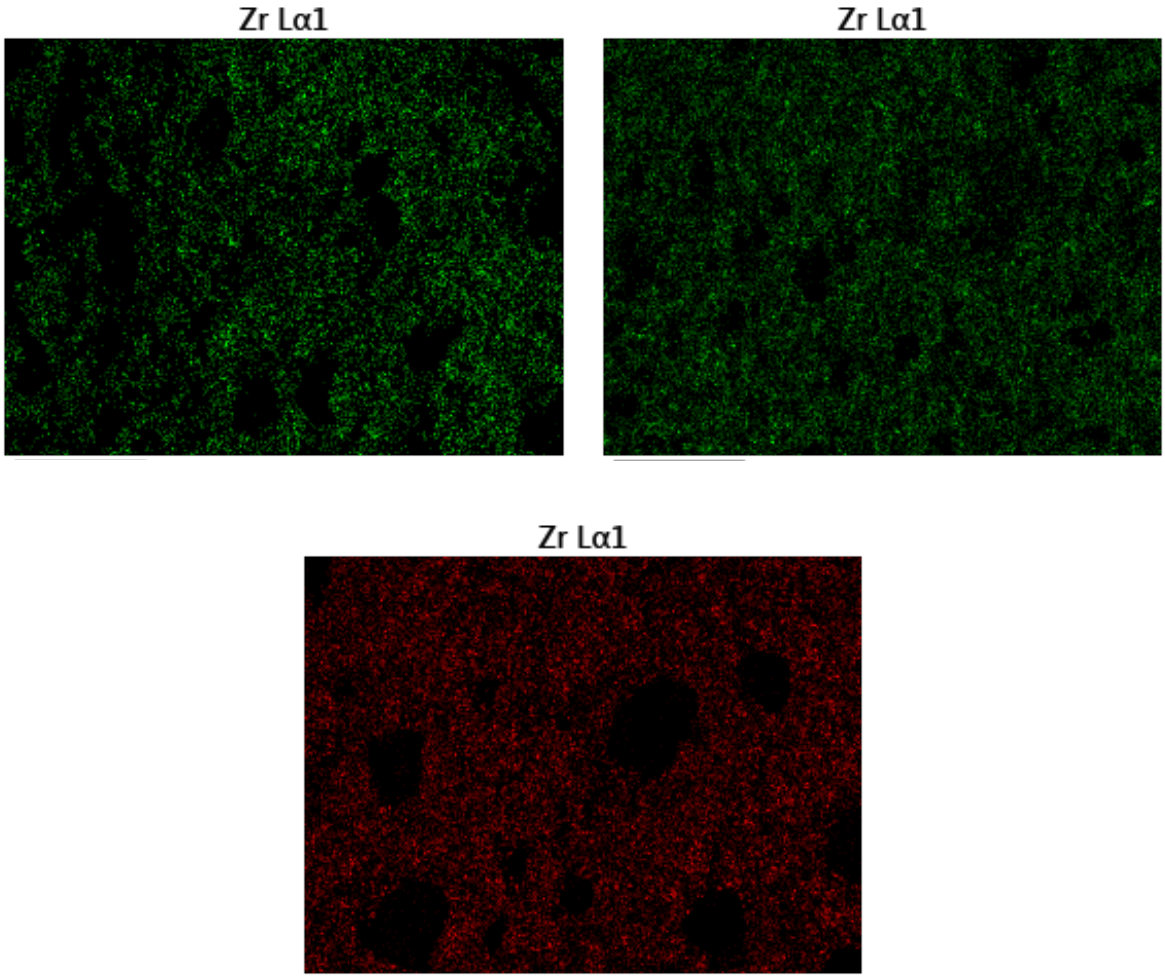

(c)

To measure the diffusion rate as a function of sintering temperature, the FGM samples were sintered at various temperatures between 1110 and 1210^{o}C for two hours separately. The reason for the small sintering temperature range is that the compound cannot fully react at low temperature while too high temperature will lead to liquid phase sintering. By measuring the diffusion depth, the average speed was calculated based on different sintering temperature. As shown in Figure 3.13, the diffusion rate had a close

linear relationship with temperature, which is consistent with other reference [93] that the diffusion rate of W will increase as the temperature going up. The average speed of W diffusion is 0.45mm/s during the sintering, which was used to calculate the sintering time and design the FGM with certain property.

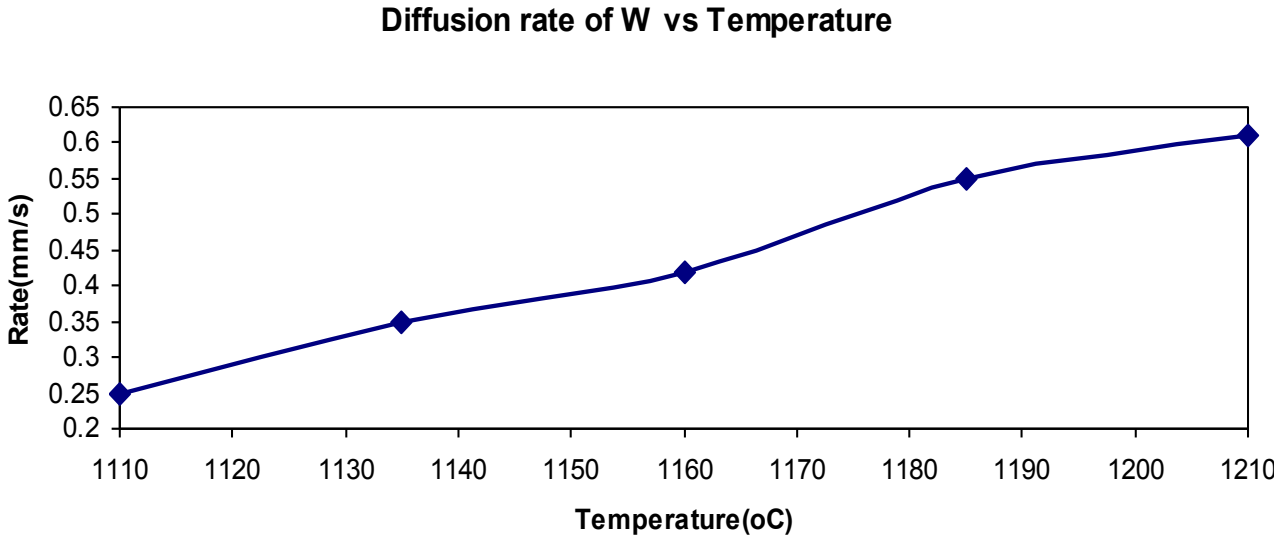

Figure 3.13. Diffusion rate of W element based on different soaking temperature

With the diffusion rate as a function of temperatures, the diffusion rate related with different soaking time will also be considered to establish the reaction model. According to the measured diffusion depth and elemental mapping results, the diffusion rate as a function of soaking time was shown in Figure 3.14. The rate has the maximum value at one-hour soaking time and the highest value is near 0.45mm/s. The two important affecting factors for diffusion are temperature and concentration difference. Figure 3.13 showed that the diffusion rate of tungsten has a linear relationship with temperature. And with the concentration of tungsten decreasing, the diffusion rate also decreases with the increase in the soaking time.

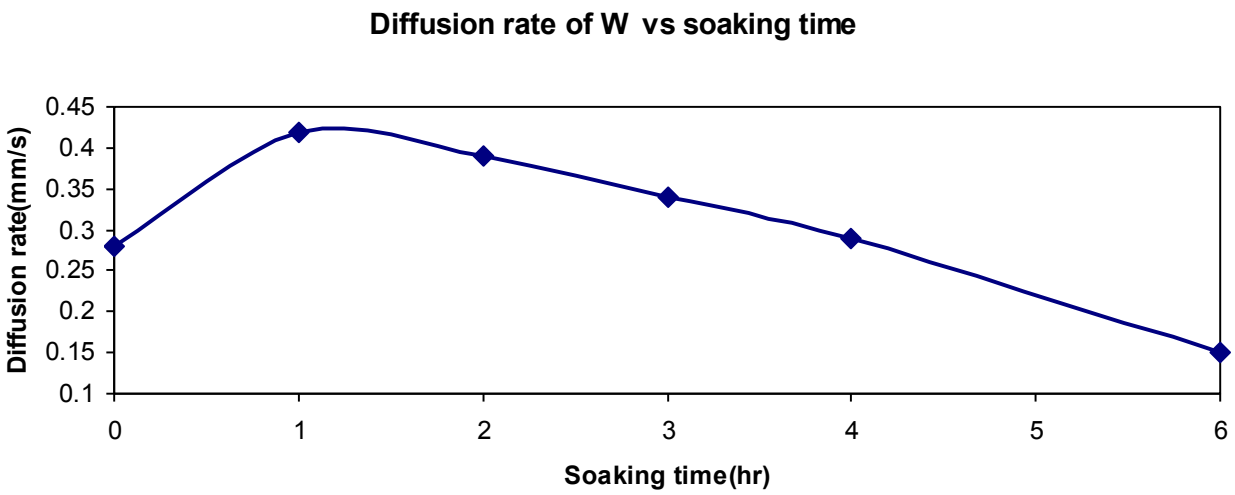

Figure 3.14. Diffusion rate of W element based on soaking time

3.3.3 Distortion control of sintered sample

In the first attempt to produce a continuous FGM, only CERAC-2003 powder was used as the zirconia component of the WO_3+ZrO_2 powder mixture. After sintering, the original cylindrical shape of the green bodies had changed to a shape similar to the hourglass shape of a cone for the left and center samples in Figure 3.6. This distortion comes from a mismatch in the final dimension between the two materials after compaction and sintering. The compaction and sintering behaviors of powders can be modified by mixing two or more powders with distinct characteristics such as average size and size distribution, which ultimately influences the final dimension of a sample [68].

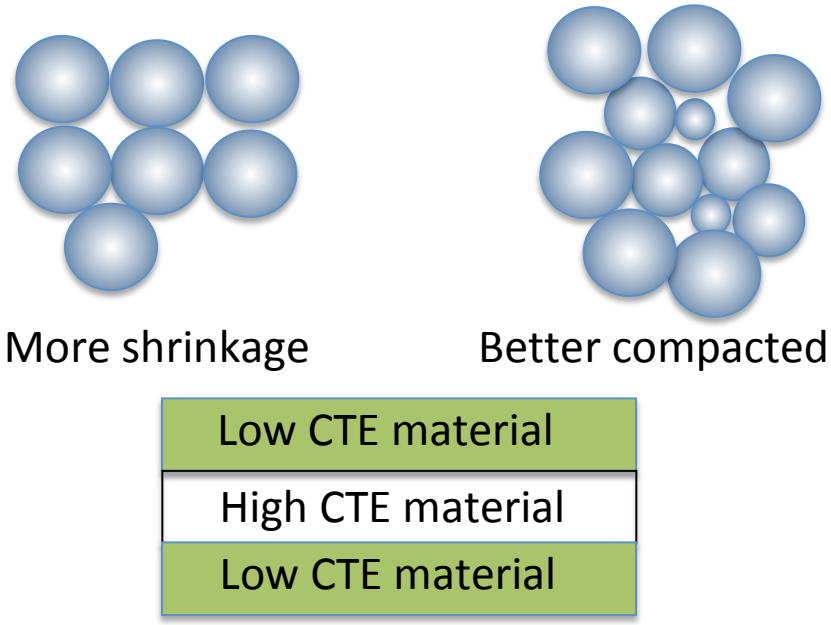

Figure 3.15. Powder mixing effect with different particle size

Based on this finding (shown in Figure 3.15), TZ3YS powders (smaller particles) were mixed with different proportions of CERAC-2003 to form zirconia powder mixtures. The final diameter of each sample was different as the proportion of CERAC-2003 in zirconia powder mixtures was varied. The powder mixing process allows the smaller TZ3YS particles to fill the interstitial spaces among the larger CERAC-2003 particles, producing a powder mixture with better compaction than either TZ3YS only or CERAC-2003 only. The powder mixture with a better compactabilty will have a small shrinkage during sintering. Therefore, if the mixture can be compacted at a higher density, the final sintered diameter for the middle layer will increase to the dimension of the other layers and the distortion will be minimized.

(1) (2) (3)

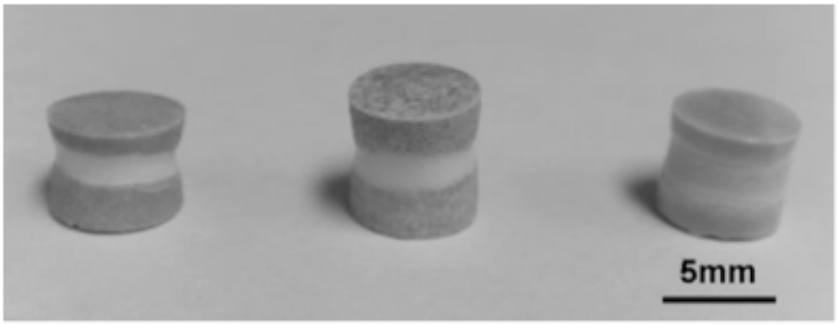

Figure 3.16. Distortion controlled samples with powder mixing to change the sintering behavior

Several attempts were made to achieve the appropriate proportion between TZ3YS and CERAC-2003 to obtain the same final sintering diameter with ZrW_2O_8. The sintering diameter has a maximum value when the components are approximately 50% of TZ3YS to 50% of CERAC-2003. As shown with Sample 3 in Figure 3.16, the middle layer mixed with 20% ZrW_2O_8 and 80% ZrO_2 (20% CERAC, 80% TY3ZS) reduces the distortion effectively.

Although the powder mixture found for the middle layer can reduce the distortion, the gap shown in Figure 3.6(a) finally destroyed the sample due to the low shrinkage of the outer cylinder. After many attempts, the sample shown in Figure 3.6(b) was produced without a gap by increasing the proportion of ZrO_2 powder. Therefore, a good sample can be obtained by applying a different proportion of ZrO_2 powder to the middle layer of the outer cylinder (20% ZrW_2O_8/80% ZrO_2, and 20% CERAC/80% TY3ZS) and the core

part made of 50% ZrW_2O_8/50% ZrO_2, where ZrO_2 was produced by mixing with 10% CERAC and 90% TY3ZS. Two reasons contribute to this phenomenon.

The first reason is that the proportion of ZrO_2 powder affects the shrinkage of the core part during sintering. The more ZrO_2 powder the core part has, the more shrinkage the sample can attain after sintering. The other reason is that the diffusion of tungsten through the thickness direction can influence the final sample dimension. Figure 3.7 shows that the outer cylinder has a much thinner (t=2mm) ZrO_2 layer compared to the ZrO_2 core (d=8mm). The tungsten can diffuse into the outer cylinder very easily, causing it to expand much more evenly with the same proportion of zirconia powder. The composition (20% ZrW_2O_8 and 80% ZrO_2) of the outer cylinder can prevent distortion effectively, which means the layer experiences the same amount of shrinkage as the pure ZrW_2O_8 layer after sintering. While using this composition as a core part, a gap, due to different shrinkage, was generated as shown in Figure 3.6(a). That is mainly because the reaction depth of ZrO_2 with diffused tungsten can affect the ultimate sample size.

3.4. CONCLUSION

This section introduces the use of advanced materials created by shrink-fitting partially

sintered ceramic samples made to form complex FGMs. When these tiles are assembled, they exert compressive force to induce a buckling action among the tiles upon thermal loading. These tiles will seamlessly fit together and will expand or shrink, exerting forces on other tiles to cause buckling when heated. The FEM simulation using ABAQUS verified that the model buckled using the proper material parameters under the expected loading condition. Using the shrink-fitting technique, we were able to successfully produce several samples. Mainly ZrW_2O_8 and ZrO_2 tiles with a designed shape were partially sintered and machined, and with a dimensional compensation, the perspirable skin assembly was fabricated. To enhance the buckling action, a complex FGM tile was fabricated to optimize the contact situation of the core and tile part in the designed simulation. It was found that each layer was joined with other layers through a reaction to fabricate the FGM tiles with good shape control and mechanical integrity.

CHAPTER 4 IMPROVING DENSITIFICATION OF ZIRCONIUM TUNGSTATE WITH NANO TUNGSTEN TRIOXIDE AND ADDITIVES

4.1. INTRODUCTION

Because of the highly negative thermal expansion coefficient, zirconium tungstate (ZT) offers a unique opportunity in engineering applications. However, processing of ZT has not been fully perfected to yield a near thoeretical density. Thus, ZT has relatively a weak strength, which prevented its unique property to be fully utilized in applications. This part investigates the processing methods to improve the packing and subsequent final densities – thus improving the mechanical strength. These methods include (1) use of a wide variety of powders with different size, (2) use of nano-powders and (3) use of additives. Under the same compaction and sintering condition, a variety of powder mixtures were produced, whose initial packing density and final sintered density were measured and compared in order to determine the optimal combination. The optimal amount of nanopowders and sintering aids were determined to improve the final density and strength.

Powder Metallurgy (P/M) is the main processing method used to process most ceramic and some metallic components. The three steps of P/M mentioned above are closely related to each other, that is, one step can affect another. The average size of the

particle, the size distribution and the shape of the particle influence the compatibility and sinterability [69-73]. Moreover, other factors such as compacting pressure, friction, sintering temperature and sintering aids can alter the final density and appearance of a sintered sample [74-76].

Nanoparticles are typically sized between 1 and 100 nanometers [77]. Although numerous methods of producing nanopowders has been discovered, bulk ceramics cannot be processed directly from the nanopowders due to the tremendous friction among the powders due to the extremely large surfaces in contact, resulting in limited densifications in the final product [78]. However, if the nanopowders are mixed with coarse particles, both compaction and sintering can be improved [79, 80] to enhance the final density. Another method of improving the final density is to use the sintering aids. The sintering aids help to control the microstructure of sintered materials, which can be classified by two categories: 1) the reaction with the basic compound to produce a liquid phase, 2) the solid state sintering without the formation of a liquid phase [81].

(a)

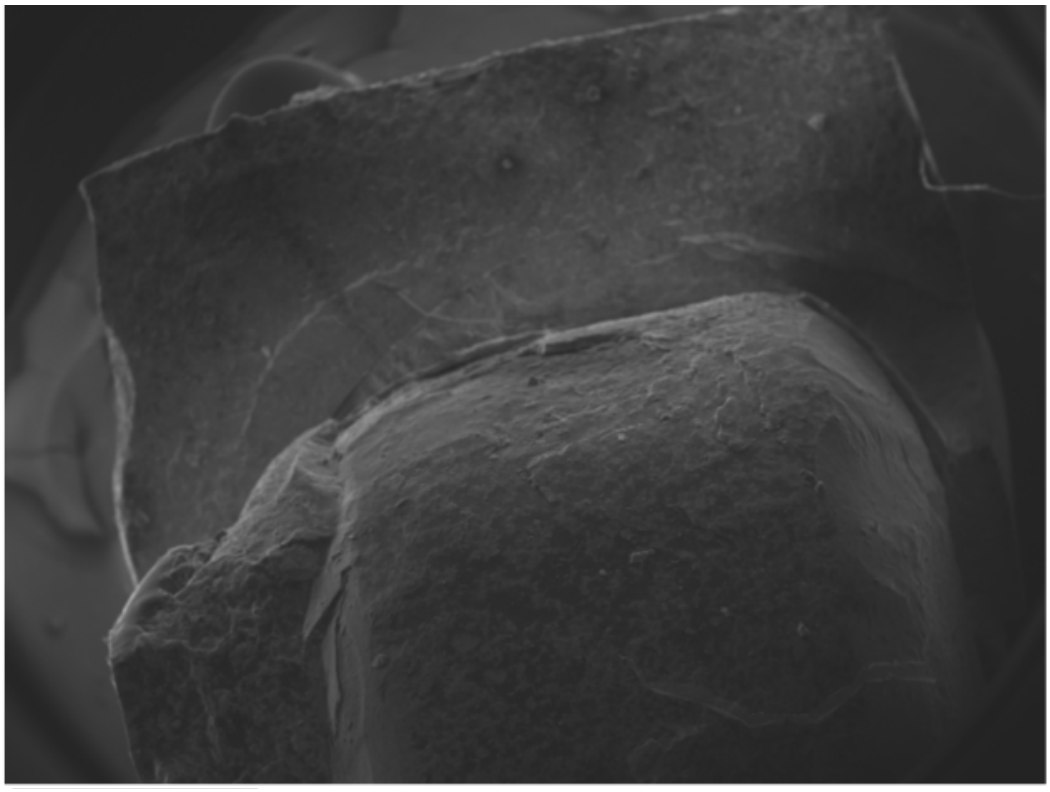

(b)

Figure 4.1 Shrink-fitted sample cracks due to the low strength of outside ZT: (a) Broken sample, (b) SEM micrograph showed ZrO_2 hard-core.

Zirconium tungstate (ZrW_2O_8 or ZT) is an essential material in the design of 'Perspirable skin,' which is a new design of thermal protection system with possible applications for reentry or supersonic vehicle. The initial design consisted of a material with distinctly negative coefficient of thermal expansion shrink-fitted into a skin. The main idea hinges on the core made of either pure ZrW_2O_8 or Functionally Graded Materials (FGMs) made of ZrW_2O_8 and ZrO_2. ZrW_2O_8 or ZT is the material with exceptionally large and isotropic negative thermal expansion (NTE) coefficient in a large range of temperature (0.5 K–1050 K) with a phase transition of α - ZrW_2O_8 into β - ZrW_2O_8 at about 420 K [61].

Despite of its advantage, zirconium tungstate contains abundant residual pores with conventional processing method, which certainly decreases the strength of material. Especially when we combine ZrW_2O_8 with high strength ZrO_2 sample to make FGM, it would be very easy to generate crack in ZT. The Figure 4.1 showed the crack happened during the shrink-fitting process. Therefore, in order to successfully make the FGM sample, it is necessary to enhance the strength of ZT to accommodate with ZrO_2.

In this study, the packing and sintered densities of ZrW_2O_8 with nanopowders and some sintering aids were investigated. Through this study, the optimal processing receipt was attained the highest density in order to improve the strength. The Young's modulus of each sample, which is also related to the pore content, was also measured.

4.2 MATERIALS AND EXPERIMENTAL PROCEDURE

A series of experiments was conducted with five distinct powders whose average particle sizes vary from nano to micro. The size and material of the powders are summarized in Table 4.1. The powder list consists of two tungstate powders, one zirconia and two sintering aids alumina and magnesia. ZT was successfully produced by the react of WO_3 and ZrO_2 powders. Due to the detrimental phase change in zirconia (ZrO_2), either partially or fully stabilized powders are used. In this experiment, partially stabilized zirconia powder manufactured by CERAC was used.

Table 4.1. Characteristics of Raw Powders used in this study

Name	Material	Mean particle size (μm)	Manufacturer
W-Fluka	WO_3	8.22	Sigma-Aldrich, U.S.A.
Nano Powder	WO_3	~0.06	Inframat Advanced, USA
CERAC-2003*	ZrO_2	1.23	CERAC Inc., U.S.A.
TMDAR	Al_2O_3	0.17	3M company
MAGCHEM 10 -325	MgO	0.25	MARTIN MARIETTA

*Stabilized by 3w% Y_2O_3.

A 2:1 stoichiometric ratio of WO_3 and ZrO_2 was needed to produce pure ZrW_2O_8 [58].

Different weight ratios of nano WO_3 powder and sintering aids were added into the mixtures. The powders were mixed with the speed mixer DAC 150 (FlackTek, Inc., USA) for 3 minutes (1min for each cycle and totally 3 cycles) at the angular velocity of 2000 rad/s. Sometimes, in order to increase the compatibility of green sample, several different zirconia beads were cooperated with speed mixer to break down the particle size of certain powders. Therefore, the green compatibility can be improved using powder-mixing effects then. Figure 4.2 showed that the zirconia beads used in our experiment, and it was much more effective to use the beads with smaller diameter. Four grams of each powder mixture were measured with Adventurer AR 2140 (Ohaus Corp. USA) with a 0.0001g resolution. Before pouring the powders into the die, the die wall was lubricated with graphite powder (Panef Corp., USA). The mixture was then stacked in a single-action die whose inner diameter, Din, is 19.10mm.

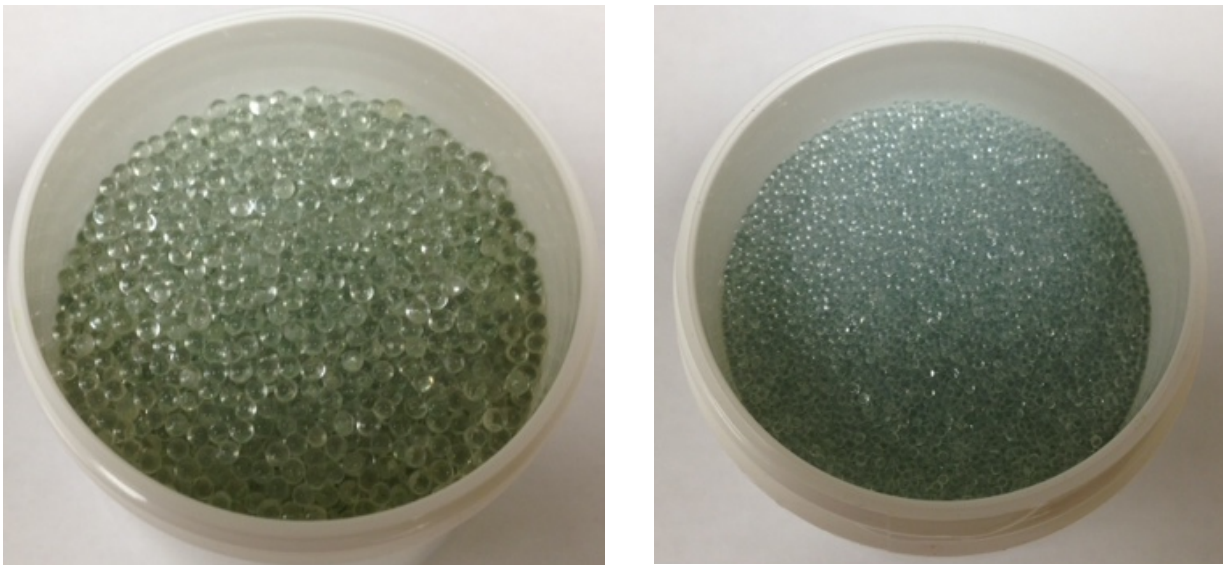

(a) (b)

Figure 4.2. Zirconia beads used in the experiment to break down particle size for the speed mixer: (a) D=2.5mm, (b) D=1mm.

The compaction experiments were implemented by MTS Insight 300 (MTS Systems Corp., USA). The speed was 5mm/min and the stress resolution is 0.013MPa. During the compaction, only the top punch moved. At first, a pre-load of 0.5MPa was applied to set an initial state so that the compact characteristics can be measured accurately before starting the main compacting process. After pre-loading, the initial height of each sample, h_i, was measured by subtracting the height of the two punches from the total height of the two punches and the pre-loaded compact thickness. A Marathon electronic digital caliper with a 0.01mm resolution was applied to measure the distance.

The powder mixture is composed by two distinct powders, WO_3 and ZrO_2; therefore, the

density of the mixture with the 2:1 stoichiometric ratio [10] was obtained

$$\rho_f = v_{wo3}\rho_{wo3} + v_{zro2}\rho_{zro2} \tag{4.1}$$

to be 6.79 g/cm^3 with the density of WO_3, is 7.16g/cm^3 and the density of ZrO_2 is 5.68g/cm^3. Considering the diameter of each compact to be the same as the inner diameter of the die, D_{in}, the relative density of a green compact, R_i, can be calculated by the following equation:

$$R_i = \frac{\rho_i}{\rho_f} = \frac{m}{\rho_f V_i} = \frac{4m}{6.79\pi {D_{in}}^2 h_i} \tag{4.2a}$$

where m, *V*, and ρ represent mass, volume, and density, respectively, and the subscripts i and f represent initial and theoretical value. The equation 4.2(a) was used to calculate the initial compaction relative density.

By the recorded top punch displacement, Zt, and the initial compact height, hi, or final compact height, hf, the sample height at time t, ht, can be calculate,

$$\begin{cases} ht = hi - Zt & (4.2b) \\ ht = hf + Zt & (4.2c) \end{cases}$$

The ht calculated by Equation (4.2b) or (4.2c) for any compact was the same.

From the calculated ht, similar to calculating the initial relative density, the relative density at time t, defined as Rt, can be found as,

$$Rt = \frac{\rho t}{\rho f} = \frac{m/Vt}{\rho f} = \frac{m}{\frac{6.79}{4}\pi Din^2 ht} \qquad (4.2d)$$

In Equation (4.2d), the sample diameter was assumed to be matching the inner diameter of the die, D_{in}.

The powders were compacted from 0.5MPa to 120MPa until the relative density do not further increase. After compaction, the final green samples had a diameter of 19.10mm and their heights ranged from 3.1mm to 3.9mm. Therefore, the height/diameter ratios of compacts (0.15-0.2) were very low, which indicated the transmit force applied on the top and bottom punches were almost identical in the compaction without any frictional loss and a uniform density throughout each sample can be attained.

The green compacts are then sintered at 1160°C for 6 hours in a covered platinum crucible under atmospheric pressure in a furnace (Carbolite-HTF1700, UK). The covered crucible provided the nearly sealed environment required to reduce the sublimation of WO_3 at temperatures higher than 800°C. Since decomposition of ZrW_2O_8 takes place at temperature between 1050°C and 1100°C, an air quenching process, performed by removing the crucible from the sintering furnace, was necessary to prevent decomposition at lower temperatures and produce pure ZrW_2O_8. The final sintered samples were coated with toluene lacquer and their volumes were measured in water by Archimedes' method.

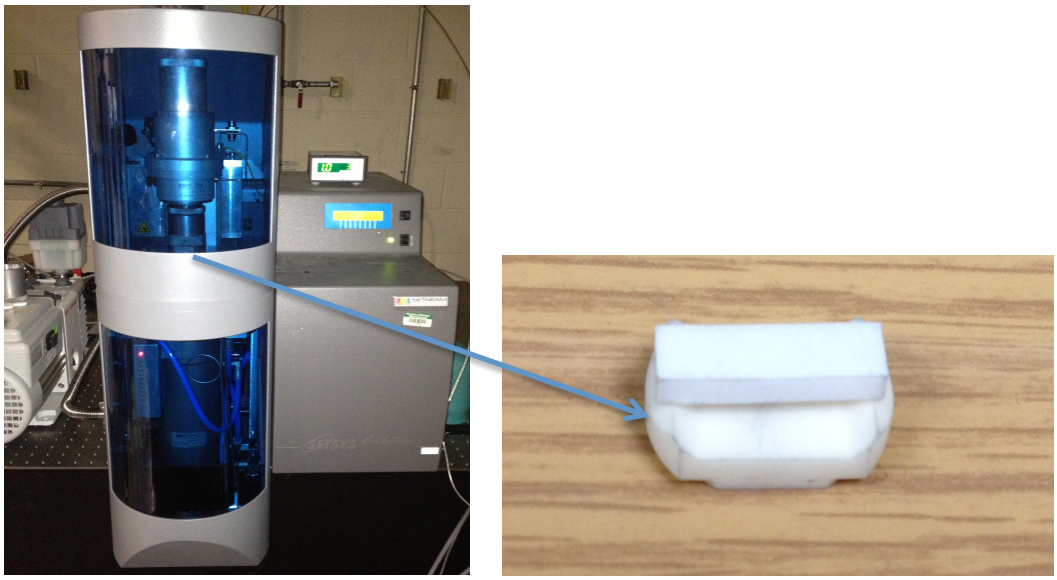

(a) (b)

Figure 4.3. TMA (thermal-mechanical analyzer) (a) TMA furnace (b) base support for measuring Young's modulus.

To understand the effect of adding nano-sized WO_3 on densification, a sample without nano-sized WO_3 was also prepared. In addition, to investigate the effect of sintering aids on densification, several samples without any sintering aid and the same sample with each sintering aid were prepared. These samples were all processed with the exactly same procedure. After obtaining the final density of sintered sample, the Young's modulus of each sample was also tested to confirm the improvement in densification. Before the Young's modulus testing, the samples were heat treated (3°C/min for both heating and cooling cycles, and soaking for 60 minutes at 300°C) to cure microcracks induced by the quenching process [82].

The Young's moduli of sintered samples were measured using a Thermomechanical Analyzer (TMA: Setaram 95, France). Three specimens produced for each sample were tested for Young's modulus. A load of 0.2N was applied to the sample until the displacement is stable. After that, another 1N load was applied, and the flexure was recorded to calculate Young's modulus. During the testing, the Young's modulus variation is within 8% in all three specimens. Thus, the results were consistent and the average value of three specimens was reported in this report.

4.3 RESULTS AND DISCUSSION

4.3.1 Relative packing density of mixtures with different composition

The same procedure to calculate the initial relative density was use to calculate the relative density at time t, defined as R_t. According to Eq. (4.2), only h_i was replaced by h_t in order to calculate R_t. while h_t was the sample height at time t, which can be calculated by subtracting the distance of two punches without sample from the distance with a sample. The compacting stress is the applied load F_t divided by the punch area.

The relative density-stress curves for each powder mixture group were shown in Fig. 4.4. As the load increases, each powder mixture compacts to higher densities up to about 120MPa and beyond 120MPa the powder did not further compact. While the

stoichiometric ratio is kept constant at 2:1, the proportions of nano-sized WO_3 powder as part of WO_3 were increased to improve the sinterability. As shown in Fig. 4.4, the 79% Fluka + 21% CERAC mixture showed the highest green density (64%) and five weight percentages from 0 to 100% of the Fluka powder was replaced with nano-sized WO_3 powder. The packing density values were calculated using Eq. (4.2), and. The packing density decreased once the nano-sized WO_3 powder was added into the mixture as evident in Figure. 4.4.

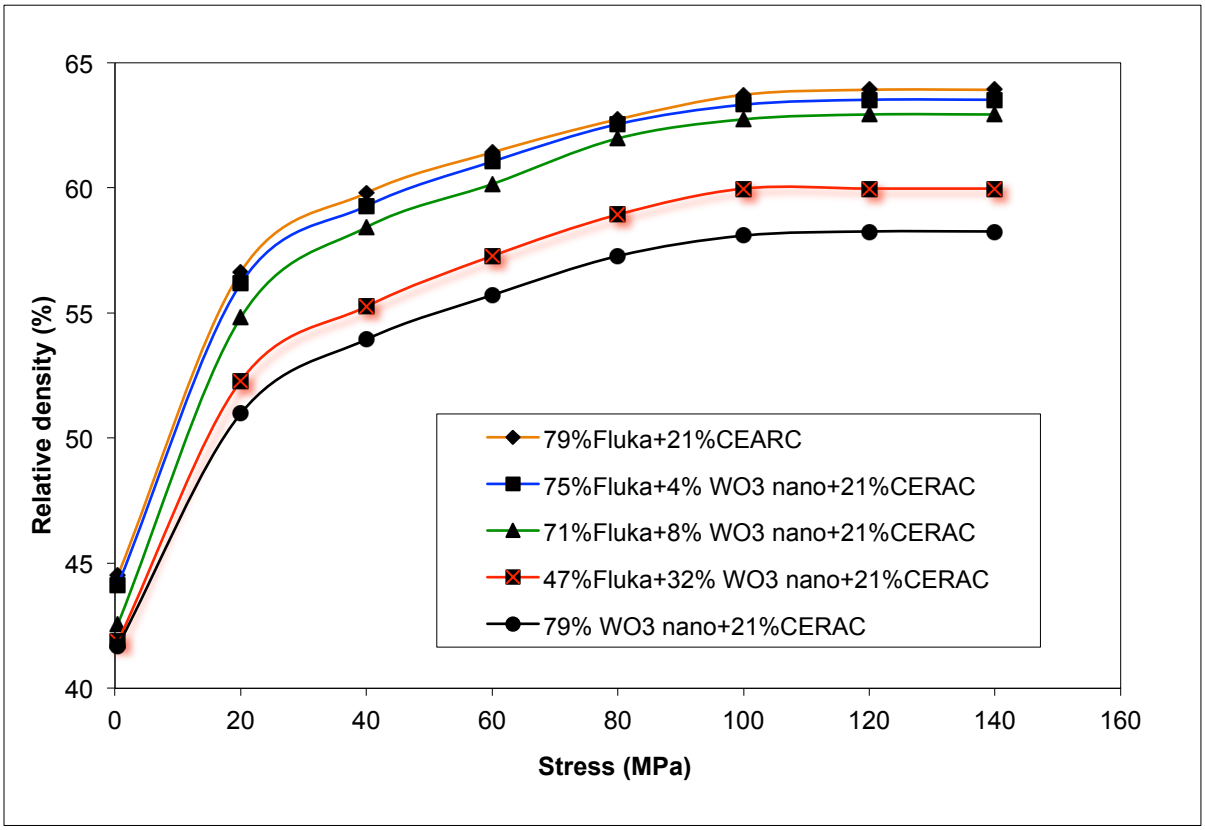

Figure 4.4. The relative density-stress curves after compaction with different nano-sized WO_3 powder proportions.

It was known that pressing nanopowders is a much more difficult task than pressing the powders with larger particle sizes [83, 84]. Because of their interactions among individual particles and die wall during compaction, nanopowders always show poor compaction. However, numerous studies [69, 85, 86] showed that if smaller particles can fill into the interstices among coarse particles, then the powder mixture should be compacted better. For a continuous size distribution system, the average particles size of coarse powder is at least 3.6 times of fine powder without changing the total volume of mixture [87]. In our experiments, the stoichiometric ratio between WO_3 and ZrO_2 was fixed in order to achieve a fully reacted compound. From Table 4.1, the average particle size of Fluka was much bigger than that of CERAC (6.7 times), which indicated ZrO_2 powders already filled into the interstices of coarse particles to improve the packing density. Therefore, in our experiment, the small amount of the nano WO_3 powders slightly decreased the packing density due to its low pressing ability.

The zirconia beads mentioned above were also tried to mill the powders in order to break down the particle size. The smaller WO_3 particles were mixed with ZO powders after grinding to check the green compact density. During the milling process, a good starting point is 5g material and 10g of beads in a Max 20 Cup. Listen to the mixing and adjust the speed so that the sound of beads colliding is the loudest. In our experiment, the optimum speed was around 3000RPM. The milling process needed to be stopped every 30 seconds to make sure the sample does not get too hot due to the friction. Two

different sizes (2.5mm and 1mm) of beads were tried in this experiment, and the green compact density was shown in Figure 4.5. From the Figure, we found that the compact density was improved a little after the milling. The mixture with smaller beads for milling 2 minutes had almost the same density value with larger beads for 10 minutes. While after 10 minutes, there will be no improving effect to the compatibility of green sample. Therefore, it was a good attempt to enhance the green compact density by employing the milling media during the mixing process.

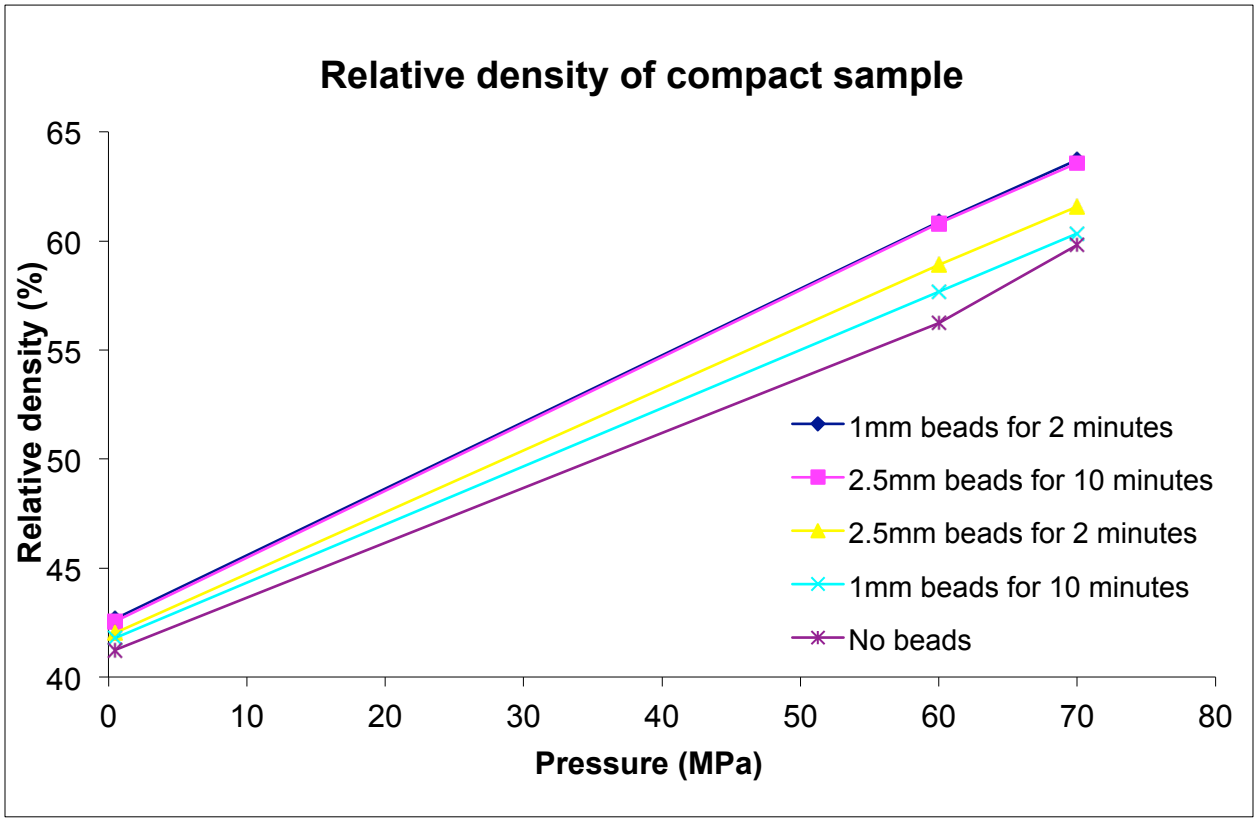

Figure 4.5. Compaction properties of powders with different milling media size.

4.3.2 Relative sintered density of mixtures with different composition

The relative densities of all mixtures sintered with nano-sized powder and 0.4wt% sintering aids were shown in Table 4.2. Since only small amount of sintering aid were introduced into the mixture, the change in the theoretical density can be neglected. The mixture (75w% Fluka + 4w% nanoWO_3 powder + 21w% CERAC) with 0.4wt%MgO additive showed the highest sintered density (95.9%). In contrast, the relative density of 79w% nano WO_3 powder +21w%CERAC mixture was lowest (71.9%). The addition of 0.4wt% MgO additive enhanced the relative density of ZrW_2O_8 from 91.5% to 95.9%. The addition of 4wt% nanopowders improved the densification of ZrW_2O_8 from 86.8% to 91.5%. The beneficial effect of 4wt% nano WO_3 powder in the densification can be explained in terms of the enhanced driving force for densification due to the high surface area of nanopowders. The nanopowders enhance sintering but reduce the compaction densities [78, 88, 89]. Therefore, as long as the packing density does not get significantly affected, the nanopowder will certainly improve the densification process and increase the final density.

Since the nanopowders have a positive effect on the final sintered density, the question is how many percentage of nanopowder in the mixture will lead to the highest density for our sample. Several experiments were carried out to find an ideal amount of nanopowder and the results were presented in Figure 4.6. The highest density achieved is the mixture

with 4~5wt% nanopowder which is the best final sintered density. As the proportion of nanopowder increase, the enhancement in the densification cannot compensate the poor compactability, which leads to the same sintered density of two mixtures (0% and 32% nanopowders). Therefore, if nanopowders exceed the threshold of 32%, the final density is sacrified as the sample #e in Table 4.2.

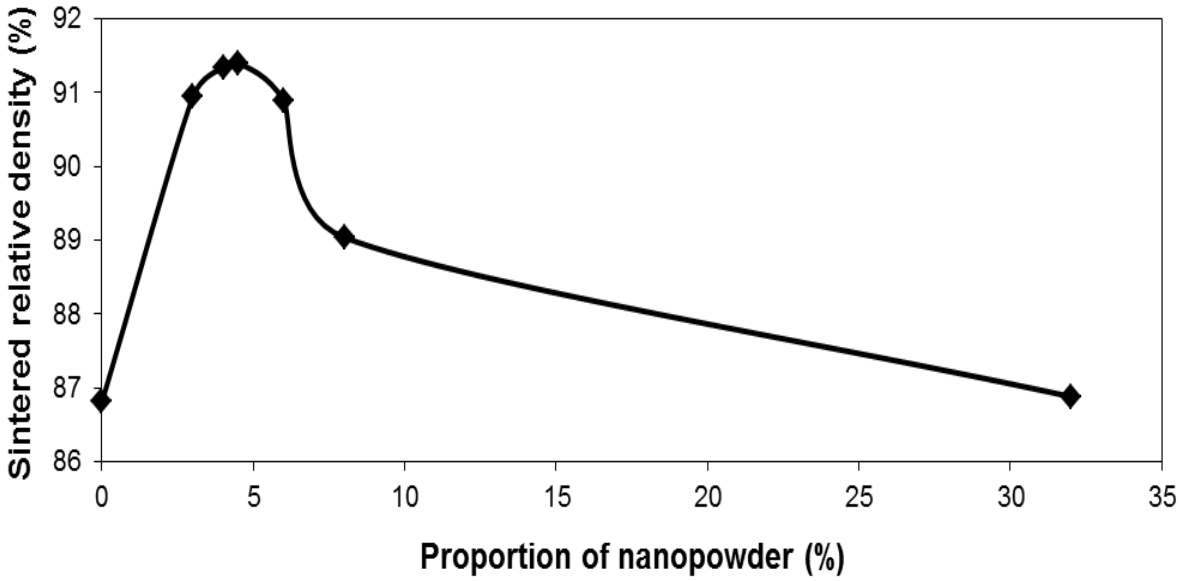

Figure 4.6. The sintered relative density with different proportions of nanopowder.

The cross-section micrographs of each sample in Table 4.2 were also taken and shown in Figure 4.7. With same magnification, the 4% nanopowder sample showed better appearance among the first five Figures with fewer and smaller pores. The 79% nanopowder exhibited very poor appearance as indicated, which was consistent with the data in Table 4.2. Figure 4.7(a) and (d) were very similar in the size and concentration of pores, which agreed with the values of sample #a and #d in Table 4.2 as they were close in the final density. Figure 4.7(f), (g) and (h) showed the samples prepared with sintering

aids and the significant improvements were observed. Many published works [56, 90] mentioned that the final density of ZrW_2O_8 is improved by adding a minute amount of Al_2O_3. From the WO_3 and Al_2O_3 bi-phase diagram [91], during the sintering, the balanced reaction can be expressed in Eq. (3). One can find that $Al_2(WO_4)_3$ can only exist at a temperature higher than 720°C, and the compound changes to be liquid phase once the temperature is higher than 1135°C. Therefore, a liquid phase exists if the soaking temperature is set at 1160°C. The presence of the liquid will promote the densification kinetics, improving the final relative density. This was consistent with the micrographs shown in Figure 4.7(f) and (g).

$$Al_2O_3 + 3WO_3 \rightarrow Al_2(WO_4)_3 \qquad (4.3)$$

Many proportions of Al_2O_3 (0.1%, 0.4%, 0.7%, 1%, and 5% weight) were added into the mixture to see the effect, and the highest density without causing the distortion of the sample shape was achieved by the mixture with 0.4% sintering aids. If the liquid phase during the sintering become abundant with too much sintering aid, which certainly destroys the final shape.

Table.4.2. Mixture composition and sintered density

No	Mixture composition (wt%)	Sintered density (g/cm^3)	Theoretical density (g/cm^3)	Relative density (%)
a	79%W-Fluka+21%CERAC	4.421	5.09	86.8%
b	75% W-Fluka +4%nano WO_3 +21%CERAC	4.656	5.09	91.5%
c	71% W-Fluka +8%nano WO_3 +21%CERAC	4.583	5.09	90%
d	47% W-Fluka +32%nano WO_3 +21%CERAC	4.473	5.09	87.9%
e	79%%nano WO_3 +21%CERAC	3.658	5.09	71.9%
f	79%W-Fluka+21%CERAC+ 0.4%Al_2O_3	4.632	5.09	91%
g	75% W-Fluka +4%nano WO_3 +21%CERAC+ 0.4%Al_2O_3	4.799	5.09	94.3%
h	75% W-Fluka +4%nano WO_3 +21%CERAC+ 0.4%MgO	4.883	5.09	95.9%

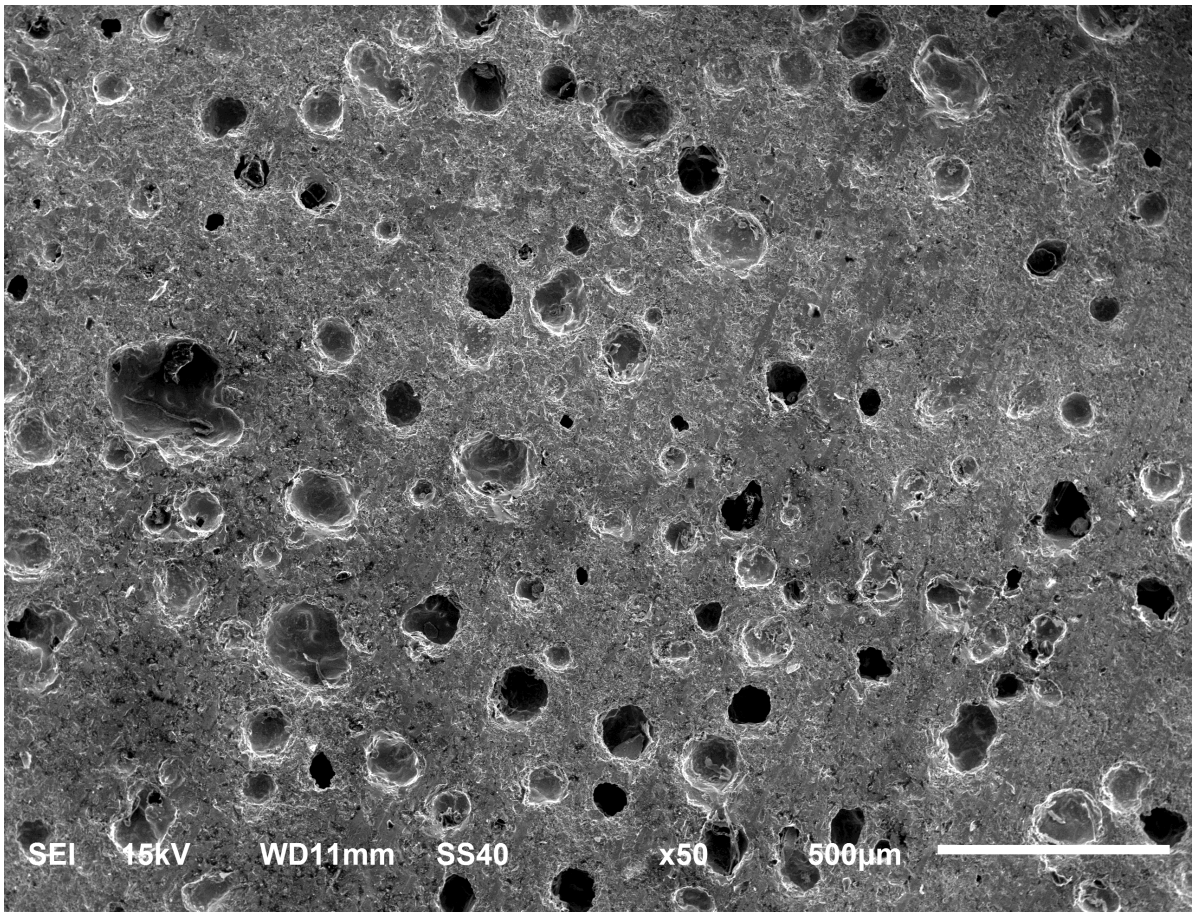

(a)

Figure 4.7. SEM micrographs of sintered sample: (a) no nano-sized WO_3 powder; (b) 4%; (c) 8%; (d) 32%; (e) 79%; (f) no nano-sized WO_3 powder but with sintering aid (Al_2O_3); (g) 4%nano powder with sintering aid (Al_2O_3); (h) 4%nano powder with sintering aid (MgO). (Refer to table 4.2)

Figure 4.7 (cont'd)

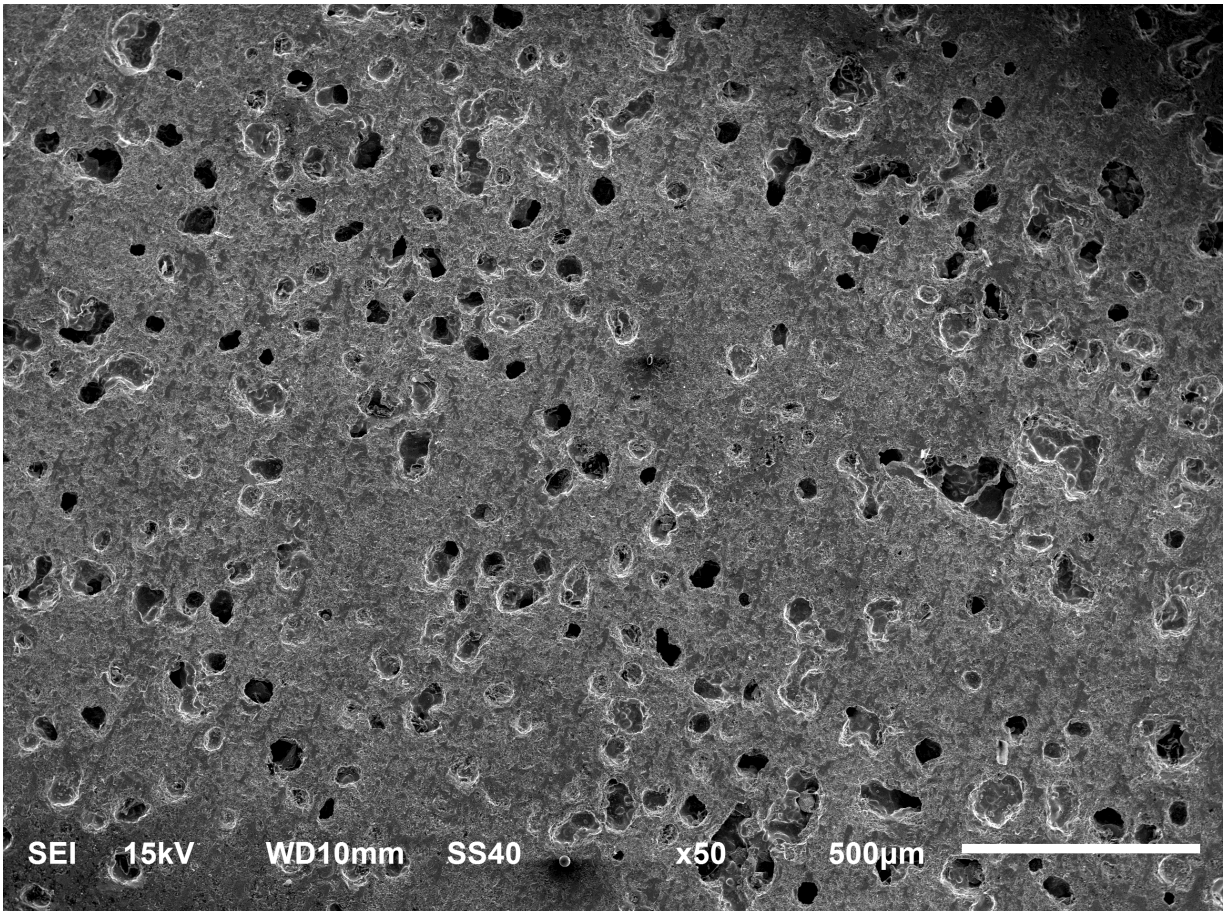

(b)

Figure 4.7 (cont'd)

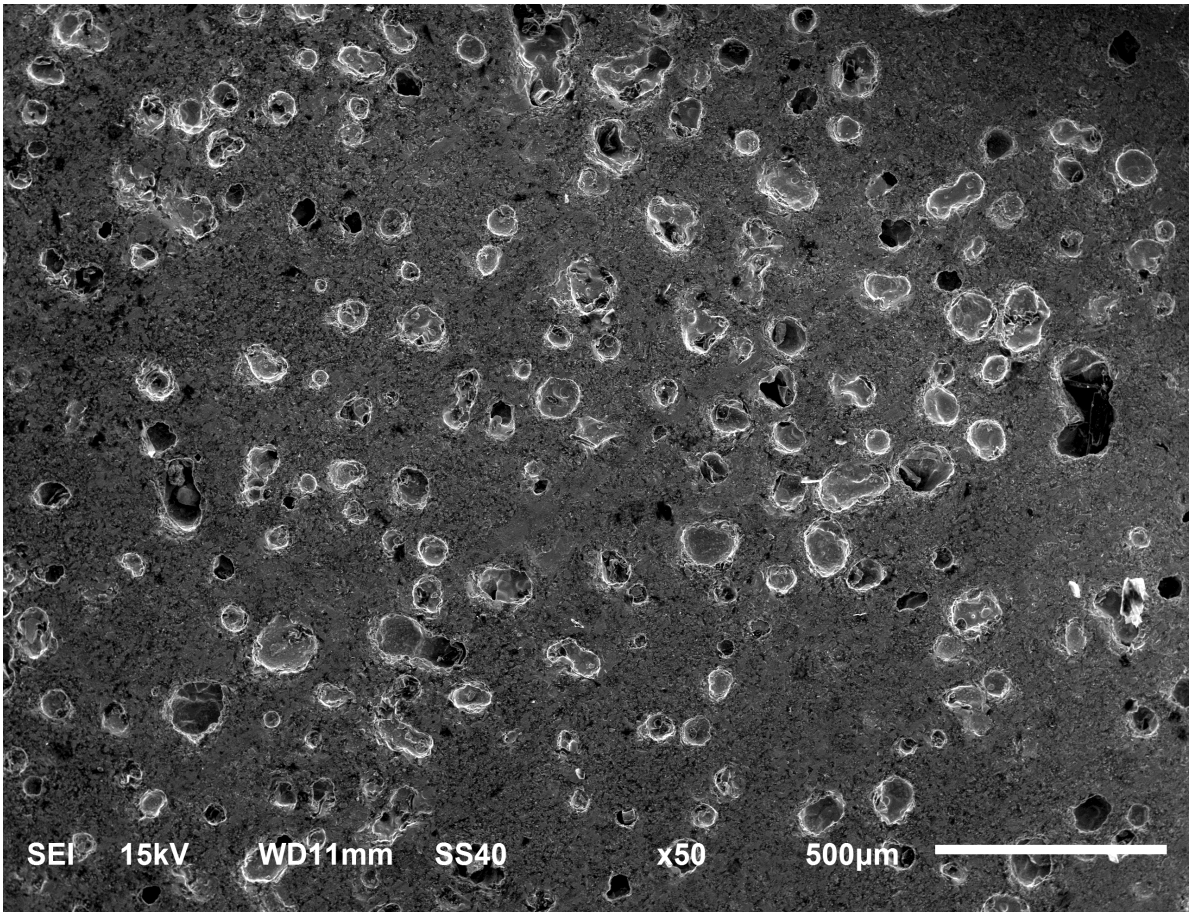

(c)

Figure 4.7 (cont'd)

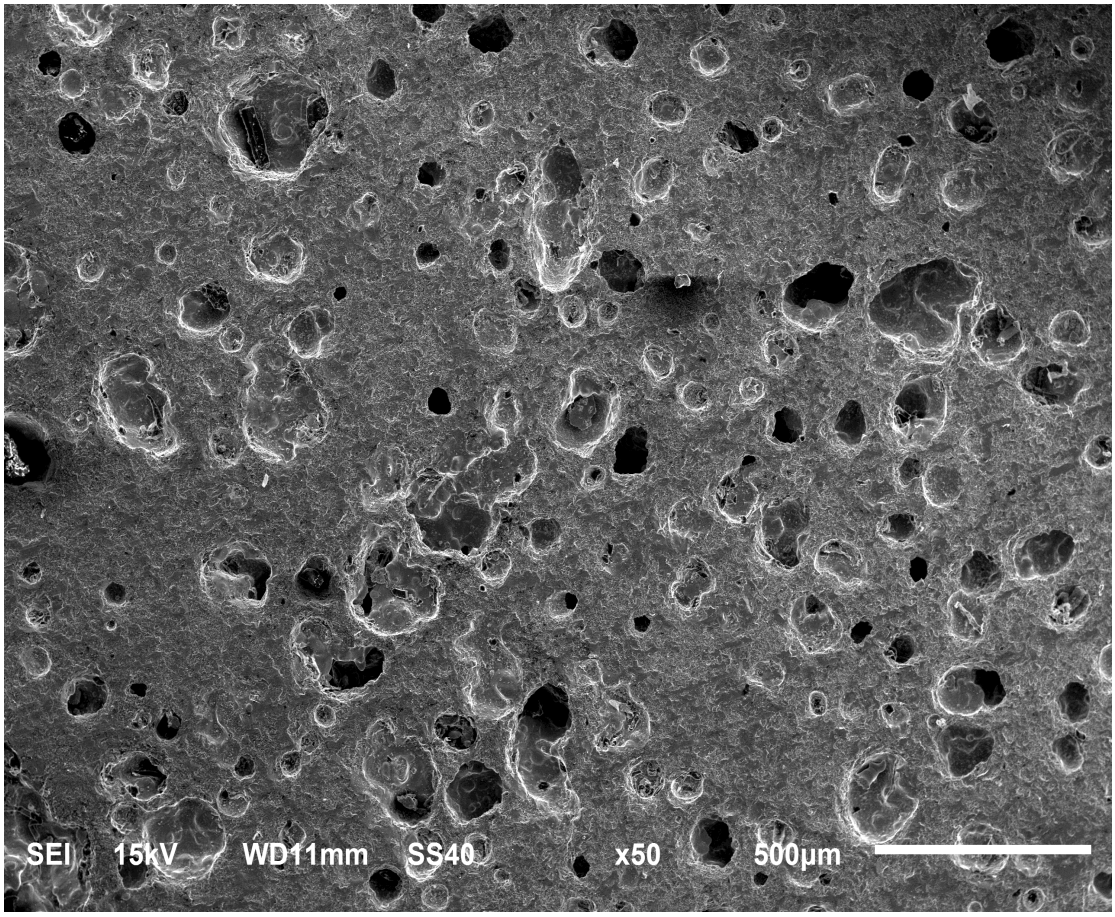

(d)

Figure 4.7 (cont'd)

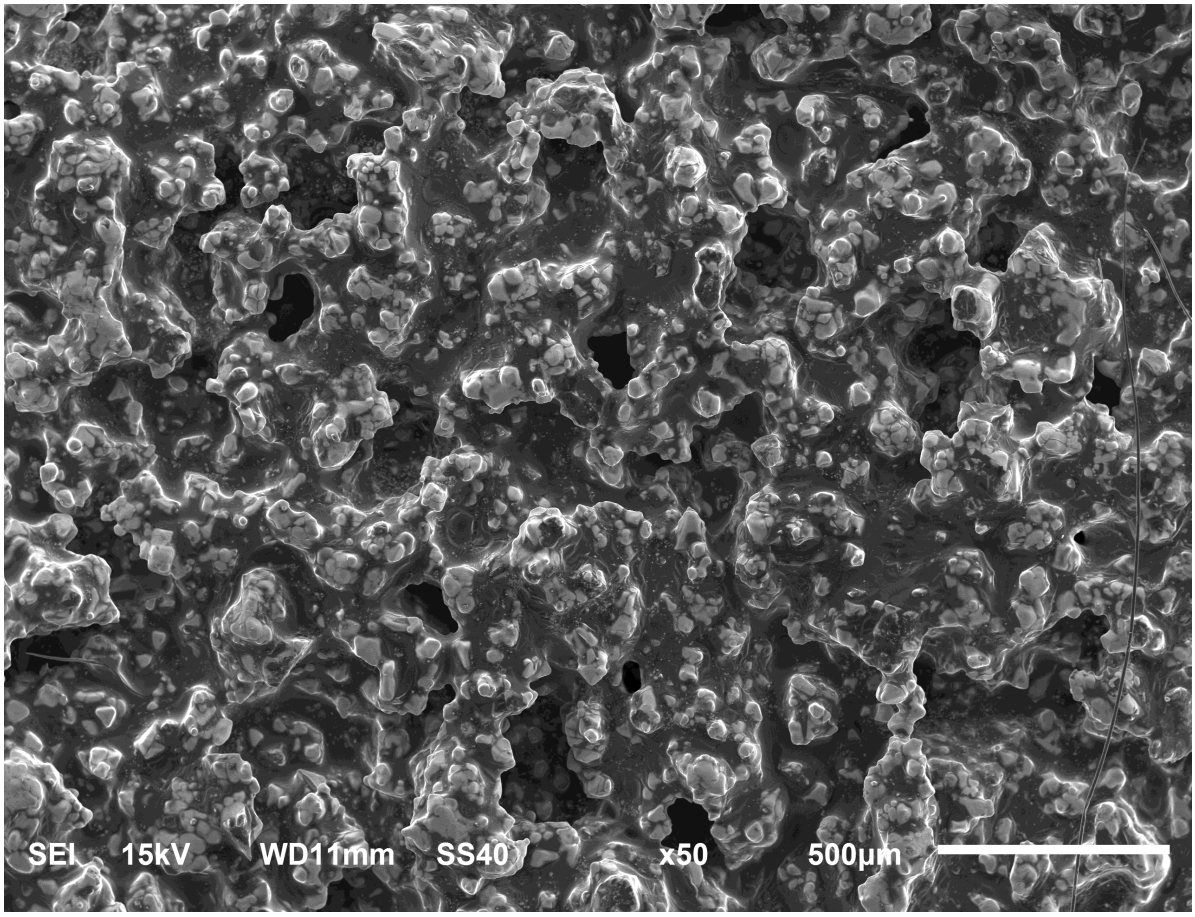

(e)

Figure 4.7 (cont'd)

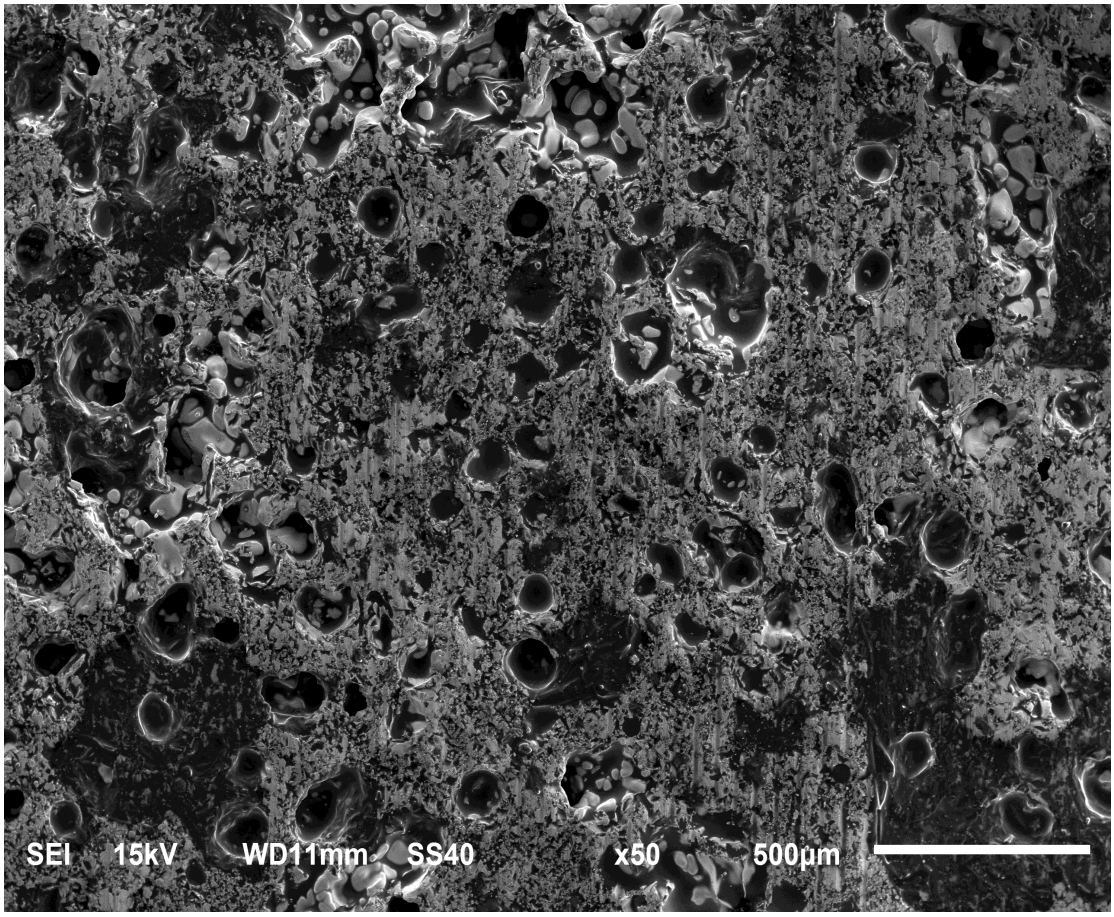

(f)

Figure 4.7 (cont'd)

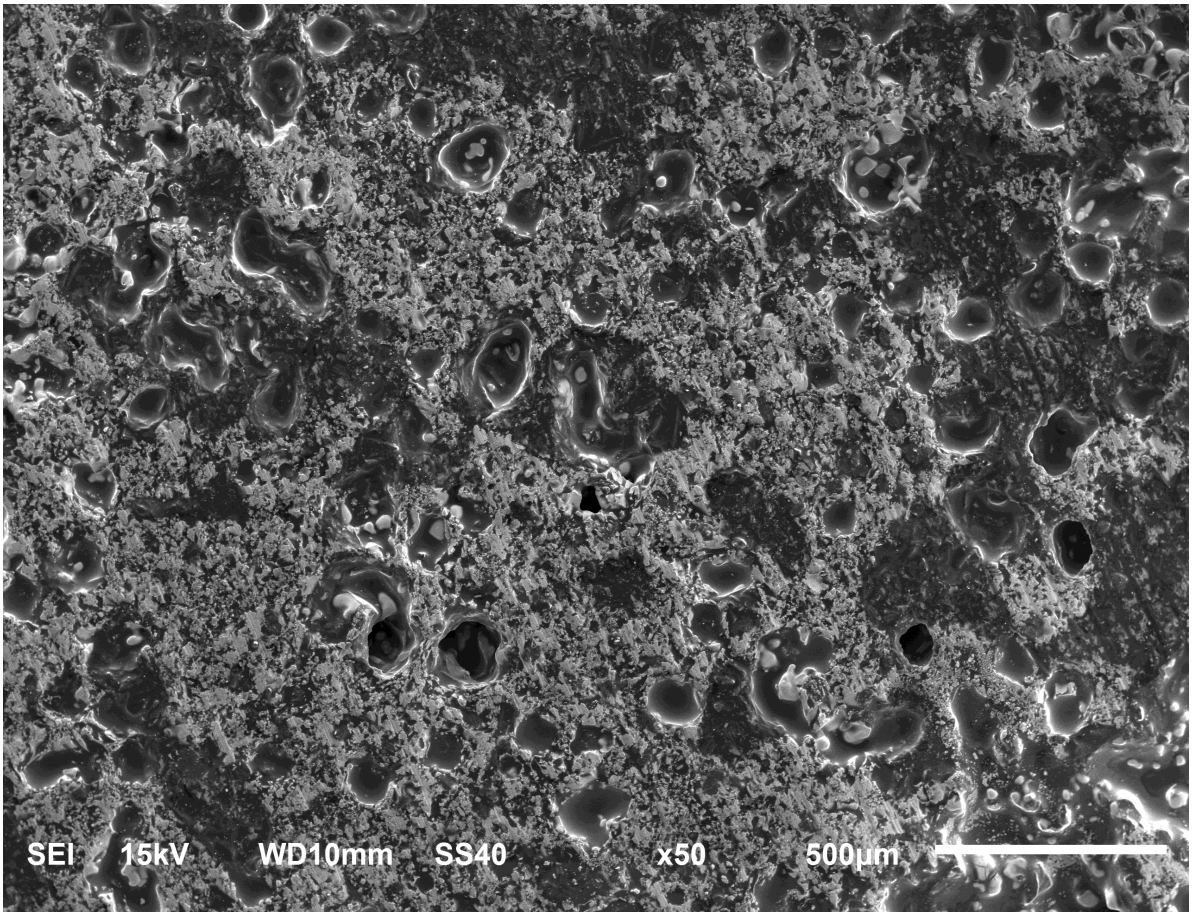

(g)

Figure 4.7 (cont'd)

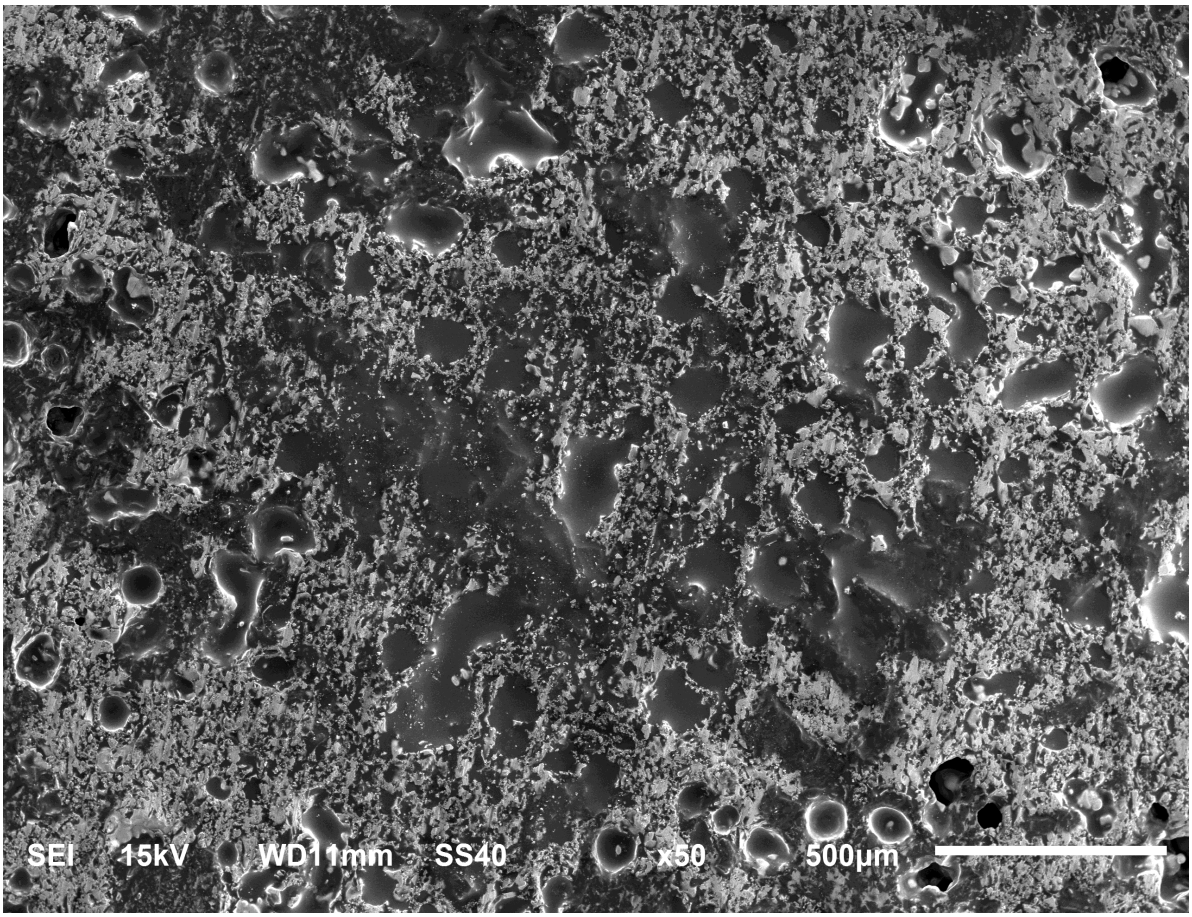

(h)

According to Table 4.2 and Figure 4.7(h), the sample with 0.4wt% MgO sintering aid also showed a good appearance and had the highest density among the eight samples. Several papers [92, 93, 94] discussed that Magnesium tungstate ($MgWO_4$) can be obtained by the reaction between MgO and WO_3 at 1000^{o}C to 1200^{o}C. The reaction can be described as Eq. (4.4)

$$MgO + WO_3 \rightarrow MgWO_4 \qquad (4.4)$$

A recent study [95] showed due to the combination of heavy (W) and light (Mg and O) elements, $MgWO_4$ was a new crystal scintillator, which can be widely used for various applications such as the detection of ionizing radiation and particles. In our study, $MgWO_4$ was used as a sintering additive to improve the final density of ZrW_2O_8 with reaction. From the MgO and WO_3 bi-phase diagram [96], WO_3 and $MgWO_4$ form a eutectic (tetragonal WO_3+ wolframite-structure $MgWO_4$) between 750-1125°C, and the $MgWO_4$ compound will become liquid phase once the temperature is higher than 1125°C. The liquid $MgWO_4$ was utilized to improve the final density since our soaking temperature is 1160°C. Similar to the Al_2O_3 sintering aid, several different proportions (0.1%, 0.4%, 0.7%, 1%, and 5% weight) of MgO were also added into the mixture. The sample cannot maintain a good shape once the amount exceeded the threshold of 0.4wt%.

4.3.3 The measurement of Young's modulus for different sintered samples

The final sintered samples were then tested with thermal mechanical analyzer (TMA) unit using the three-point bending method to measure Young's modulus. After sintering and polishing, the samples used in Young's modulus testing are cuboids shape, and the dimensions were: length, 13.5mm; thickness, 2mm; and width 4.5mm according to the

ASME standard. The formula to calculate the Young's modulus E (by bending) for rectangular bars is

$$E = \frac{Fl^3}{4\delta wt^3} \tag{4.5}$$

Where *F* is the increasing load giving the changing flexure, l is called effective length, which is the distance between supports, δ is the flexure measured, w is the sample width, and t is the sample thickness.

The Young's modulus of each sample in Table 4.2 at room temperature was calculated through equation 4.5, which are presented in Figure 4.8. The values of Young's modulus were consistent with the density values. Typically the denser the sample was, the higher for Young's modulus. The highest Young's modulus value was 4.58GPa, which was obtained by the mixture (75% W-Fluka +4%nano WO_3 +21%CERAC+ (0.4%) MgO).

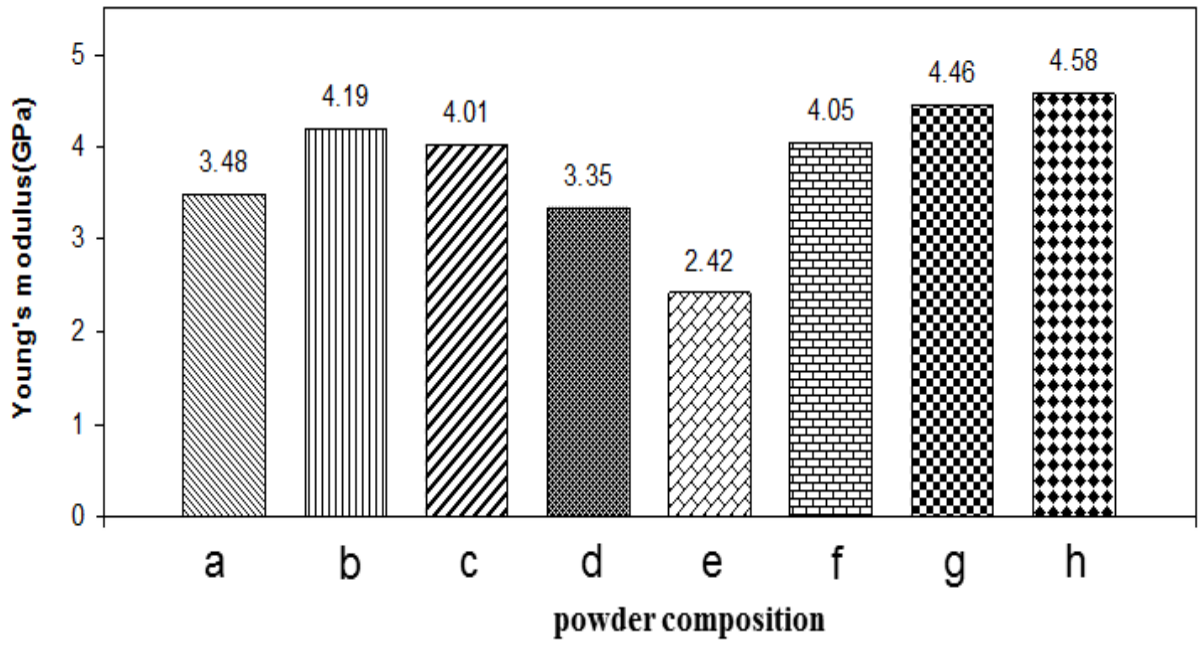

Figure 4.8. Young's modulus with different compositions for pure ZrW_2O_8 (refer to Table 4.2).

4.3.4 Young's modulus values predicted by Mori-Tanaka Method

The Mori-Tanaka Method [23] was originally concerned with calculating the average internal stress in matrix of a material containing precipitates with eigenstrains. Benveniste (1987) reformulated the model so that it can be applied to composite materials [28]. He considered anisotropic phases and ellipsoidal phases, and the application of the Mori–Tanaka method requires that the inclusion shape is ellipsoidal so that the stress and strain in each inclusion is constant. This ellipsoidal shape includes a wide variety of shapes such as cylinders, spheres, discs and ribbons.

In this thesis, the voids inside the matrix material were assumed as spherical pores full of air. Thus, the Mori-Tanaka scheme was considered to calculate the Young's modulus of the porous ZrW_2O_8, and make a comparison with experiment values. The physical implications are that the particle sees a matrix material with an average stress state provided by the average in the matrix. The effective stiffness tensor, $\boldsymbol{C_{ef}}$, is used to calculate the Young's modulus, *E*, for the stiffness matrix.

$$C_{ef} = C_m + v(C_i - C_m)A_i \tag{4.6}$$

Where $\boldsymbol{C_m}$ and $\boldsymbol{C_i}$ are the stiffness tensors of the matrix and inclusion materials as pores, respectively, *v* is the volume fraction of the inclusion phase. $\boldsymbol{A_i}$ is the inclusion strain concentrator tensor defined as

$$A_i = T[(1 - v)I + vT]^{-1} \tag{4.7}$$

Where I is the forth rank identity tensor and ***T*** is Wu's tensor [33] defined as

$$T = [I + ES_m(C_i - C_m)]^{-1} \tag{4.8}$$

Where ***E*** is Eshelby's tensor decided by the shape of the inclusion [30], and $\boldsymbol{S_m}$ is the compliance tensor of the matrix material.

For our experiment, the ZrW_2O_8 is isotropic material, and the shape of inclusions was assumed as spherical. Combining Eqs. (4.6)-(4.8), the composite Young's modulus, E

can be calculated as

$$E = \frac{(C_{11}-C_{12})(C_{11}+2C_{12})}{C_{11}+C_{12}} \tag{4.9}$$

The theoretical Young's modulus of ZrW_2O_8 is taken as 5GPa [97], and the Poisson's ratio is 0.3 [97]. In our experiment, we assumed the voids of composite were full of air. We found the bulk modulus of air is 1.01×10^5Pa from [98], and the poisson's ratio is 0 according to [99].

We take the highest density sample as an example to show the calculation process, and in order to obtain the Young's modulus values, the stiffness tensors of the matrix $\boldsymbol{C_m}$ and inclusion materials $\boldsymbol{C_i}$ need to be calculated first.

$$C_i = \begin{bmatrix} 0.3*10^{-3} & 0 & 0 & 0 & 0 & 0 \\ 0 & 0.3*10^{-3} & 0 & 0 & 0 & 0 \\ 0 & 0 & 0.3*10^{-3} & 0 & 0 & 0 \\ 0 & 0 & 0 & 0.15*10^{-3} & 0 & 0 \\ 0 & 0 & 0 & 0 & 0.15*10^{-3} & 0 \\ 0 & 0 & 0 & 0 & 0 & 0.15*10^{-3} \end{bmatrix} \tag{4.10}$$

$$C_m = \begin{bmatrix} 6.73 & 2.8846 & 2.8846 & 0 & 0 & 0 \\ 2.8846 & 6.73 & 2.8846 & 0 & 0 & 0 \\ 2.8846 & 2.8846 & 6.73 & 0 & 0 & 0 \\ 0 & 0 & 0 & 1.9231 & 0 & 0 \\ 0 & 0 & 0 & 0 & 1.9231 & 0 \\ 0 & 0 & 0 & 0 & 0 & 1.9231 \end{bmatrix} \tag{4.11}$$

In order to find the Wu's tensor, we need to calculate Eshelby's tensor ***E*** first, which is decided by the shape of the inclusion. The second step it to obtain the compliance tensor of the matrix material, which is the inverse form of stiffness tensor.

$$E = \begin{bmatrix} 0.5238 & 0.0476 & 0.0476 & 0 & 0 & 0 \\ 0.0476 & 0.5238 & 0.0476 & 0 & 0 & 0 \\ 0.0476 & 0.0476 & 0.5238 & 0 & 0 & 0 \\ 0 & 0 & 0 & 0.5238 & 0 & 0 \\ 0 & 0 & 0 & 0 & 0.5238 & 0 \\ 0 & 0 & 0 & 0 & 0 & 0.5238 \end{bmatrix} \quad (4.12)$$

$$S = \begin{bmatrix} 0.2 & -0.06 & -0.06 & 0 & 0 & 0 \\ -0.06 & 0.2 & -0.06 & 0 & 0 & 0 \\ -0.06 & -0.06 & 0.2 & 0 & 0 & 0 \\ 0 & 0 & 0 & 0.5200 & 0 & 0 \\ 0 & 0 & 0 & 0 & 0.5200 & 0 \\ 0 & 0 & 0 & 0 & 0 & 0.5200 \end{bmatrix} \quad (4.13)$$

Combined the calculated stiffness tensor with the forth-rank identity tensor I, and utilizing the equation 4.8, the Wu's tensor ***T*** is shown as follow.

$$T = \begin{bmatrix} 2.1472 & 0.2385 & 0.2385 & 0 & 0 & 0 \\ 0.2385 & 2.1472 & 0.2385 & 0 & 0 & 0 \\ 0.2385 & 0.2385 & 2.1472 & 0 & 0 & 0 \\ 0 & 0 & 0 & 2.0998 & 0 & 0 \\ 0 & 0 & 0 & 0 & 2.0998 & 0 \\ 0 & 0 & 0 & 0 & 0 & 2.0998 \end{bmatrix} \quad (4.14)$$

The volume fraction *v* for the highest sintered density sample is taken as 0.041, and with Wu's tensor, the inclusion strain concentrator tensor $\boldsymbol{A_i}$ can be calculated as,

$$A_i = \begin{bmatrix} 2.0469 & 0.2068 & 0.2068 & 0 & 0 & 0 \\ 0.2068 & 2.0469 & 0.2068 & 0 & 0 & 0 \\ 0.2068 & 0.2068 & 2.0469 & 0 & 0 & 0 \\ 0 & 0 & 0 & 2.0092 & 0 & 0 \\ 0 & 0 & 0 & 0 & 2.0092 & 0 \\ 0 & 0 & 0 & 0 & 0 & 2.0092 \end{bmatrix} \quad (4.15)$$

Thus, according to the equation 4.6, the effective stiffness tensor, $\boldsymbol{C_{ef}}$ will finally be calculated as,

$$C_{ef} = \begin{bmatrix} 6.1163 & 2.5610 & 2.5610 & 0 & 0 & 0 \\ 2.5610 & 6.1163 & 2.5610 & 0 & 0 & 0 \\ 2.5610 & 2.5610 & 6.1163 & 0 & 0 & 0 \\ 0 & 0 & 0 & 1.7647 & 0 & 0 \\ 0 & 0 & 0 & 0 & 1.7647 & 0 \\ 0 & 0 & 0 & 0 & 0 & 1.7647 \end{bmatrix} \quad (4.16)$$

The final composite Young's modulus can be obtained with the first two components in the effective stiffness matrix, $\mathrm{C}_{11,}\ \mathrm{C}_{12}$.

$$E = \frac{(C_{11} - C_{12})(C_{11} + 2C_{12})}{C_{11} + C_{12}} = 4.6046GPa$$

The calculation process is listed above to show how we get the predicted Young's modulus value with volume fraction. Table 4.3 showed the different $C_{11,}\ C_{12}$ of the effective stiffness matrix based on the volume fraction.

Table 4.3 Experimental data and theoretical prediction by Mori-Tanaka method

Volume fraction v	C_{11}	C_{12}	Young's modulus calculated (GPa)	Young's modulus measured (GPa)
0.132	4.9649	1.9845	3.8315	3.48
0.085	5.5273	2.261	4.2145	4.19
0.1	5.3409	2.1683	4.0887	4.01
0.121	5.091	2.0456	3.9183	3.35
0.281	3.5253	1.3227	2.8035	2.42
0.09	5.4644	2.2296	4.1722	4.05
0.057	5.8944	2.4468	4.4589	4.46
0.041	6.1163	2.561	4.6046	4.58

The predicted modulus was calculated using the Mori-Tanaka, and combined with the measured Young's modulus, the data was shown in Figure 4.9. The Mori-Tanaka method has a very good agreement with experiment results, especially when the relative density is higher than 90%.

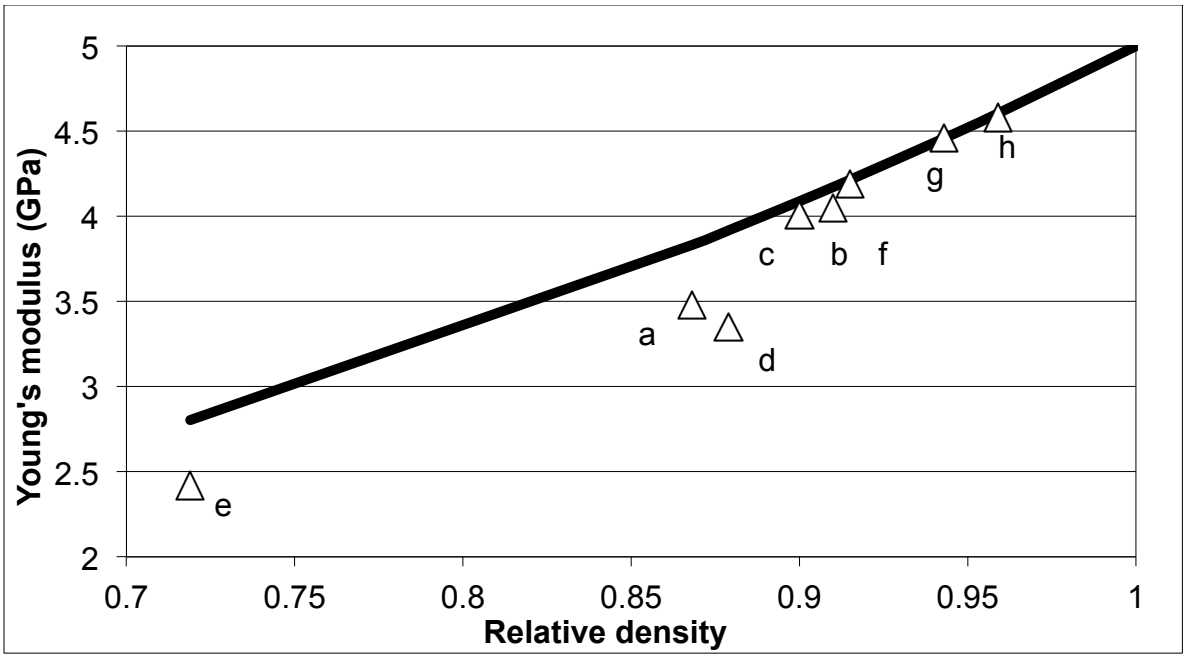

Figure 4.9. Experimental data and Mori-Tanaka predictions (refer to Table 4.2).

4.4 CONCLUSION

Several groups of powder mixtures with nano-powders and sintering aids were compacted and sintered. The initial packing density was investigated in relation to the compacting stress. Mixing with nano-powders did not improve the compaction characteristics due to the high friction but enhanced the densification of the mixtures during sintering instead. The high surface area of nanopowders has increased the driving potential for densification. The experiment results also showed the optimal amount of nano-powders for the mixture as the relative sintered density can be increased by 5% by adding 4wt% nanopowders.

Several groups of mixture have been tested to find the optimum amount of sintering aids for the sintered compound, including 0.1wt%, 0.5wt%, 1wt% and 2wt%. A small amount (0.4wt%) of Al_2O_3 or MgO can help achieve the highest density for the smaple. This turns out to be an efficient method to increase the final density by approximately 5%. In this case, the reason for improvement is that the liquid phase was formed to enhance the final relative density for both Al_2O_3 and MgO. Few works have reported that the sintered density of ZrW_2O_8 can be enhanced by small amount of Al_2O_3 additive. This is the first time to report MgO as an additive in improving the final density for ZrW_2O_8. In this work, the highest sintered density (95.9%) was achieved by the combination of 4wt% nanopowders and 0.4wt% MgO as a sintering aid.

The relevant Young's modulus of different samples was also measured using the three points bending method, and the values were consistent with the measured density. The highest value (4.58GPa) was obtained with the sample with the highest density. The Mori-Tanaka method was introduced to predict the Young's modulus and had a very good agreement with experiment results once we took the porous media as a particle filled with air. This study indicated that the mechanical strength was improved by trying to attain high packing and to improve the sintering potential.

CHAPTER 5 CONCEPT PROVING WITH SIMPLE ASSEMBLY FOR THERMAL BUCKLING AND FUTURE WORKS

5.1 CONCEPT PROVING WITH HOMOGENEOUS ASSEBLY

5.1.1 Simulation of thermal buckling with homogeneous assembly

The buckling deformation simulation was implemented with several loading conditions. They were described as follows: (a) Contact defined between the front interface of the tiles and the corresponding interface on the core as “no separation”, (b) Spherical hinges applied to tiles to simulate a surrounding RCC rotational restriction, (c) Uniform thermal loading of 800^{o}C applied to the top surface, and 50^{o}C to the bottom.

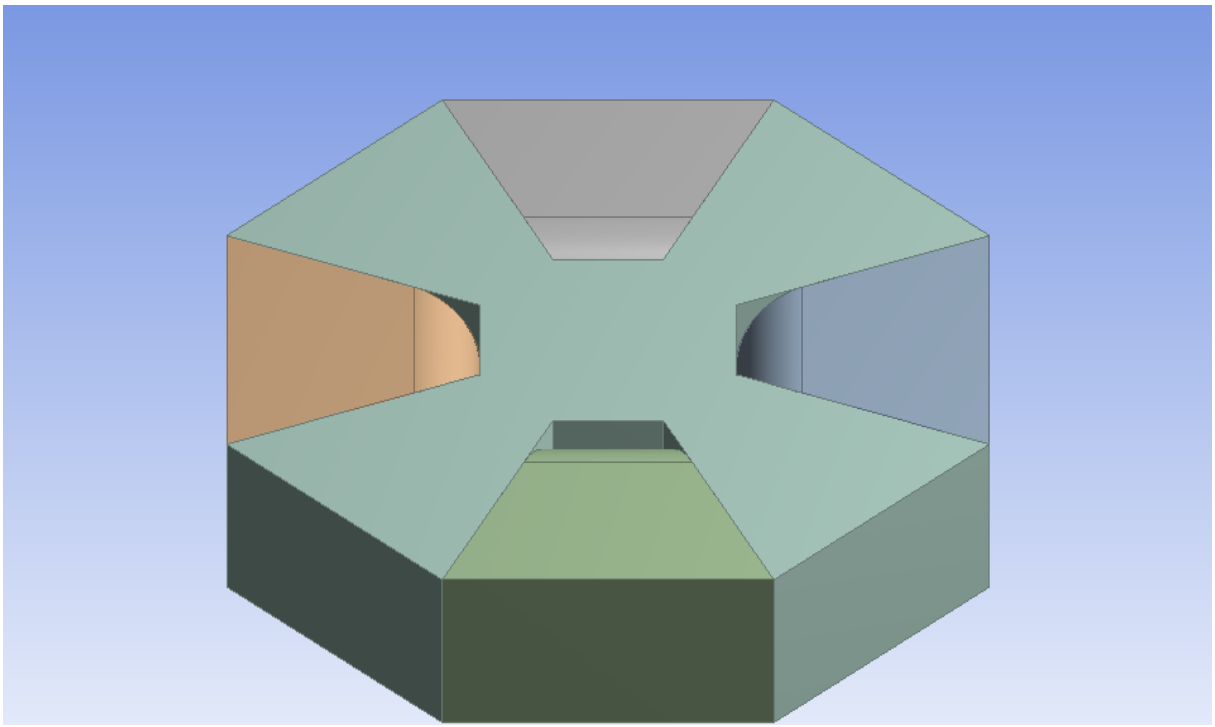

(a)

Figure 5.1. (a) Initial designed homogeneous model, (b) The simulation results after thermal loading.

Figure 5.1 (cont'd)

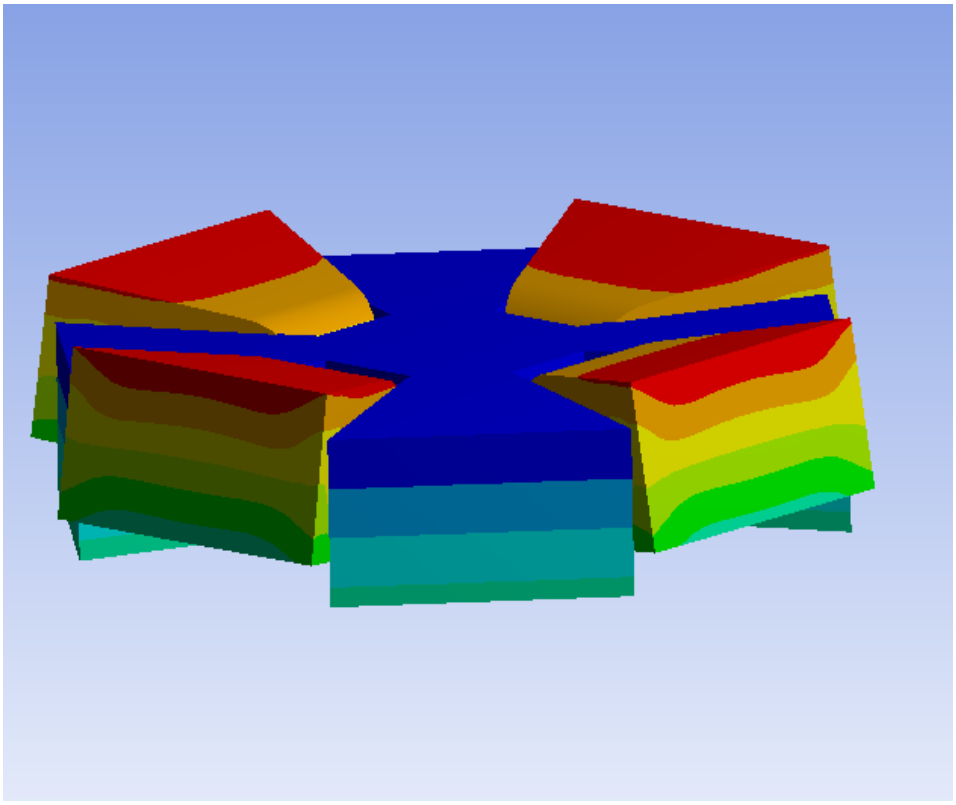

(b)

From the simulation results shown in Figure 5.1, although the deformation was not too much, the homogeneous tiles would rotate to push the core part downwards to behave buckling action. Therefore, it is convenient and feasible for us to make the homogeneous assembly to testify the buckling action and avoid the complex manufacturing process first.

5.1.2 Sintered homogeneous assembly and its optimization

The homogeneous samples were manufactured according to the methods described in chapter 3. Each part was compacted and partially sintered, and then was machined to designed shape to compose the assembly. The initial assembly and parts were shown in Figure 5.2.

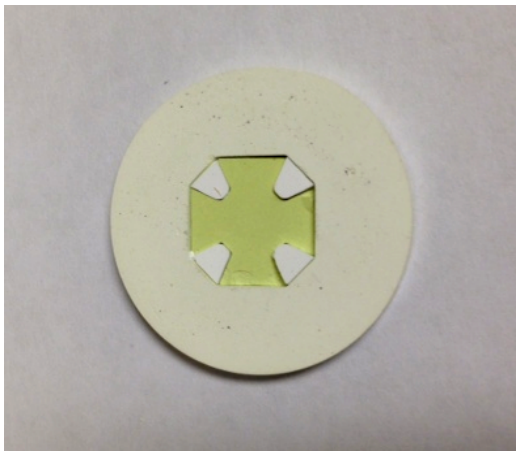

(a)

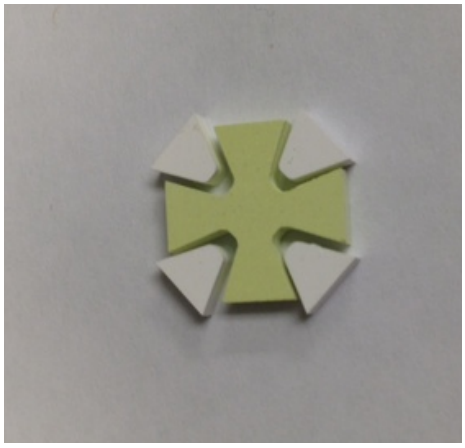

(b)

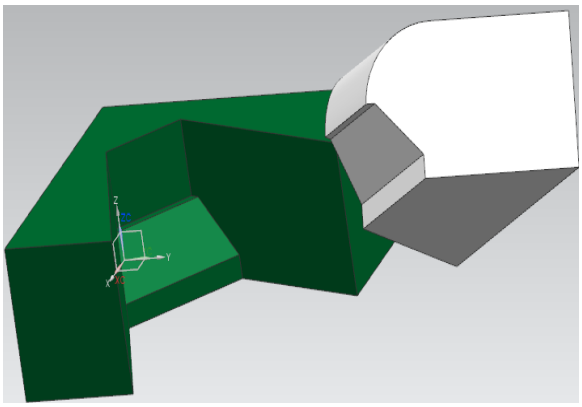

(c)

(d)

Figure 5.2 (a) Simple assembly with big core part, (b) Optimized core part with adjusted area, (c) the optimized design with a chamfer, (d) the real machining sample with chamfers

Figure 5.2(a) was a simple assembly, but the core part was relatively big compared to the tiles. Therefore, it was very difficult to make the assembly buckle downwards. The optimized sample was made to decrease the area of core part, shown in Figure 5.2(b). According to Figure 5.2(c), a 45-degree chamfer was added to the tip of the ZrO_2 and inside of ZrW_2O_8. This was done to promote buckling and was shown to help in our computer simulation. Figure (d) showed the perfect sample for the core part after machining.

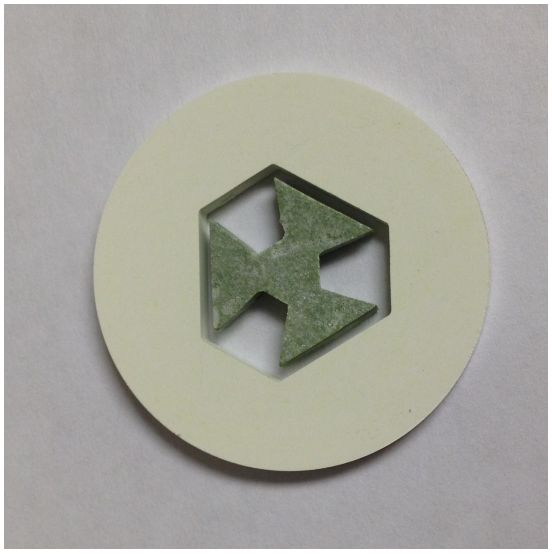

(a)

Figure 5.3 (a) The assembly before sintering, (b) Octagonal shape sample after sintering, (c) Hexagonal shape sample after sintering.

Figure 5.3 (cont'd)

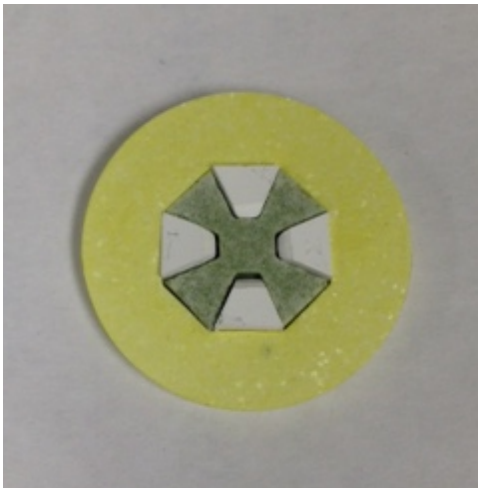

(b)

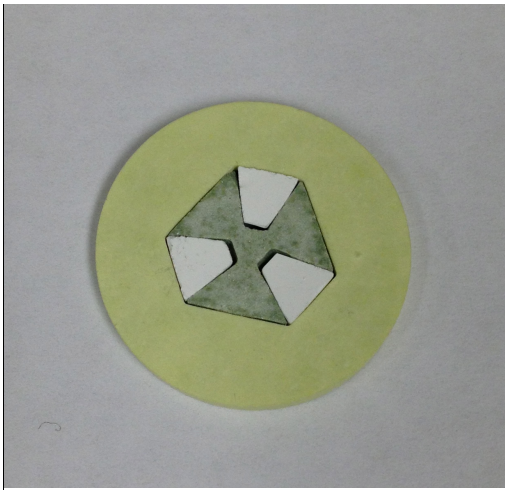

(c)

During the experiment, samples with different shapes like octagonal and hexagonal were made to examine the differences in buckling behaviors. Figure 5.3 showed the samples before and after sintering. The diameter of circular outside skin part shown in Figure 5.3 is 30mm, and the whole assembly is relatively small. One possibility of increasing the size of assembly to promote the buckling was considered, as it is difficult for the assembly to buckle with such small geometry.

The complicated assembly with FGM tile parts was shown in Figure 5.4. The center core part was made of pure ZT, which can shrink during the working temperature to release the initial pressure between each part. The tile part was made with ZT, which was embedded with ZO core to have multi-dimensional CTE value.

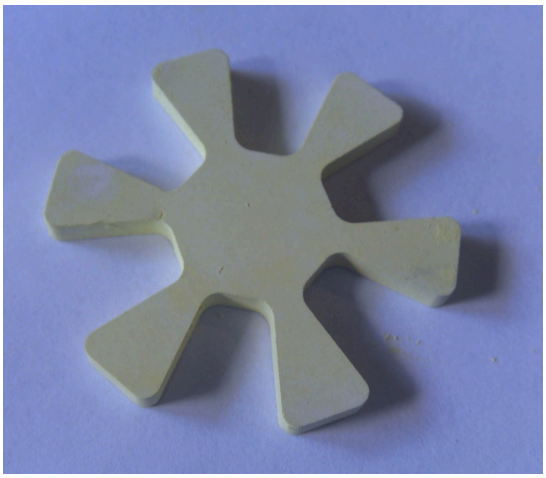

(a)

(b)

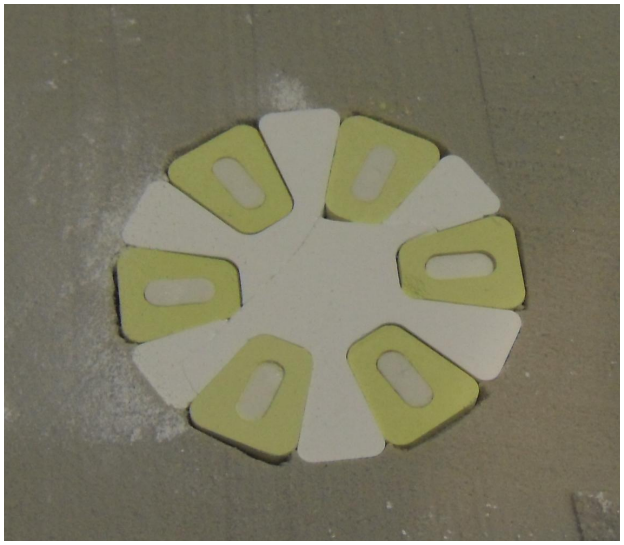

(c)

Figure 5.4. Experimental assembly of thermal buckling structure, (a) core part, (b) tile part, (c) assembly.

The assembly was almost the same with simulated model, which indicated the proposed plan was feasible. However, it is quite challenging to sinter the six tiles and core part together to have a perfect fit. Thus, the simple homogenous assembly was tried first to verify the ideas.

CHAPTER 6 CONCLUSIONS

The main contributions of this study are listed below,

1. The previous design had the core made of ZrW_2O_8 shrink-fitted into the RCC. When the temperature increases, a gap is formed between the core and the RCC skin due to their distinct CTE difference. Because the materials available have limited CTE ranges (typically in 10^{-6}/°C), the gap generated by this simple in-plane thermal deformation cannot achieve a high cooling capacity. Therefore, in this study, a new design approach has been pursued to drastically improve the cooling capacity by utilizing a buckling action. The core was made of ZrW_2O_8 and/or complex/multidimensional FGMs to trigger the buckling under certain loading condition. The tiles were specially designed to exhibit high positive thermal expansion radially and modest negative thermal expansion circumferentially. The reason for a negative circumferential CTE is to avoid the tiles getting stuck with the core during the buckling. In addition, the tiles was designed to have a through-the-thickness gradiency - higher thermal expansion on the exterior surface and negative thermal expansion on the interior surface - to trigger the required buckling action easily.
2. Complex FGMs utilizing shrink-fitting methods of pre-sintered ceramic samples were fabricated. When these tiles are assembled, they exert compressive force to induce a buckling action among the tiles. The FEM simulation verified that the

model buckled under the proper material parameters and an expected loading condition. Mainly ZrW_2O_8 and ZrO_2 tiles with a designed shape were partially sintered and machined, and with a dimensional compensation, the perspirable skin assembly was successfully fabricated. To enhance the buckling action, a complex multi-dimensional FGM tile was fabricated to decrease the contact area of the core and tile part in the designed simulation. It was found that each layer was joined with other layers through a reaction to fabricate the FGM tiles with good shape control and mechanical integrity.

3. The powder mixing process changes the compaction capability of the powder mixtures. The initial relative density depends on the ratio between the average particle sizes as well as the difference in the initial density of two powders. Mixing the ZT mixture with nano-powders did not improve the compaction characteristics due to the inherent high friction with small particles but enhanced the densification process during sintering. The high surface area of nanopowders has increased the driving potential for densification. The experiment results also showed the optimal amount of nano-powders for the mixture as the relative sintered density can be increased by 5% by adding 4wt% nanopowders.
4. Several groups of mixture with different amount sintering additives (0.1wt%, 0.5wt%, 1wt% and 2wt%) have been fabricated to find the optimum value for the compound. A small amount (0.4wt%) of Al_2O_3 or MgO can help achieve the highest density for the samples. This turns out to be an efficient way to improve the density by approximately 5%. In this case, the reason for the improvement is that the liquid phase was formed to enhance the relative density for both Al_2O_3

and MgO. This is the first time to report MgO as an additive in improving the final density for ZrW_2O_8. In this work, the highest sintered density (95.9%) was achieved by the combination of 4wt% nanopowders and 0.4wt% MgO as a sintering additive.

5. The relevant Young's modulus values of different samples were also measured using the three points bending method, and the values were consistent with the measured density. The highest Young's modulus (4.58GPa) corresponded the highest density sample. The Mori-Tanaka method was introduced to predict the Young's modulus and had a very good agreement with experiment results once we took the porous media as the pores filled with air and used air as a second phase. When the relative density is higher than 90%, there is only slight difference between the theoretical and experimental data (0.5% relative error for sample h in table 4.2).
6. Homogeneous samples with different shapes like octagonal and hexagonal were made to test the buckling behaviors. Some complicated FGM tiles were also made to compose the designed assembly in the simulation.

REFERENCES

REFERENCES

[1] Angelo J. A., 1999, The dictionary of space technology, New York, NY: Facts on File, pp. 211-25.

[2] NASA Facts, 2006, “Orbiter Thermal Protection System”, FS-2004-09-014-KSC (Rev. 2006), pp. 1-6.

[3] Cleland G. G., Iannetti F., 1989, "Thermal protection system of the space shuttle", NASA contractor report: NASA CR-4227, pp.1-17.

[4] NASA, 2003, “Follow the TPS”, Columbia Accident Investigation Board Report, Vol. 4, pp. 1-12.

[5] Savage G., 1993, Carbon-carbon composites, New York, NY, Chapman & Hall, pp. 37-80 & pp. 322-350.

[6] Kieback B., Neubrand A. and Riedel H., Processing techniques for functionally graded materials, Mater. Sci. Eng. A 362 (2003). pp. 81–105.

[7] Kalpakjian S., Schmid S. R. Manufacturing Processes for Engineering Materials, Upper Saddle River, NJ, Pearson Education, Inc. 2008, pp. 669-726.

[8] German R.M., 1994, Powder metallurgy science, 2nd ed., Metal powder industries federation, Princeton, pp. 15-24, 210-221, 241-262.

[9] C.W.Yip, J.A.Hersey. Perfect powder mixtures, Powder Technol., 16(1977), pp. 189-192.

[10]R.L. Coble. Sintering Crystalline Solids, I. Intermediate and Final State Diffusion Models, J. Appl. Phys. 32(1961), pp. 787.

[11]Barsown, M., 1997, Chapter 10: Sintering and Grain Growth, in Fundamental of Ceramics, New York: The McGraw-Hill Companies, Inc., pp. 331-385.

[12]German R.M., 1994, Powder metallurgy science, 2nd ed., Metal powder industries federation, Princeton, pp. 15-24, 210-221, 242-262.

[13]Legros, C., Carry, C., Bowen, P. and Hofmann, H. Sintering of a Transition Alumina: Effects of Phase Transformation, Powder Characteristics and Thermal Cycle, J. Eur. Ceram. Soc., 19(1999), pp. 1967-1978.

[14]Suk-Joong L. Kang. Sintering: Densification, Grain Growth and Microstructure. Elsevier’s Science. UK (2005), pp. 173.

[15]Z.H. Huang*, D.C. Jia, Y. Zhou, Y.J. Wang. Effect of a new additive on mechanical properties of hot-pressed silicon carbide ceramics. Materials Research Bulletin 37 (2002) pp. 933-940.

[16]J.H. She* and K. Ueno. EFFECT OF ADDITIVE CONTENT ON LIQUID-PHASE SINTERING ON SILICON CARBIDE CERAMICS. Materials Research Bulletin, 34(1999). pp. 1629–1636.

[17]Alfian Noviyanto, Dang-Hyok Yoon. Metal oxide additives for the sintering of silicon carbide: Reactivity and densification. Current Applied Physics. 13 (2013) pp. 287-292.

[18]Pauli Pedersen. On Shrink Fit Analysis and Design. Computer Mech. 37 (2006) pp. 121–130.

[19]Hamid Jahed1, Behrooz Farshi. Optimum Autofrettage and Shrink-Fit Combination in Multi-Layer Cylinders. Journal of Pressure Vessel Technology. 128(2006) pp.196-200.

[20]Alfian Noviyanto, Dang-Hyok Yoon. Metal oxide additives for the sintering of silicon carbide: Reactivity and densification. Current Applied Physics. 13 (2013) pp. 287-292.

[21]Taya M and Arsenault R. Metal Matrix Composites. 1st edition, Pergamon Press, (1989), pp. 23.

[22]"Stiffness of long fibre composites". University of Cambridge. Retrieved 1 January 2013.

[23]T. Mori, and K. Tanaka, Average stress in matrix and average elastic energy of materials with misfitting inclusions. Acta. Metal. 21(1973), pp. 571-574.

[24]P. S. Turner. Thermal Expansion Stresses in Reinforced Plastics. J. Res. Natl. Bureau. Stand. 37(1946), pp. 239.

[25]E. H. Kerner. The Elastic and Thermo-Elastic Properties of Composite Media. Proc. Phys. Soc. B., 69(1965), pp. 808.

[26]B.W. Rosen, and Z. Hashin. Effective thermal expansion coefficients and specific heats of composite materials. Int. J. Eng. Sci. 8(1970), pp. 157.

[27]V. M. Levin. Thermal expansion coefficients of heterogeneous materials, Mekhanika Tuerdogo Tela, 2(1967), pp. 88.

[28]Y. Benveniste. A new approach to the application of Mori-Tanaka's theory in composite materials. Mech. Mater. 6(1987), pp. 147.

[29]P. Kwon, and C.K. H. Dharan. Effective moduli of high volume fraction particulate composites. Acta. Metall. Mater. 43(1995), pp. 1141.

[30]Mura, T., Micromechanics of Defects in Solids, 2nd edition, Martinis Nijihoff, New York (1987), pp. 79.

[31]J. Aboudi, 1991, Mechanics of composite materials, a unified micromechanical approach. (Elsevier, New York), pp. 35-37.

[32]C. Nishimatsu, and J. Gurland, Experimental survey of the deformation of the hard-ductile two-phase alloy system WC-Co. Trans. Am. Soc. Metals. 52(1960), pp. 469.

[33]Wu, T. T., The effect of inclusion shape on the elastic moduli of a two-phase material. Int. J. Solids Struct. 2 (1966), pp. 1-8.

[34]Rabin BH and Shiota I. Special issue: functional gradient materials. MRS Bull. 20(1995), pp. 14–15.

[35]Markworth AJ, Ramesh KS, Review Modeling studies applied to functionally graded materials" Journal of Materials Science, 30(1995), pp. 2183-2193.

[36]Hirai T, Functionally gradient materials. In Materials Science and Technology, A comprehensive treatment, Vol. 17B, Processing of Ceramics, part II, Chapter 20, (1996), pp. 293–341.

[37]Kwon P, Dharan CKH, Ferrari M. Macroscopic analysis of axisymmetric functionally gradient materials under thermal loading. J Energy Res Technol. 116(1994), pp. 115-116.

[38]Erdogan F. Fracture Mechanics of Functionally Graded Materials, Composites Engineering, 5(1995), pp. 753-770.

[39]Koizumi M. Recent progress of functionally gradient materials in Japan, Ceram. Eng. Sci. Proc. 13(1992), pp. 333.

[40]Kieback B, Neubrand A, Riedel A. Processing techniques for functionally graded materials, Materials Science and Engineering A362 (2003). pp. 81–105.

[41]Miyamoto Y (1999) Functionally graded materials: design, processing, and applications, Chapter 6, pp. 163.

[42]Atarashiya K, Ishida Y andNagai T, (1993) Functionally gradient material of the system Ni-AIN by pressureless sintering, Functionally Gradient materials, Eds. Holt JB, Koizumi M, Hirai T and Munir ZA Ceram. Trans. American Ceramic Society Westerville, OH. pp. 141-148.

[43]Rabin, BH, Heaps RJ, (1993) Powder processing of Ni/Al_2O_3 FGM, Ceram. Trans. 34, "." Functionally Gradient Materials, edJ.B. Holt, M. Koizumi, T. Hirai, Z.A. Munir (Eds.), American Ceramic Society, Westerville, OH, pp. 173–180.

[44]Zhu J, Yin Z and Lai Z. Microstructure and Mechanical Properties of ZrO_2/Ni Functionally Gradient Material. J. Mater. Sci. Technol. 10(1994), pp. 188–192.

[45]U. Leushake, A.N. Winter, B.H. Rabin, B.A. Corff, in: W.A. Kaysser (Ed.), (1999) General Aspects of FGM Fabrication by Powder Stacking, Proceedings of the 5th International Symposium on FGM 1998, Trans Tech Publications, Switzerland, pp. 13–18.

[46]M. Takemura, T. Hyakubu, A. Yoshitake, M. Tamura, in: J.B.Holt, M. Koizumi, T. Hirai, Z.A. Munir (Eds.), (1993) Ceram. Trans. "Mechanical and thermal properties of FGM fabricated by thin lamination method Functionally Gradient Materials." American Ceramic Society, Westerville, OH, pp. 271–278.

[47]Zeng Y-P, Jiang D-L. Fabrication and Properties Of Tape-Cast Laminated and Functionally Gradient Alumina-Titanium Carbide Materials, J. Am. Ceram. Soc. 83(2000), pp. 2999–3003.

[48]Zhang J, Wang Y-Q, Zhou BL, Wu XQ. Functionally Graded Al/Mg_2Si In-situ Composites prepared by Centrifugal Casting, J. Mater. Sci. Lett. 17(1998), pp. 1677–1679.

[49]Lee NJ, Jang J, Park M and Choe CR. Characterization of functionally gradient epoxy/carbon fibre composite prepared under centrifugal force, J. Mater. Sci. 32(1997), pp. 2013–2020.

[50]Sleight A. W. "Thermal contraction", Endeavor. 19(1995), pp. 64-68.

[51]Evans J.S.O., Mary T. A., Sleight A. W. "Negative thermal expansion materials", Physica B., 241-243(1998), pp. 311-16.

[52]Sleight A. W., "Compounds that contract on heating", J inorg. Chem., 37(1998), pp. 2854-60.

[53]Mary T. A., Evans J. S. O, Vogt T, Sleight A. W., "Negative thermal expansion from 0.3 to 1050 Kelvin in ZrW_2O_8", Science. 272(1996), pp. 90-92.

[54]Evans J. S. O., Mary T. A, Vogt T., Subramanian M. A, Sleight A. W. "Negative thermal expansion in ZrW_2O_8 and HfW_2O_8", Chem Mater 8(1996), pp. 2809-23.

[55]Closmann C., Sleight A. W., Haygarth J. C., "Low-temperature synthesis of ZrW_2O_8 and Mo-Substituted ZrW_2O_8", J Solid State Chem 139(1998), pp. 424-26.

[56]Korthuis V., Khosrovani N., Sleight A. W., Robers N., Dupree R., Warren W. W. Jr., "Negative thermal expansion and phase transitions in the ZrV_2-$xPxO_7$ series", Chem Mater, 7(1995), pp. 412-17.

[57]Oguz, B., 2009 "Design and processing of perspirable skin through numerical analysis", M.S Thesis at Michigan State University.

[58]Sun L., 2009, "Multi-functional materials by powder processing for a thermal protection system with self-cooling capability: Perspirable skin", PhD. Dissertation at Michigan State University.

[59]Sheehan J. E., Buesking K. W., Sullivan B. J., "Carbon-Carbon Composites", Annu. Rev. Mater. Sci., 24(1994), pp. 19-44.

[60]Mary T. A, Evans J. S. O, Vogt T, Sleight A. W., 1996, Negative thermal expansion from 0.3 to 1050 Kelvin in ZrW_2O_8, Science, 272(5258), pp. 90-92.

[61]T.A. Mary, J.S.O. Evans, A.W. Sleight, and T. Vogt, Negative Thermal Expansion from 0.3 K to 1050 K in ZrW_2O_8, Science 272(1996), pp. 90-92.

[62]DryMiotis F. R., Ledbetter H., Betts J. B., Kimura T., Lashley J. C., Migliori A., Ramirez A. P., Kowach G. R., Van Duijn J., "Monocrystal elastic constants of the negative-thermal-expansion compound Zirconium Tungstate (ZrW_2O_8)", Phy.s Rev. Lett., 93(2004), pp. 1-4.

[63]Sun L, Shi X, Sneller A, Uher C and Kwon P. (2008) In-situ synthesis and thermal properties of ZrO_2/ ZrW_2O_8, The proceeding for 23rd annual technical conference of ASC, pp. 14-23.

[64]Al-Dawery IAH Butler EG, Fabrication of high-temperature resistant oxide ceramic matrix composites." Composites Part A 32(2001), pp.1007-1012.

[65]Kuribayashi K, Yoshimura M, Ohta T, and Sata T. High-temperature phase relations in the system Y_2O_3-$Y_2O_3 \cdot WO_3$, J Am. Ceram. Soc. 63(1980), pp. 644-647.

[66]Sun L and Kwon P. ZrW_2O_8–ZrO_2 Continuous Functionally Graded Materials Fabricated by In Situ Reaction of ZrO_2 and WO_3, Journal of the American Ceramic Society, 93(2010), pp. 703-708.

[67]Waring JL. Phase equilibria in the system aluminum oxide—tungsten oxide, J. Am. Ceram. Soc., 48(1965), pp. 493-493.

[68]Sun L, Sneller A and Kwon P. Processing Techniques for Functionally Graded Materials, Mater Sci Eng A. 488(2008), pp. 31–38.

[69]Westman A. E. R., and Hugill H. R., The packing of particles, J. Am. Ceram. Soc. 13 (1932), pp. 767–779.

[70]Hansen, J. D., Rusin, R. P., Teng, M.-H. and Johnson, D. L., Combined-stage sintering model. J. Am. Ceram. Soc., 75(1992), pp.1129–1135.

[71]Watanabe.R. Powder processing of functionally gradient materials. MRSBull. (1995), pp. 32-34.

[72]Sun L., Sneller A. and Kwon P., Powder selection in cosintering multi-layered ceramic functionally graded materials based on the densification kinetics curves, J Comp Mat. 43 (2009), pp. 469-483.

[73]White H. E., and Walton S. F., Particle packing and particle shape, J. Am. Ceram. Soc. 20 (1937), pp. 155-166.

[74]Nysrom, C, Alderborn, M, Duberg. Bonding surface area and bonding mechanism-two important factors for the understanding of powder compactability. Drug. Dev. Ind. Pharm., 19(1993), pp.2143-2197.

[75]Muralithran, G., Ramesh, S., The effects of sintering temperature on the properties of hydroxyapatite. Ceramics International, 26(2000), pp.221-230.

[76]Kim, D.H., Kim, C.H., Toughening behavior of silicon carbide with additions of Yttria and alumina. J.Am.Ceram. Soc., 73(1990), pp. 1431-1434.

[77]Granqvist, C.G., Buhrman, R.A., Wyns, J., Far-infrared absorption in ultrafine Al particles. Phys.Rev.Lett. 37(1976), pp. 625-629.

[78]Mayo, M. J. Processing of nanocrystalline ceramics from ultrafine particles. Int. Mat. Rev., 41(1996), pp. 85-115.

[79]Sun Li, Basak Oguz, Kwon, P., Powder mixing effect on the compaction capabilities of ceramic powders. Powder Technology. 195(2009), pp. 227-234.

[80]Kazuya Shimoda, Hinoki, T., Effect of additive content on transient liquid phase sintering in SiC nanopowder infiltrated SiCf/SiC composites. Composites Science and Technology. 71(2011), pp. 609-615.

[81]Phillipe Boch, Jean-Claude Niepce. Ceramic Materials: Processes, Properties and Applications. Hermes Science Publication, (2007), pp. 82-85.

[82]Chen, J. C., G. C. Huang, C. Hu, and J. P. Weng. "Synthesis of negative-thermal-expansion ZrW2O8 substrates," Scripta. Materialia. 49(2003), pp. 261-266.

[83]V. P. Filonenko and L. G. Khvostantsev. Compacting tungsten powders with varying particle size using hydrostatic pressure up to 5 GPa. Powder metallurgy and metal ceramics. 31(1992), pp. 296-299.

[84]R. Vassen and D. Stöver, Compaction mechanisms of ultrafine SiC powders. Powder Technol. 72(1992), pp. 223-226.

[85]Sun L., Sneller A. and Kwon P., Fabrication of Alumina/Zirconia functionally graded material: from optimization of processing parameters to phenomenological constitutive models, Mater. Sci. Eng. 488 (2008), pp. 31-38.

[86]McGeary R. K., Mechanical packing of spherical particles, J. Am. Ceram. Soc. 44(1961), pp. 513-522.

[87]Liu D. M. and Lin J. T, Influence of ceramic powders of different characteristics on particle packing structure and sintering behavior, J. Mater. Sci. 34 (1999), pp. 1959-1972.

[88]Lim KY, Kim YW, Kim KJ, Yu JH. Effect of in situ-synthesized nano-size SiC addition on density and electrical resistivity of liquid-phase sintered silicon carbide ceramics. J Ceram Soc Jpn, 119(2011), pp. 965-967.

[89]R. Vassen and D. Stöver. Processing and properties of nanograin silicon carbide. J Am Ceram Soc, 82(1999), pp. 2585-2593.

[90]C. De Meyer, L. Vandeperre, and S. Hoste. Processing effects on the microstructure observed during densification of the NTE-compound ZrW_2O_8. Crystal Engineering. 5(2002), pp. 469-478.

[91]J. L. WARING. Phase Equilibria in the System Aluminum Oxide-Tungsten Oxide. Journal of The American Ceramic Society. 48(1965), pp. 493.

[92]John R. GUNTER and Marcel AMBERG. “High-temperature" Magnesium tungstate, MgWO4, prepared at moderate temperature. Solid State Ionics. 32/33(1989), pp. 141-146.

[93]Guo, Q. and Kleppa, O. J., Enthalpies of formation from the component oxides of MgWO4, CaWO4, SrWO4 and BaWO4, determined by high temperature direct synthesis calorimetry. Thermochim. Acta, 288(1996), pp. 53–61.

[94]R.C. Pullar, S. Farrah, and N. McN. Alford. $MgWO_4$, $ZnWO_4$, $NiWO_4$ and $CoWO_4$ microwave dielectric ceramics. Journal of the European Ceramic Society. 27(2007), pp. 1059–1063.

[95]F.A. Danevich, D.M. Chernyak, and A.M. Dubovik, B.V. MgWO4-A new crystal scintillator. Nuclear Instruments and Methods in Physics Research Section A: Accelerators, Spectrometers, Detectors and Associated Equipment. 608(2009), pp. 107-115.

[96]Lukel. Y. Chang, Margaret G. Scroger, and Bert Phillips. Alkaline-Earth Tungstates: Equilibrium and Stability in the M-W-O Systems. Journal of the American Ceramic Society. 49(1966), pp. 385-389.

[97]Wei Liu and Baosheng Li. Elasticity of amorphous zirconium tungsate at high pressure. Appl. Phys. Lett. 93(2008), pp. 1901-1904.

[98]http://en.wikipedia.org/wiki/Bulk_modulus

[99]Schönfeld, F., C μ FD –Simulation of Microfluidic Systems. COMSOL CONFERENCE, Grenoble 2007, pp. 12.